The Dissertation Committee for Sayema Chowdhury certifies that this is the approved version of the following dissertation:

Synthesis, characterization, and electrical transport in 2-D transition metal dichalcogenides grown by chemical vapor deposition

Committee:

_____

Sanjay Banerjee, Supervisor

_____

Deji Akinwande

_____

Leonard F Register

_____

Ananth Dodabalapur

_____

Yaguo Wang

Synthesis, characterization, and electrical transport in 2-D transition metal dichalcogenides grown by chemical vapor deposition

by

Sayema Chowdhury

Dissertation

Presented to the Faculty of the Graduate School of
The University of Texas at Austin
in Partial Fulfillment
of the Requirements
for the Degree of

Doctor of Philosophy

The University of Texas at Austin
August 2022

Dedicated to my mother

Acknowledgments

My experience at UT Austin would not be nearly as remarkable as it was without the presence of such amazing group of peers, collaborators, and mentors. I will always be indebted to them.

I would like to start by expressing my deepest gratitude to Professor Banerjee for giving me the opportunity to be a part of his group which shaped me up into the person I am today. Thank you, Professor, for giving me a complete freedom to explore various research routes and finding the one that most interested me, and for guiding me through the entire journey by offering useful insights, engineering solutions and unlimited logistic support. Thank you for understanding the hardships I faced being a mother of two and for allowing me the flexibility I so very much needed.

I would also like to thank all the professors on my Ph.D. Dissertation Committee – Professor Deji Akinwande, Professor Leonard F. Register, Professor Ananth Dodabalapur and Professor Yaguo Wang. I am especially grateful to Dr. Filippo Mangolini for teaching me the basics of advanced surface analysis, and for guiding me through a lot of spectroscopic studies that supported my research.

I want to express my heartfelt gratitude to all my mentors, seniors and colleagues for showing me the ropes, for their companionship and for the many memories that I will cherish forever. A special shoutout to Amritesh Rai for selflessly mentoring me, for teaching me the basics of clean room fabrication techniques, for answering the innumerous naïve questions I had and for being such a good friend both in and outside the lab. I would also like to express my sincerest thanks to Anupam Roy for walking me through the research process, for instilling the necessity of attention to detail, for your unwavering support and your boundless patience. Thank you for criticizing me, for encouraging me, for listening to me and especially for knowing when to do which. Many thanks to Rudresh Ghosh and Chison Liu for setting up the CVD growth system that I have used extensively during this work. I also want to thank William Hsu, Stephen Szczepaniak, Hema CP

Movva, Omar Mohammad, Harry Chou, Saungeun Park, Maruthi Yogeesh and Michael Rodder for help with training, insightful discussions and valuable suggestions. I am also grateful to Deepyanti Taneja and Martha I. Serna for their help and friendship.

Thanks to my amazing FABLAB-TA mentors, Tanuj Trivedi and Andreas Hsieh for training me and for repeating every procedure for the umpteenth time until I felt comfortable to run things on my own. In addition to all the technical nitty-gritties, I learnt the virtue of patience and perseverance from you both. I also want to thank Praveen Pasupathy, Nitin Prasad and Xian Wu for support in running and maintaining the FABLAB smoothly. I want to take this opportunity to acknowledge all my peers in Banerjee group past and present, who have helped me directly or indirectly during my time at MRC: Tanmoy Pramanik, Rik Dey, Atresh Sanne, Jaehun Ahn, Sai Subhramanya Teja, Chris Luth, Jessica Depoy, Siyu Wu, Ryan Schalip, Matthew Disiena, Alexander Klatt, Joe Freidman, Ansh Gupta, Isaac Bodemann and Jatin Vikram Singh. Thank you for the wonderful time and for the many memories.

I am extremely grateful to the administrative and support staff at EER, MRC and TMI. Thank you, Melanie Gulick and Melody Singleton, for all your valuable suggestions and indispensable help during my admission and throughout my PhD journey. My sincerest gratitude to Jean Toll, for not only helping with mountain loads of paperwork, but also for being a place for me to vent and seek comfort when I needed a friend. I would like to acknowledge Jesse James for all the training and technical support, for always being available when I needed help and for going above and beyond and helping me with setting up the fabrication lab at EER. I am also grateful to Ricardo Garcia, Bill Ostler, Johnny, William Veith, Marylene Palard, Sarmita Majumder, Hugo Celio and Raluca Gearba for training and technical support. I would like to thank Christine Woods, Darren Robbins, Joyce Kokes, Gerlinde Sehne, David Korts for their continuous support and assistance throughout my days at UT.

I had a wonderful opportunity to intern at Micron during my grad studies at UT, which provided me with exposure to work in an industry setting. I am deeply indebted to

my manager Rita Klein and to Melanie Lewis for giving me the opportunity to intern at Micron. I want to thank my mentor Ross Economy for teaching me everything from scratch and for your valuable suggestions regarding both professional and personal life. The entire experience has certainly been very enlightening.

I want to take this opportunity to remember my late father (*Abbi*), late aunt (*Khalamoni*) and late uncle (*Mama*) and express how sorry I am that they are not here to see me graduate. I would like to express my deepest gratitude to my family for all the inspiration, encouragement, and the unconditional love they bestowed on me during all these years. I especially thank my super-mom for making me what I am today and for the courage and tenacity she showed in educating me. Thanks to my sister and her two little boys, Umar and Usman whose love, stories, giggles and conversations have lifted my mood uncountable number of times. To my boys, Arham and Idrees, you have made me stronger and filled my heart with so much love and joy. It is not despite you, but because of you that I thrived. Lastly, I want to thank my husband Hasib: none of this would have been possible without your inspiration and camaraderie. Thank you for your patience and support during the most challenging times in my life.

Abstract

Synthesis, characterization, and electrical transport in 2-D transition metal dichalcogenides grown by chemical vapor deposition

Sayema Chowdhury, Ph.D.

The University of Texas at Austin, 2022

Supervisor: Sanjay Banerjee

Transition metal dichalcogenides (TMDs), possessing a multitude of interesting properties, have emerged as an interesting choice for various types of electronic, optoelectronic and beyond CMOS device applications. Chemical vapor deposition (CVD) has been used extensively as an efficient, fast, reliable, and scalable route to grow uniform, high quality, large area TMDs. In this work, we report atmospheric pressure CVD (APCVD) and metal-organic CVD (MOCVD) growth of TMDs and study the effects of growth temperature, metal/chalcogen flux, reaction environment, *etc*. in modulating the shape, size, crystal structure, and uniformity of the grown film.

To control the morphology more efficiently, we established a process for transition from compact two-dimensional (2D) domain to branched domain morphologies by varying the growth temperature and transition metal flux. Two different types of branched domains, fractals and dendrites, are observed which follow different growth mechanisms. In addition to the experimental investigations, we used a phase field simulation method for a better understanding of the dependence of the domain morphologies on the growth parameters. To control the 2D/3D growth mode, crucial role of chalcogen flux is investigated. While multilayer islands form in a chalcogen-deficient condition, a chalcogen-rich condition promotes lateral growth by restricting transition metal-rich nuclei formation. Study of APCVD growth with different carrier gases show that a reducing environment under hydrogen gas is more favorable to achieve uniform 2D growth. Based on the experimental

observations, we propose an optimized CVD growth condition to achieve large-area high quality 2D TMD domains.

Beside the APCVD growth of TMDs, an alternative approach *via* MOCVD growth under low pressure followed by a high-temperature sulfurization process under atmospheric pressure has also been explored. This two-step process can substantially heal chalcogen vacancies, suppress carbon/oxygen contamination, and produce more homogeneously distributed triangular monolayer domains with the electrical performance comparable to APCVD-grown domains.

Table of Contents

List of Figures

Chapter 1: Introduction

1.1 MOTIVATION

Recent years have seen a strong surge in research of two-dimensional (2D) materials due to their versatile characteristics such as semiconducting and superconducting nature [3], sub-nanometer thickness [4], flexibility [5], high optical absorbance [6], high mobilities [7], spin orbit coupling [8], ferromagnetism [9] and so forth, making them an attractive choice for electronic [10–12], optoelectronic [13–16], spin [17] and valleytronic [18] devices. Transition metal dichalcogenides (TMDs) are a sub-class of 2D materials, where a transition metal is sandwiched between two chalcogen atoms forming a three-atom thick layer with strong intralayer covalent bonds and weak interplanar van der Waals (vdW) bonds [19], such that the 2D layers have no dangling bonds on the surface, leading to low density of surface and interface trap states and reduced scattering [20]. These make 2D TMDs a promising candidate for next generation electronics, and hence it is imperative to have a repeatable, reliable, scalable, and cost-effective synthesis method for uniform large scale monolayer TMDs. So far, the highest quality crystalline flakes are obtained by mechanical exfoliation [21], but it comes with its own limitations of small flake size, low yield and poor control over layer thickness. To scale up the production of TMDs for practical applications, various bottom-up synthesis methods, *e.g.*, molecular beam epitaxy (MBE) [22–24] and chemical vapor deposition (CVD) [25–31] are being

---

Much of the discussions presented in this Chapter have been adapted from the following references: Ref [1]: Chowdhury, S., Roy, A., Bodemann, I., Banerjee, SK., "*2D to 3D Growth of Transition Metal Diselenides by Chemical Vapor Deposition: An Interplay between Fractal and Compact Morphologies*" ACS Applied Materials & Interfaces **12**, 13, 15885–15892 (2020), reprinted with permission from [ACS Appl. Mater. Interfaces 2020, 12, 13, 15885–15892]. Copyright [2020] American Chemical Society. Available at: https://doi.org/10.1021/acsami.9b23286. Ref [2]: Chowdhury, S., Roy, A., Liu, C., Alam, MH., Ghosh, R., Chou, H., Akinwande, D., Banerjee, SK., "*Two-Step Growth of Uniform Monolayer MoS_2 Nanosheets by Metal–Organic Chemical Vapor Deposition*" ACS Omega **6**, 15, 10343–10351 (2021), reprinted with permission from [ACS Omega 2021, 6, 15, 10343–10351]. Copyright [2021] American Chemical Society. Available at: https://doi.org/10.1021/acsomega.1c00727, and a manuscript in preparation: Sayema Chowdhury et al. *"Role of hydrogen in suppressing secondary nucleation in chemical vapor deposited MoS_2*". The dissertator, S. Chowdhury, conceived and designed the experiments, conducted growths, carried out material characterization and analysis and largely wrote the manuscript with contributions from all the authors.

explored. Although MBE offers greater control over the film thickness and excellent repeatability of the growth yields, the small grain size in case of TMD growth limits its application in large scale electronic devices [24,32] Among different CVD methods, atmospheric pressure CVD (APCVD) has been extensively used to successfully grow large area TMDs such as MoS_2 [33], $MoSe_2$ [29], WS_2 [34], WSe_2 [26], ReS_2 [35], and $ReSe_2$ [36] with quality comparable to exfoliated flakes. This growth method greatly simplifies the process steps and considerably reduces total processing time, without compromising the quality of the grown films. Although the great variety of tunable growth parameters in APCVD such as growth temperature, metal/chalcogen flux, growth duration, reaction environment, *etc.*, provides a high degree of freedom to tailor the growth as required, in practice, single crystals of TMDs grown *via* APCVD method suffer from random nucleation, defects and vacancies and non-uniform thickness with multiple secondary islands. The effect of growth parameters such as substrate temperature, precursor flux, *etc.*, on the morphology and precise control over the thickness of the domains is yet to be explored in detail. Previous studies have reported suppressing the nucleation of secondary islands by ensuring effective reduction of the oxide-based precursor during CVD reaction [37]. Hence, to suppress multilayer growth, it is necessary to conduct a thorough study of the effects of hydrogen incorporation during CVD growth, in modulating the shape, size, uniformity, and purity of the grown film.

One of the major challenges of APCVD is the use of powder-based MoO_3 precursor which has a low vapor pressure, and hence must be placed in the central heating zone of the furnace which compromises precise control over the ratio of precursor flux leading to non-uniform thicknesses and inhomogeneity in domain sizes [38]. To combat these issues, use of metal-organic precursors having high vapor pressure are being investigated [39]. Metal-organic CVD (MOCVD) offers more efficient control over the metal flux and thus the ratio of metal-to-chalcogen flux that reaches the substrate can be tailored as required, thereby ensuring uniform thickness control. Several reports have demonstrated MOCVD growth of MoS_2 using precursors molyhexacarbonyl [$Mo(CO)_6$] for metal and diethyl sulfide [$(C_2H_5)_2S$] for chalcogen [40–42]. Diethyl sulfide inherently leaves considerable

carbon residues in the film that degrades material properties [43]. Other routes involve first creating an air and moisture stable precursor tetrakis (diethylaminodithiocarbomato) molybdate (IV) ($Mo(Et_2NCS_2)_4$) and then decomposing this single source to form MoS_2 *via* MOCVD [44]. Regardless of the precursors used, the growth often results in polycrystalline films with domain sizes of the order of a few nanometers [42,45,46]. Recently, MOCVD growths of MoS_2 with domain sizes larger than 10 μm have been reported. However, they involve long processing times (~ 26 hour per monolayer) [40] or require the substrates to be pre-exposed to halides [42,47], which form sodium/potassium metal oxide layer below the TMD monolayer as byproduct [48]. So far, an optimized MOCVD method that yields large area single crystal monolayer domains with uniform coverage across the entire substrate and free of contamination *e.g.*, carbon and/or alkali metal oxides, is yet to be developed.

1.2 OUTLINE

This dissertation is organized as follows.

Chapter-2 discusses detailed growth methods for the APCVD and MOCVD techniques. This chapter summarizes basic characterization results using optical microscopy, Raman and Photoelectron spectroscopy. Details of various as-grown film transfer techniques are also described here.

Chapter-3 reports APCVD growth of $MoSe_2$ and WSe_2 and discusses the effect of parameters such as temperature, growth time, chalcogen/metal flux on the morphology, and thickness of the grown material. An optimized recipe to grow compact domains and to promote lateral growth by suppressing the formation of multilayer islands is proposed.

Chapter-4 demonstrates APCVD growth of MoS_2 under different carrier gases are compared. APCVD Growths conducted under an inert atmosphere (Argon and Nitrogen) and reducing atmosphere (Hydrogen) are compared. Furthermore, to understand the effect

of H_2 incorporation during CVD growth, experimental findings are modeled using the phase field method.

Chapter-5 reports MOCVD growth of MoS_2 film followed by sulfurization at high temperature to achieve a homogeneous distribution of single crystal triangular domains of monolayer thickness. Electrical properties and material properties are compared before and after sulfurization.

Chapter-6 summarizes the key findings discussed in this dissertation and identifies potential future research pathways.

Appendix-A shows the major components of the growth system and provides the recipe for MoS_2 synthesis.

Appendix-B demonstrates the microfabrication process used in this work.

Appendix-C compares TMD growth on various substrates.

Appendix-D describes large area CVD growth of TMDs using phase field simulation.

Chapter 2: TMD Growth and Characterization

2.1 INTRODUCTION

Various TMDs are synthesized using chemical vapor deposition. Here we discuss the growth method and some primary characterization techniques to confirm the quality of the grown TMDs.

2.2 MATERIAL SYNTHESIS

2.2.1 Atmospheric Pressure Chemical Vapor Deposition

2.2.1.1 MoS_2:

A clean double-side polished Si/SiO_2 (300 nm, thermally grown oxide) substrate was placed on an alumina combustion boat/crucible containing 8.5 mg of MoO_3 (99.5% pure Alfa Aesar, CAS 1313-27-5) and placed inside a 1 in. quartz tube and positioned at the center of a single-zone Lindberg/Blue M furnace as seen in the schematic in Fig. 2.1. A second boat containing S (99.98% Sigma-Aldrich CAS: 7704-34-9) was placed upstream in the tube outside the central heating zone of the furnace, and a separate coil heater was

---

Portions of this chapter, including results and figures have been adapted from the following references: Ref [1]: Chowdhury, S., Roy, A., Bodemann, I., Banerjee, SK., "*2D to 3D Growth of Transition Metal Diselenides by Chemical Vapor Deposition: An Interplay between Fractal and Compact Morphologies*" ACS Applied Materials & Interfaces **12**, 13, 15885–15892 (2020), reprinted with permission from [ACS Appl. Mater. Interfaces 2020, 12, 13, 15885–15892]. Copyright [2020] American Chemical Society. Available at: https://doi.org/10.1021/acsami.9b23286. Ref [2]: Chowdhury, S., Roy, A., Liu, C., Alam, MH., Ghosh, R., Chou, H., Akinwande, D., Banerjee, SK., "*Two-Step Growth of Uniform Monolayer MoS_2 Nanosheets by Metal–Organic Chemical Vapor Deposition*" ACS Omega **6**, 15, 10343–10351 (2021), reprinted with permission from [ACS Omega 2021, 6, 15, 10343–10351]. Copyright [2021] American Chemical Society. Available at: https://doi.org/10.1021/acsomega.1c00727, and a manuscript in preparation: Sayema Chowdhury et al. *"Role of hydrogen in suppressing secondary nucleation in chemical vapor deposited MoS_2*". The dissertator, S. Chowdhury, conceived and designed the experiments, conducted growths, carried out material characterization and analysis and largely wrote the manuscript with contributions from all the authors.

attached to apply heat to the S boat. The system was pumped down to base pressure (~1.5 mTorr) and purged three times using ultrahigh pure N_2 at 200 sccm. The growth was conducted at 850 °C (with S kept at 150 °C) for 5 min under ambient pressure with a carrier gas (N_2) flow rate at 10 sccm. The furnace was then turned off, and the lid was opened to let the furnace cool down under ambient conditions.

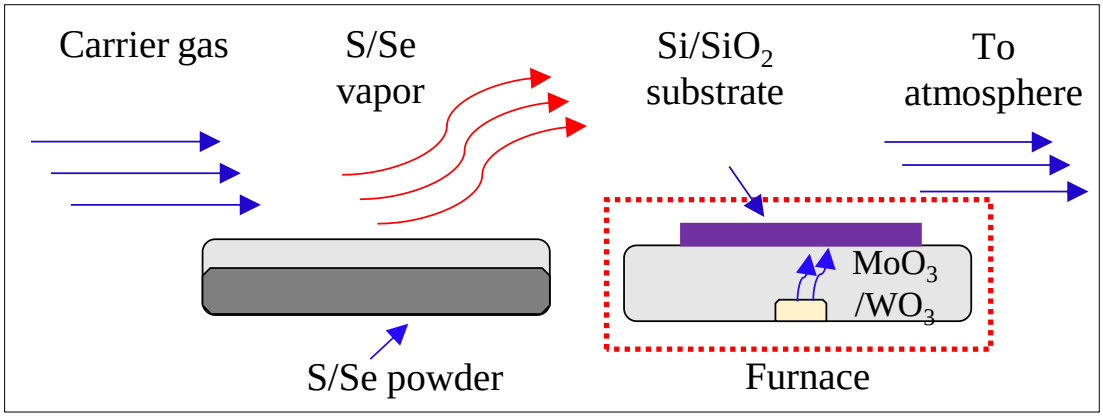

Figure 2.1: Schematic of the set up used for APCVD growth of 2D TMDs.

Figure 2.2 (a-b) shows an SEM image and optical micrograph of MoS_2 grown on the Si/SiO_2 substrate. Domain sizes range from few tens to hundreds of microns. Figure 2.2 (c,d) shows Raman and PL spectroscopies of a typical monolayer domain grown by APCVD. The Raman peak difference of ~19 cm^{-1} and a sharp distinct PL peak at 1.86 eV [full width at half-maximum (FWHM) is ~0.06 eV] are consistent with those of monolayer MoS_2 [49].

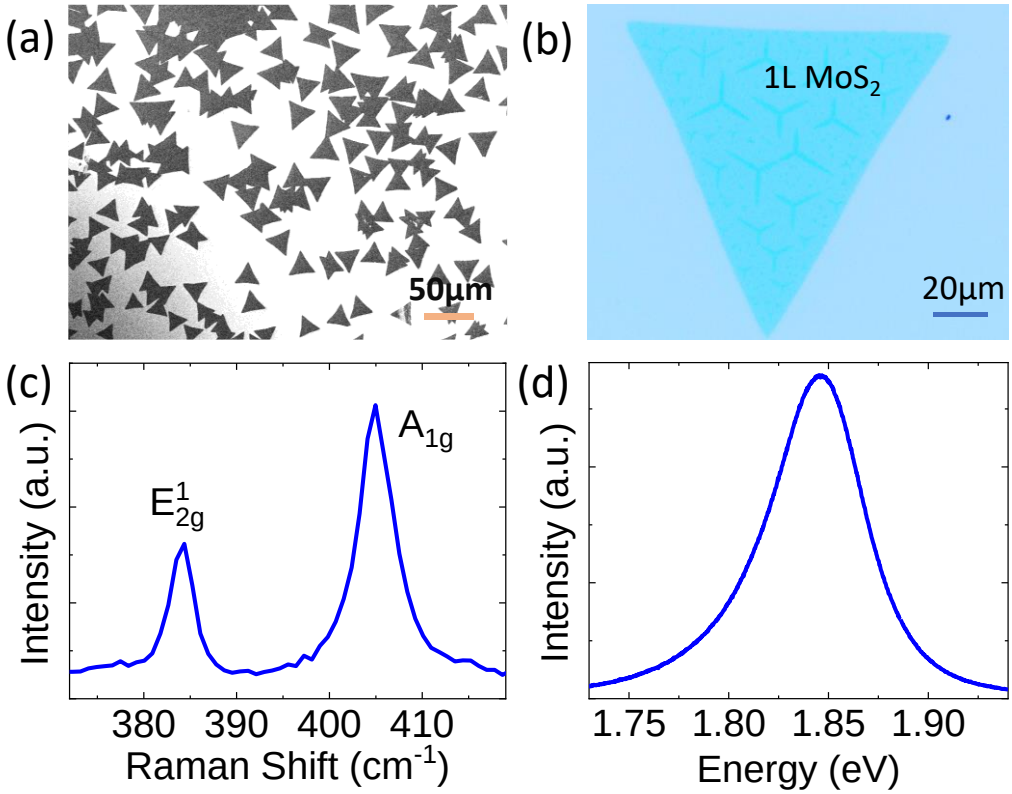

Figure 2.2: Monolayer MoS_2 domains grown on Si/SiO_2: (a) SEM image of MoS_2 domains (b) Optical microscopy image of a single MoS_2 domain. (c) Raman and (d) PL spectroscopy from monolayer MoS_2 domain.

2.2.1.2 $MoSe_2$

$MoSe_2$ is synthesized using the same experimental setup shown in Fig. 2.1 with Se precursor (99.999% Sigma Aldrich CAS: 7782-49-2) used instead of S. The growth was conducted at 900 °C with 5/65sccm of H_2/Ar as carrier gas. The Se heater temperature was

set at 300 °C. Figure 2.3 (a-c) shows the optical image, Raman, and PL spectroscopies of $MoSe_2$ grown by APCVD, respectively. The characteristic out-of-plane A_{1g} peak at 241 cm^{-1} and sharp PL peak at 1.55 eV corresponds to monolayer $MoSe_2$ [1].

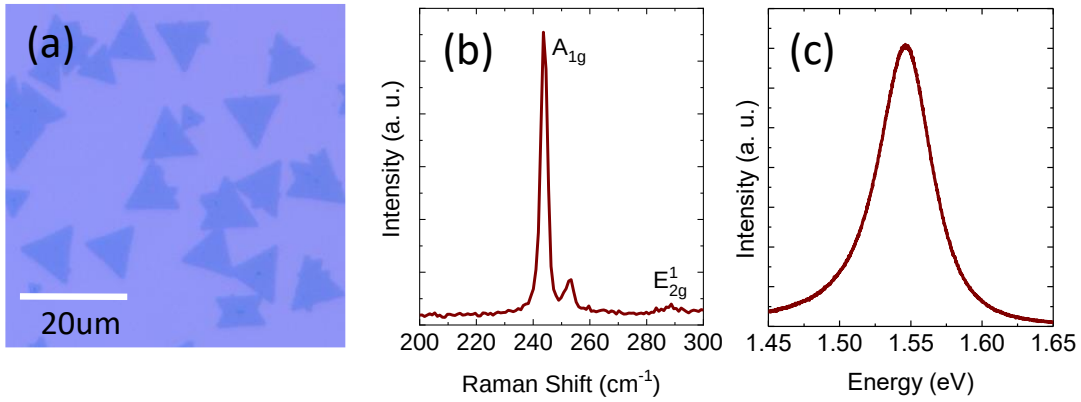

Figure 2.3: Monolayer $MoSe_2$ domains grown on Si/SiO_2: (a) Optical microscopy image, (b) Raman and (c) PL spectroscopy of monolayer $MoSe_2$ domain.

2.2.1.3 WS_2

WS_2 is grown using solid oxide-based precursors WO_3 (99.995% pure Sigma Aldrich, CAS: 1314-35-8) and S (Sigma Aldrich, CAS number 7704-34-9, 99.98%) at 1000 °C for 5 min under atmospheric pressure [see section 2.2.1.1 for details in growth procedure]. The characteristic E^1_{2g} and A_{1g} peaks are observed at 352 cm^{-1} and 420 cm^{-1}. The strong PL peak at 1.97 eV corresponds to monolayer WS_2 as seen in Figure 2.4 [50]

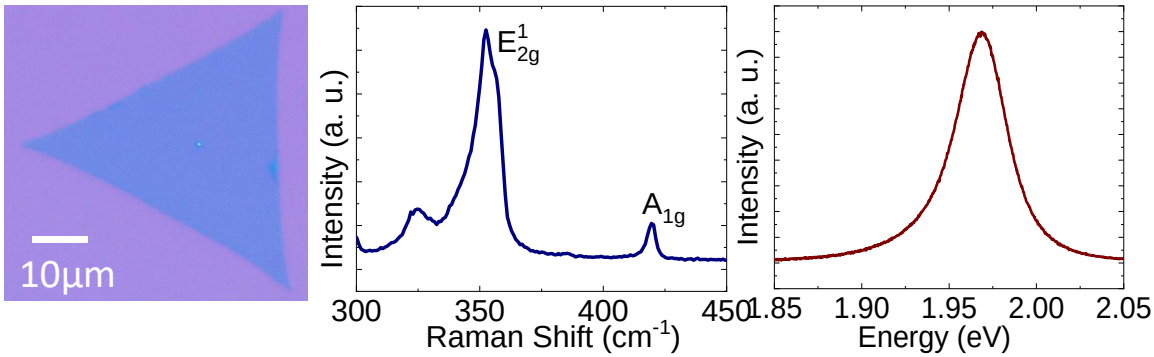

Figure 2.4: Monolayer WS_2 domains grown on Si/SiO_2: (a) Optical microscopy image of a single WS_2 domain, (b) Raman and (c) PL spectroscopy of monolayer WS_2.

2.2.1.4 WSe_2

The precursors used to grow WSe_2 are WO_3 (99.995% pure Sigma Aldrich, CAS: 1314-35-8) and Se (Sigma Aldrich, CAS number 7782-49-2, 99.98%) powder. WSe_2 grows at 1000 °C for 10 min with H_2 as carrier gas. Monolayer single crystal growth is seen from the optical image of Fig. 2.5 (a). Raman and PL spectra [Fig 2.5 (b,c), respectively] match closely with those for monolayer WSe_2 as reported in literature [26].

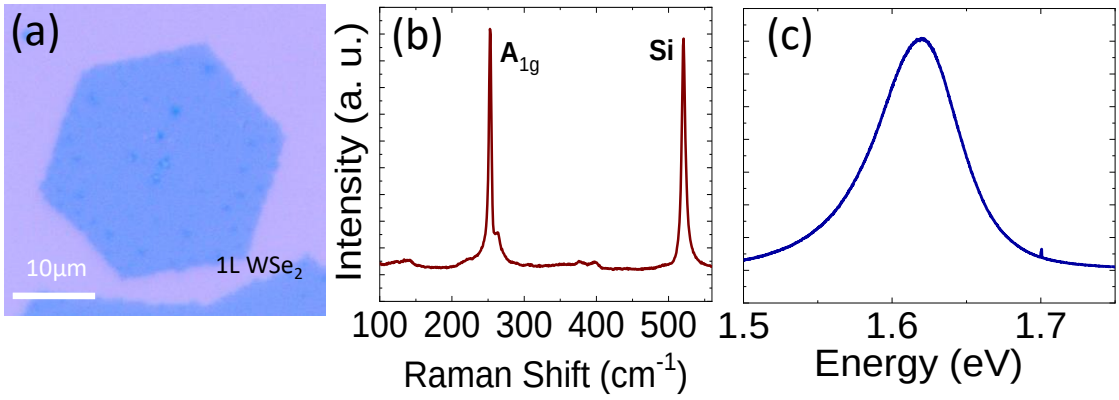

Figure 2.5: Monolayer WSe_2 domains grown on Si/SiO_2 (a) Optical microscopy image of a single WSe_2 domain, (b) Raman and (c) PL spectroscopy of monolayer WSe_2.

2.2.2 Metal Organic Chemical Vapor Deposition:

Solid precursors such as MoO_3 precursor used in APCVD has a low vapor pressure, it must be placed in the central heating zone which compromises precise control over the ratio of precursor flux leading to non-uniform thicknesses and inhomogeneity in domain sizes [38]. To combat these issues, use of metal organic precursors having high vapor pressure are being investigated [39]. MOCVD offers more efficient control over the metal flux and thus the ratio of metal to chalcogen flux that reaches the substrate can be tailored as required, thereby ensuring uniform thickness-controlled growth. This section describes growth method of various TMDs using MOCVD growth method.

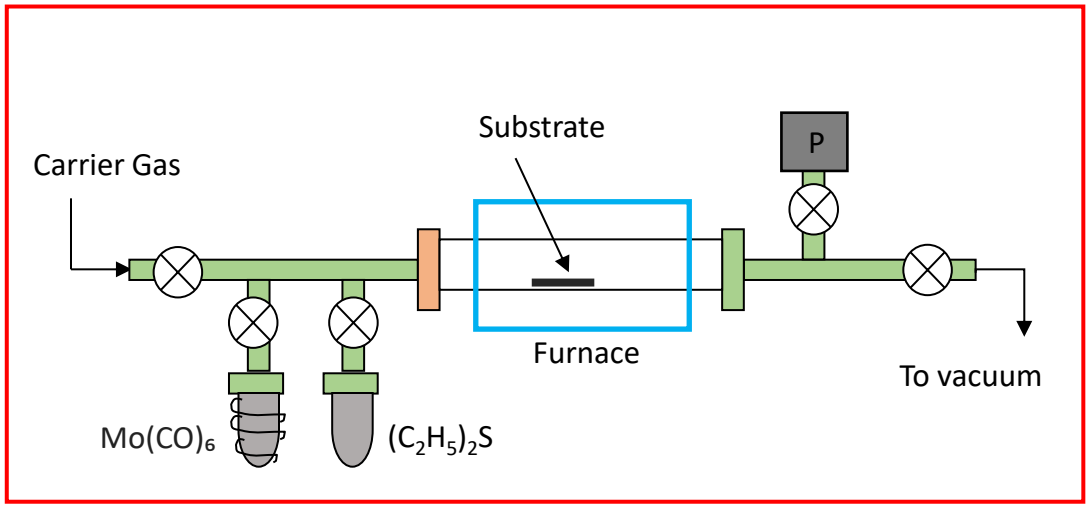

Figure 2.6: Schematic for the MOCVD growth system.

2.2.2.1 MoS_2

The schematic of the growth system is shown in Fig. 2.6. The system consists of a quartz tube with an inner diameter of 22 mm (outer diameter = 25 mm) inside a single zone Lindberg/Blue M furnace. The precursors used for MoS_2 growth are molybdenum hexacarbonyl, $Mo(CO)_6$ (Sigma-Aldrich, CAS number 13939-06-05, 99.9%), and diethyl sulfide, $(C_2H_5)_2S$ (Sigma-Aldrich, CAS number 352-93-2, 98%). The target substrate used in this work was 285 nm SiO_2 grown on highly doped double-side-polished p-type Si. At the start of the growth process, the target substrate (measuring 10 cm × 1.7 cm) was placed approximately 10 cm into the furnace and the system was pumped down to base pressure (~1.5 mTorr) following which three subsequent purge cycles using ultrahigh purity Ar at 100 sccm were performed. Afterward, Ar flow was cut off and H_2 flow was introduced at 5 sccm as the carrier gas for the rest of the growth. Background pressure of the system was held at 5 mTorr. $Mo(CO)_6$ and $(C_2H_5)_2S$ precursors were kept in bubblers in atmospheric pressure at 45 °C and at room temperature, respectively, and the flow rates were controlled via needle valves. The growth was conducted at 850 °C for a duration of 1 min after which

the precursor gas flow was cut off and the furnace was allowed to cool down, with only the carrier gas flowing.

Figure 2.7 (a,e) shows the Raman and PL spectroscopies of MoS_2 grown by MOCVD. Raman spectroscopic measurements show two distinct peaks at ~386 cm^{-1} and ~406 cm^{-1} which coincides with the Mo-S phonon modes E^1_{2g} (in-plane) and A_{1g} (out-of-plane) peaks of MoS_2, respectively, as found in literature [51] and a distinct PL peak at 1.87 eV corresponds to monolayer MoS_2.

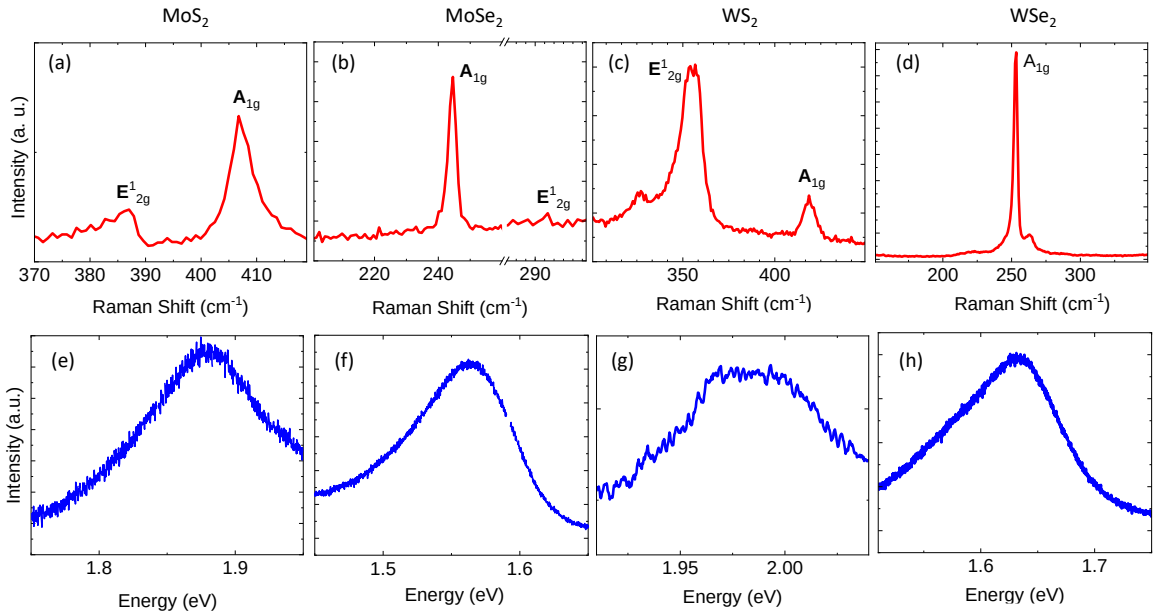

Figure 2.7: MOCVD Grown TMDs. Raman Spectra of (a) MoS_2 (b) $MoSe_2$ (c) WS_2 (d) WSe_2. (e-h) PL Spectra corresponding to different TMDs in (a-d).

2.2.2.2 $MoSe_2$

The MOCVD growth of $MoSe_2$ is similar to that of MoS_2 [section 2.2.2.1] was conducted using precursors $Mo(CO)_6$ (Sigma Aldrich, CAS number 13939-06-05, 99.9%) and Se powder (99.999% Sigma Aldrich CAS: 7782-49-2). A separate coil heater set at 300 °C was used to heat the crucible containing Se and was turned on when the furnace temperature reached 550 ºC. The growth was conducted under low pressure at 900 °C with

5 sccm of H_2 flowing as carrier gas. After a growth duration of 1 min, the metal organic precursor gas flow was cut off and the furnace was allowed to cool down, with only the carrier gas flowing. When the furnace temperature reached 550 °C the Se heater was disconnected. The characteristic out-of-plane A_{1g} peak at 244.8 cm^{-1} for $MoSe_2$ and sharp PL peak at 1.56 eV is observed in Fig. 2.7 (b,f).

2.2.2.3 WS_2

Using the setup shown in Fig. 2.6 and the precursors $W(CO)_6$ (99.99% pure, Sigma Aldrich CAS no: 14040-11-0) and diethyl sulfide, $(C_2H_5)_2S$ (Sigma-Aldrich, CAS number 352-93-2, 98%) WS_2 is synthesized by the method described in section 2.2.2.1. Fig 2.7 (c,g) shows the Raman and PL spectroscopies of WS_2 grown by MOCVD, respectively. The characteristic E^1_{2g} peak and A_{1g} peak at 356 cm^{-1} and 418 cm^{-1} and distinct PL Peak at 1.96 eV corresponding to WS_2 are observed. [50].

2.2.2.4 WSe_2

In a method similar to the one described in section 2.2.2.1, MOCVD WSe_2 was synthesized using precursors $W(CO)_6$ (99.99% pure, Sigma Aldrich CAS no: 14040-11-0) and Se powder (99.999% Sigma Aldrich CAS: 7782-49-2). The growth was conducted at 900 ºC for 1 min. A separate coil heater was used to heat the crucible containing Se at 300 °C. Figure 2.7 (d,h) shows the Raman and PL spectroscopies of WSe_2 grown by MOCVD. The characteristic out-of-plane A_{1g} peak at 252 cm^{-1} for monolayer WSe_2 and sharp PL peak at 1.6 eV corresponds to monolayer WSe_2.

2.3 CHARACTERIZATION TOOLS

2.3.1 Material Characterization

Several post growth characterization techniques were used to study the nature of the grown

materials. SEM (ZEISS Neon 40), optical microscope (Olympus) and AFM (Veeco) in tapping mode were used to study the morphology and to determine the step height on the as grown sample. Raman and PL spectroscopies were performed on all the samples before and after sulfurization using a Renishaw inVia Raman spectrophotometer system, coupled with 532 nm green laser. Raman and PL spectra were collected using a grating with 3000 lines/mm and 1200 lines/mm respectively. XPS were recorded using a commercial X-ray photoelectron spectrometer (Kratos Axis Ultra and Omicron, Germany), utilizing a monochromatic Al-K_α X-ray source ($h\upsilon$ = 1486.5 eV), electrostatic lens optics, and a multi-channel plate and delay line detector coupled to a hemispherical analyzer. The photoelectrons take-off angle was normal to the surface of the sample and 45° with respect to the X-ray beam. High resolution spectra were collected with pass energy of 20 eV. The pressure in the XPS chamber was typically 2×10^{-9} Torr during data acquisition. Details of the XPS system has been described elsewhere [52].

2.3.2 Device Fabrication and Measurement

Uniform monolayer MoS_2 domains on Si/SiO_2 substrates were identified using a combination of optical contrast, Raman spectroscopy, SEM and AFM. Device active regions and source/drain metal electrodes were defined with electron beam lithography. A stack of Ni/Au (20 nm/30 nm) was deposited as source/drain metal electrodes using *e*-beam evaporator. All electrical DC measurements were performed on a Cascade Microtech Summit 11000B-AP probe station using an Agilent 4156C parameter analyzer in ambient at room temperature under dark.

2.4 TRANSFER OF THE GROWN FILM:

For high quality crystalline growth, the growth temperature is usually in the range of >700 °C. This limits our choice of substrates to only those that can withstand such high temperature cycles. For a wide variety of practical applications, *e.g.*, in flexible electronics and optoelectronics, the grown TMD often requires to be transferred onto another substrate of choice. The two most common methods to transfer TMD flakes are described below:

2.4.1 PMMA Based Wet Transfer:

In this method, the polymethyl-methacralate solution is spin coated on $MoS_2/Si/SiO_2$ four times at the 4000 rpm, 2000 rpm, 1000 rpm and 1000 rpm, respectively. Each spin coating is for 45 s followed by 1 min drying in a hot plate at 165 °C.

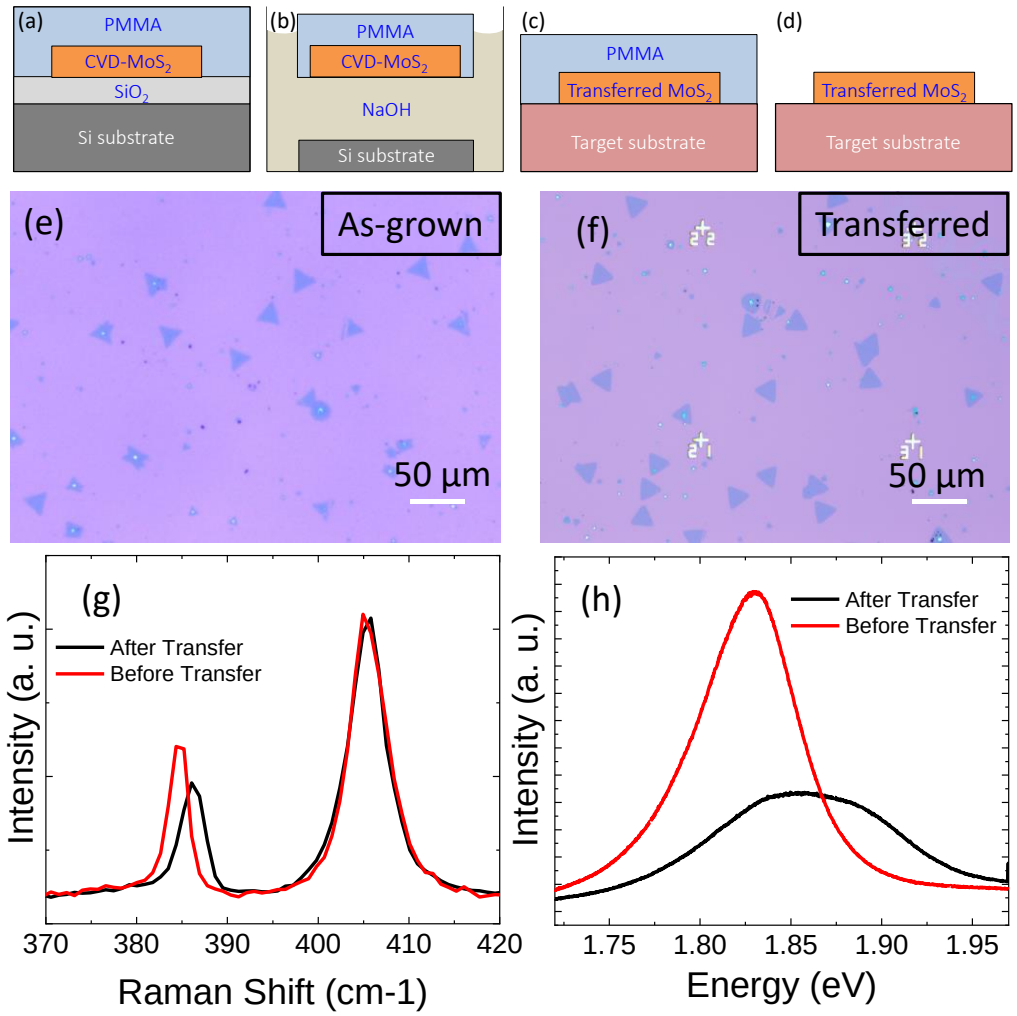

Figure 2.8: (a-d) Schematic diagram of the steps involved in wet transfer. (e-f) Optical images, (g) Raman and (h) PL spectroscopies of MoS_2 before and after transfer.

The $PMMA/MoS_2/Si/SiO_2$ sample is then immersed in 6N NaOH placed inside a water bath at 60 °C for an hour (or buffered oxide etchant at room temperature overnight) to etch

away the underlying silicon oxide. The schematic diagram illustrating the steps involved is shown in Fig. 2.8 (a-d). After all the oxide is etched away the PMMA/MoS_2 film remains suspended on the solution while the Si substrate separates. The film is then rinsed by distilled water several times to cleanse any etchant residue. A clean target substrate is then used to scoop the film and kept overnight to dry in air. Following this the sample was heated at 165 °C for 10mins and the PMMA was removed by acetone. The sample was then vacuum annealed (~ 10^{-7} Torr) at 340 °C for 8 hours to remove any PMMA residue. Figure 2.8 (e,f) shows optical microscopy images of an MoS_2 sample grown on Si/SiO_2 and transferred using NaOH wet transfer method onto another Si/SiO_2 substrate with alignment marks, respectively. Figure 2.8 (g) shows comparison of Raman spectra before and after the transfer. The in-plane E^1_{2g} mode is sensitive to the strain that develops in MoS_2 during growth [53] and the blue shift upon transfer signifies relaxation of that strain. This can also be seen in the PL spectra as seen in Fig. 2.8 (h) where the transfer results in blue shift of the PL peak.

2.4.2 PDMS Based Wet Transfer:

In polydimethylsiloxane (PDMS) stamp transfer monolayer MoS_2 is brought into conformal contact with PDMS and the PDMS/MoS_2/Si/SiO_2 stack is immersed in diluted water. Since the original substrate (SiO_2) is hydrophilic, water intercalates into the TMD/substrate interface, and separates them. The PDMS-TMD film is then brought into contact with the target substrate following which the PDMS stamp was peeled off to leave monolayer TMD films on the target substrate. This method however exerts significant mechanical strain on the TMD film which often results in tearing of the film. Figure 2.9 compares MoS_2 domains transferred *via* PMMA based method [Fig. 2.9 (a)] and PDMS based method [Fig. 2.9 (b)]

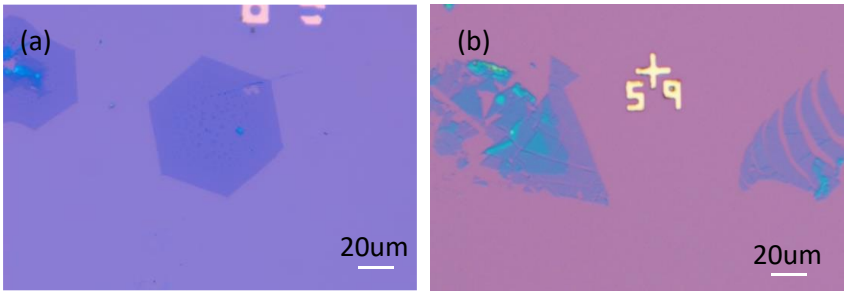

Figure 2.9: Optical Images following transfer of MoS_2 using (a) PMMA based wet transfer (b) PDMS and water-based transfer methods.

Chapter 3: Two-Dimensional to Three-Dimensional Growth of Transition Metal Diselenides by Chemical Vapor Deposition: Interplay between Fractal, Dendritic, and Compact Morphologies

3.1 INTRODUCTION

In this work, we demonstrate APCVD growth of $MoSe_2$ and WSe_2 and investigate the effect of parameters such as temperature, growth time, chalcogen/metal flux on the morphology, and thickness of the grown material. The crystalline quality, thickness, uniformity, and stoichiometry of the domains are investigated using several characterization techniques, for example, Raman and photoluminescence (PL) spectroscopies, scanning electron microscopy (SEM), atomic force microscopy (AFM), X-ray photoelectron spectroscopy (XPS), and so forth. We propose an optimized window for tuning the growth parameters to ensure compact domains and to promote lateral growth by suppressing the formation of multilayer islands.

3.2 EXPERIMENTAL METHODS

3.2.1 Growth:

Monolayer $MoSe_2$ was synthesized using APCVD. A clean double side polished Si/SiO_2 (300 nm, thermally grown oxide) substrate was placed on an alumina combustion boat/crucible containing roughly 8.5 mg of MoO_3 (99.5% pure Alfa Aesar, CAS 1313-27-5) and placed inside a 1″ quartz tube and positioned at the center of a single zone Lindberg/Blue M furnace. A second boat containing excess Se (99.999% Sigma-Aldrich CAS: 7782-49-2) was placed upstream in the tube outside the central heating zone of the

Much of the discussions, results and figures presented in this Chapter have been adapted from the following reference: Ref [1]: Chowdhury, S., Roy, A., Bodemann, I., Banerjee, SK., "*2D to 3D Growth of Transition Metal Diselenides by Chemical Vapor Deposition: An Interplay between Fractal and Compact Morphologies*" ACS Applied Materials & Interfaces **12**, 13, 15885–15892 (2020), reprinted with permission from [ACS Appl. Mater. Interfaces 2020, 12, 13, 15885–15892]. Copyright [2020] American Chemical Society. Available at: https://doi.org/10.1021/acsami.9b23286. The dissertator, S. Chowdhury, conceived and designed the experiments, conducted growths, carried out material characterization and analysis and largely wrote the manuscript with contributions from all the authors.

furnace and a separate coil heater was used to apply heat to the Se boat. For WSe_2 growth, 11.0 mg of WO_3 (99.995% pure Sigma Aldrich, CAS: 1314-35-8) was used. The system was pumped down to base pressure (~1.5 mTorr) following which three subsequent purge cycles using ultrahigh purity argon at 100 sccm were performed. The growth was conducted under ambient pressure with a carrier gas flow rate of H_2/Ar at 5/65 sccm. Owing to the low reactivity of Se, the presence of H_2 in the carrier gas during the entire growth process of selenides is crucial where H_2 acts as a reductive species to promote the growth. The growth was conducted under two different Se environments – Se-rich and Se-deficient – controlled by timing the onset of the heater associated with the Se boat. The onset temperature is defined as the furnace temperature when Se is turned on. The onset temperatures are 550 °C and 750 °C for Se-rich and Se-deficient conditions, respectively. For the optimized growth (that yields 2D compact domains), the growth was conducted under Se-rich conditions, and the growth temperature was set to be 900 °C for $MoSe_2$ (1000 °C for WSe_2). Several samples were grown for different durations at different growth temperatures. The furnace was then turned off and the lid was opened to let the furnace cool down under ambient conditions. Higher metal flux conditions were achieved by increasing the amount of MoO_3. The temperature profiles for a growth under Se-rich and Se-deficient conditions are shown in Figure 3.1.

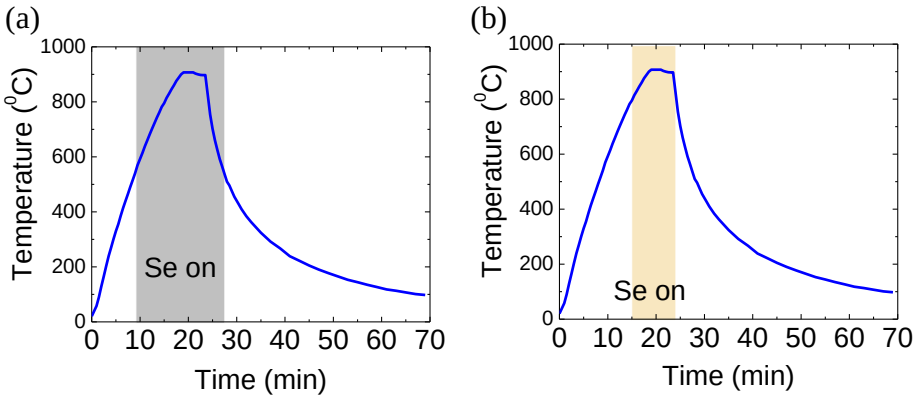

Figure 3.1: Temperature profiles during $MoSe_2$ growth on Si/SiO_2 substrates for two different conditions – (a) Se-rich and (b) Se-deficient.

3.3 INTERPLAY BETWEEN FRACTAL, DENDRITIC, AND COMPACT MORPHOLOGIES

3.3.1 Growth and Characterization of $MoSe_2$ and WSe_2

The schematic diagram of the experimental setup used for the APCVD growth is shown in Fig. 2.1. More details of the growth process are described in the Experimental Methods section 3.2.1. Optimum growth conditions (900 °C for $MoSe_2$ for 10 min) yield good coverage across a large area with primarily triangular or hexagonal domains [as shown in the optical microscopy images in Fig. 3.2 (a)].

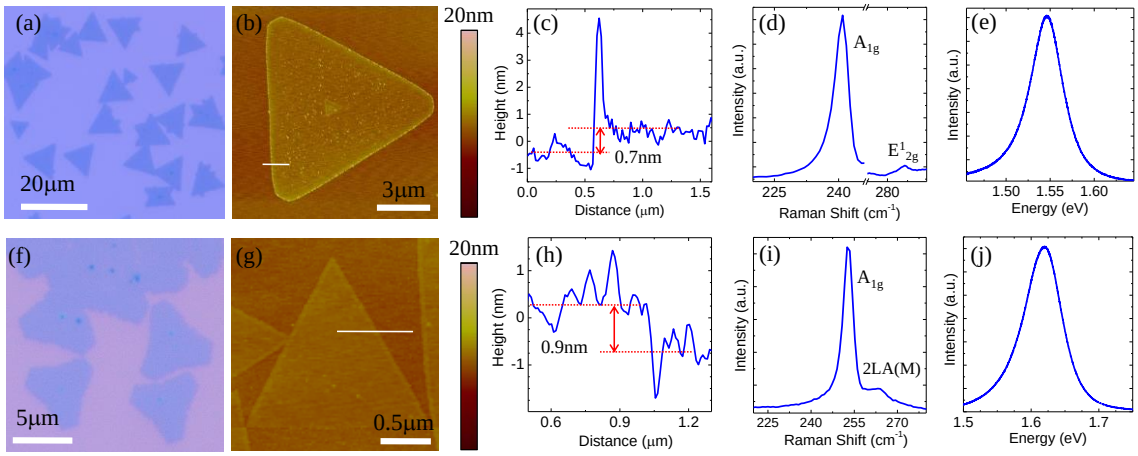

Figure 3.2: Monolayer $MoSe_2$ domains grown on Si/SiO_2: (a) Optical microscopy images (b) AFM image, (c) height profile across the line marked on AFM image, (d) Raman and (e) PL spectroscopy. Monolayer WSe_2 domains grown on Si/SiO_2: (f) Optical microscopy images (g) AFM image, (h) height profile across the line marked on AFM image, (i) Raman and (j) PL spectroscopy.

Figure 3.2 (b,c) shows the AFM image and a height profile of an $MoSe_2$ domain, which shows a step height of ~0.7 nm, corresponding to monolayer $MoSe_2$ [25]. Raman and PL spectroscopies are efficient and nondestructive techniques to characterize the grown domains to extract information such as the layer number and strain in the grown films. Raman spectrum for $MoSe_2$ excited by a 532 nm laser, as shown in Fig. 3.2 (d), depicts a characteristic out-of-plane A_{1g} peak at 241 cm^{-1} for monolayer $MoSe_2$. The

monolayer growth of TMDs was further confirmed by PL studies where a sharp distinct peak at 1.55 eV corresponds to the characteristic direct band gap of monolayer $MoSe_2$ [Figure 3.2 (e)]. For monolayer WSe_2, optical image, AFM and height profile with ~0.9 nm height [26] are shown in Fig. 3.2 (f-h), respectively. The corresponding Raman (A_{1g} peak at ~250 cm^{-1}) and PL spectra (1.64 eV) from WSe_2 are shown in Fig. 3.2 (i, j) respectively. The positions and relative intensities of Raman and PL peaks match very well with those of the corresponding $MoSe_2$ and WSe_2 exfoliated flakes, as well as previous literature reports [54–56].

3.3.2 Growth Engineering: Effect of Temperature and Metal Flux

Figure 3.3 shows the dependence of crystal morphology on growth temperature and flux of the metal precursor.

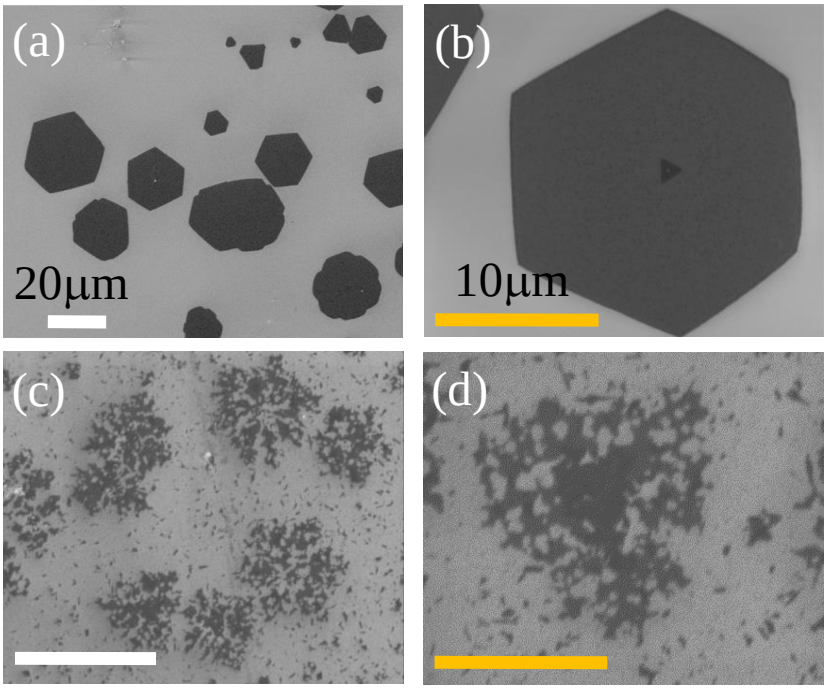

Figure 3.3: Effect of temperature on compact to fractal growth transition of 2D $MoSe_2$. SEM images showing (a) & (b) Compact domains grown at 900 ˚C. (c) & (d) Fractal domains for growth at lower substrate temperature (750 ˚C).

At 900 °C, the growth mostly yields single-crystal triangular/hexagonal monolayer $MoSe_2$, as shown in Fig. 3.3 (a,b). As the growth temperature is reduced to 750 °C, the compact structure of $MoSe_2$ domains ramifies into fractals, as seen from the SEM image in Fig. 3.3 (c). The fractal structure is clearly revealed in the zoomed-in image [Figure 3.3 (d)]. The growth at an intermediate temperature of 800 °C shows a near perfect hexagon with ragged edges, further emphasizing that the transition from compact to fractal is strongly dependent on the growth temperature [Figure 3.4]. Corresponding full width at the half maximum (FWHM), as calculated from Raman spectra and plotted in Fig. 3.4 (d), confirm a gradual improvement in the material crystallinity as the growth temperature increases.

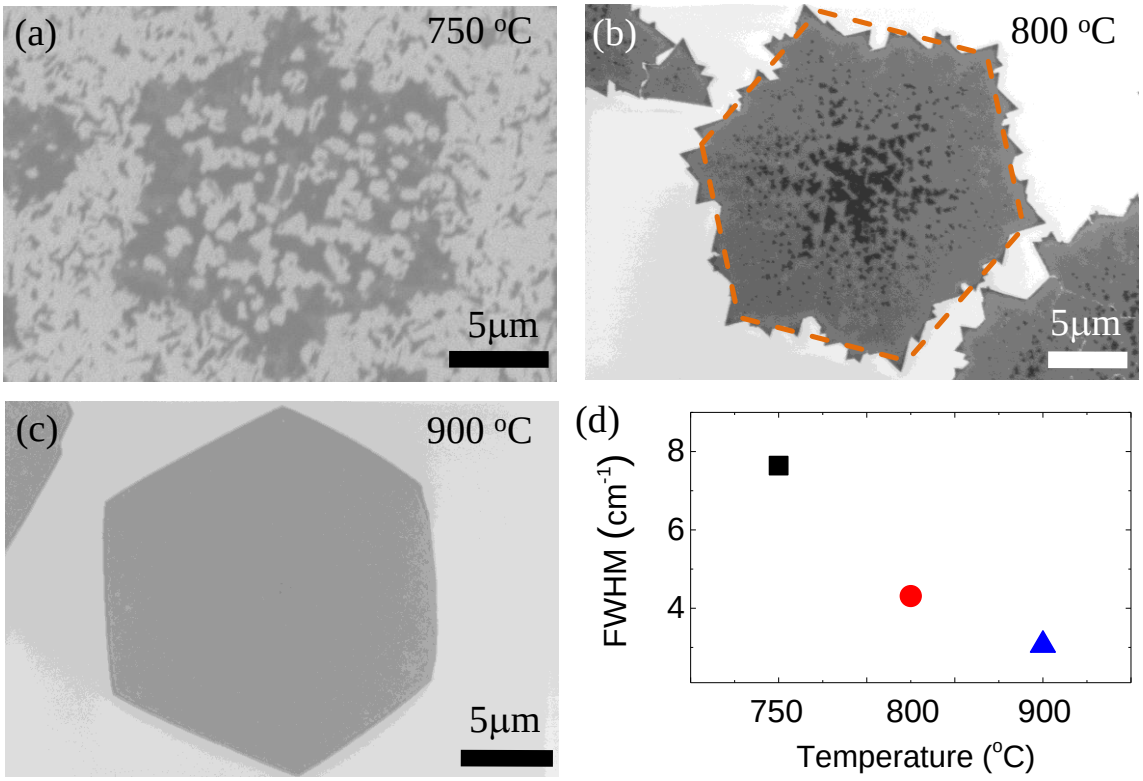

Figure 3.4: SEM micrographs (a-c) and FWHM as calculated from Raman spectra (d) showing the improvement of the crystallinity with increasing growth temperature.

This structural transition can be attributed to the difference between the rate of adatom attachment to the edge of the growing aggregate and the rate of edge diffusion. In

the vapor-phase epitaxy of 2D TMDs, once the adatoms are adsorbed from the gas phase to the surface of the substrate, they randomly diffuse until they reach the edge of a growing crystal. Concurrently, the atoms already attached to the domain edges may diffuse along the perimeter to find the most thermodynamically stable configuration of its 2D crystal. This results in compact triangular or hexagonal domains governed by the trigonal prismatic crystal symmetry of 2H-$MoSe_2$ belonging to the D_{3h} group [57]. At low temperature, the edge diffusion is highly suppressed but the incoming adatoms continue to attach themselves to the domain edges predominantly via diffusion-limited aggregation (DLA). Because there is no effective reshaping due to reduced edge diffusion, the compact domains in Fig. 3.3 (a) branch out into fractals [Figure 3.3 (c)].

Interestingly, branching is also observed with increasing flux of the metal precursor. Figure 3.5 shows growth at 900 °C, but at higher flux, compared to Fig. 3.3 (a). As metal flux increases, the rate at which the adatoms arrive at the domain edge becomes higher. Although the edge diffusion still takes place at elevated temperatures, it may not be sufficient to ensure the re-arrangement of all incoming adatoms to a stable triangular (or hexagonal) configuration and hence the compact structure will ramify, as shown in Fig. 3.5. Figures 3.3 (c) and 3.5 (a) both show branched structures, but the domains in Fig. 3.5 (a) are dendritic in shape, where the needle-like central branches indicate the preferred growth directions. The mechanism for transition from fractals to dendrites in CVD growth is poorly understood, but in general, it is directly related to the growth rate and deposition flux [58,59]. Higher metal flux increases the number of preferred growth directions, and the high-temperature regime promotes the anisotropy of edge diffusion [60]. The adatoms, in addition to attachment to the edges, now also prefer to diffuse along the lowest-energy diffusion paths on the substrate, promoting the branching along the directions of the domain expansion, leading to dendritic $MoSe_2$ domains [61]. Figure 3.5 (b) shows that the branching prefers the three crystallographic orientations of a hexagon (shown as red dashed lines). This indicates that the growth still maintains the sixfold symmetric crystallographic structure with the axes meeting at the center. Because of the preference to specific

orientations, the growth mechanism can no longer be solely explained via the DLA model as that would predict growth along random directions [62].

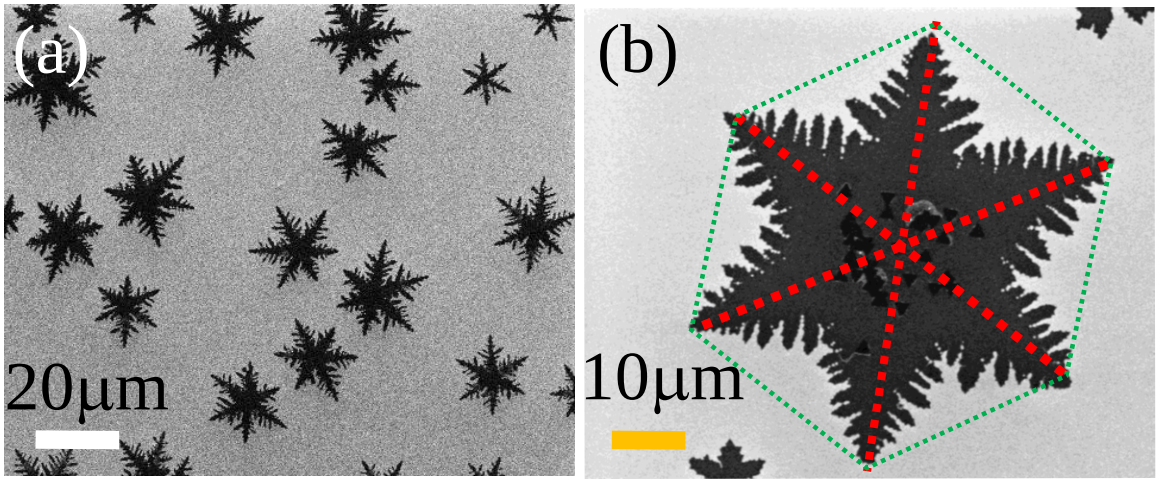

Figure 3.5: Effect of metal flux on compact to dendritic growth transition of 2D $MoSe_2$. SEM images showing (a) higher metal flux resulting in dendritic domains for growth at 900 ˚C (b) Zoomed in image of (a) clearly showing the branches.

Figure 3.6 (a,b) shows the fractal dimensions extracted from Fig. 3.3 (c) and 3.5 (a) respectively, using the box-counting method. A fractal dimension of 1.67 in the case of the domain shown in Fig. 3.3 (c) is in agreement with the expected value of 1.71 in the case of 2D DLA [63].

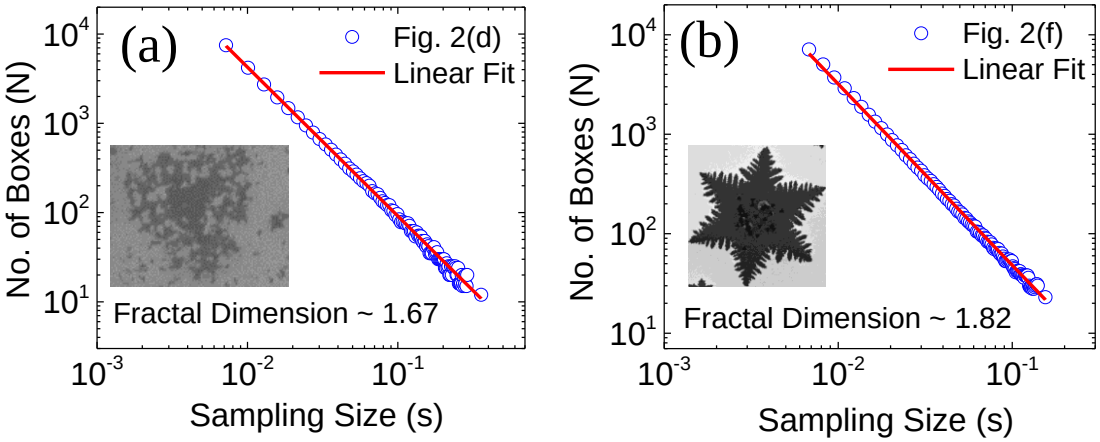

Figure 3.6: Fractal dimensions, corresponding to the images shown in insets, are calculated using the box counting method.

Fractal dimensions calculated from several other fractal $MoSe_2$ domains grown at 750 ˚C are also shown in Fig. 3.7. Corresponding SEM images are shown in insets (a-f) from six different locations on the $MoSe_2$ film moving downstream.

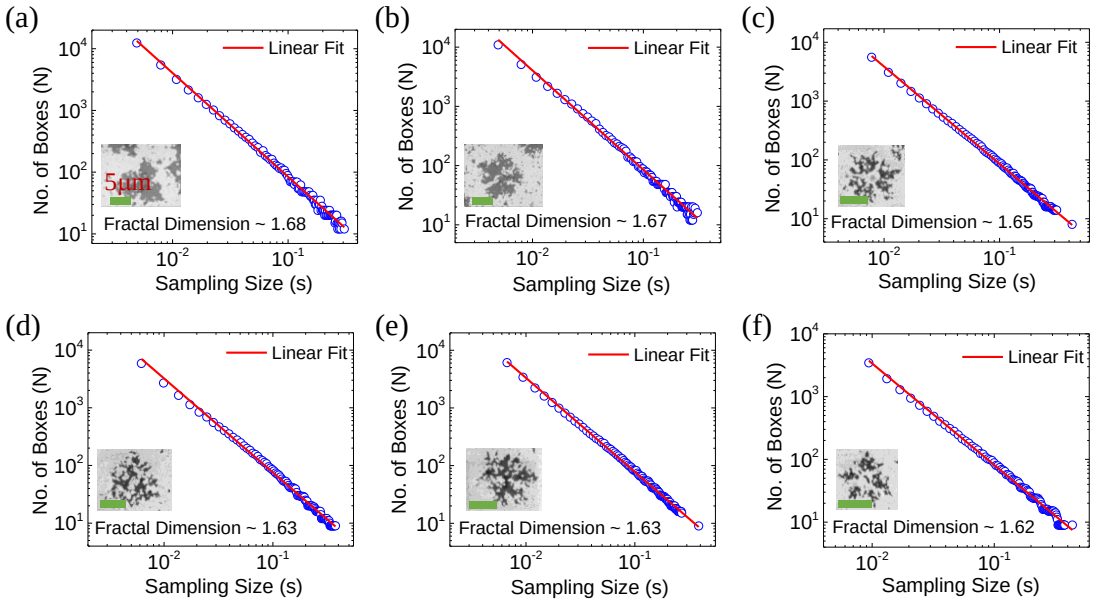

Figure 3.7: (a-f) Fractal dimensions, corresponding to the images shown in insets, are calculated using the box counting method. Scale bars for all the images are 5 μm.

For the dendritic domains, the fractal dimensions are ~1.80 [as shown in Fig. 3.6 (b)], which is higher than the expected value of 2D DLA. Growth progressing along the symmetry-governed preferred directions leads to more compact structures, hence larger fractal dimensions, compared to random fractals under 2D DLA. This further supports our claim that the dendrite formation is not entirely random and hence cannot be explained via DLA only. In addition, the side branches (yellow dashed lines) proceeding at an angle ~60° to the main branches confirm that the dendritic domains maintain the hexagonal crystal symmetry (Figure 3.8). A slight variation in the shape of branched domains is also observed in Fig. 3.8. This variation depends largely on the local ratio of Mo and Se and may vary with the location of the substrate. Similar observation has also been made for MoS_2 growth.

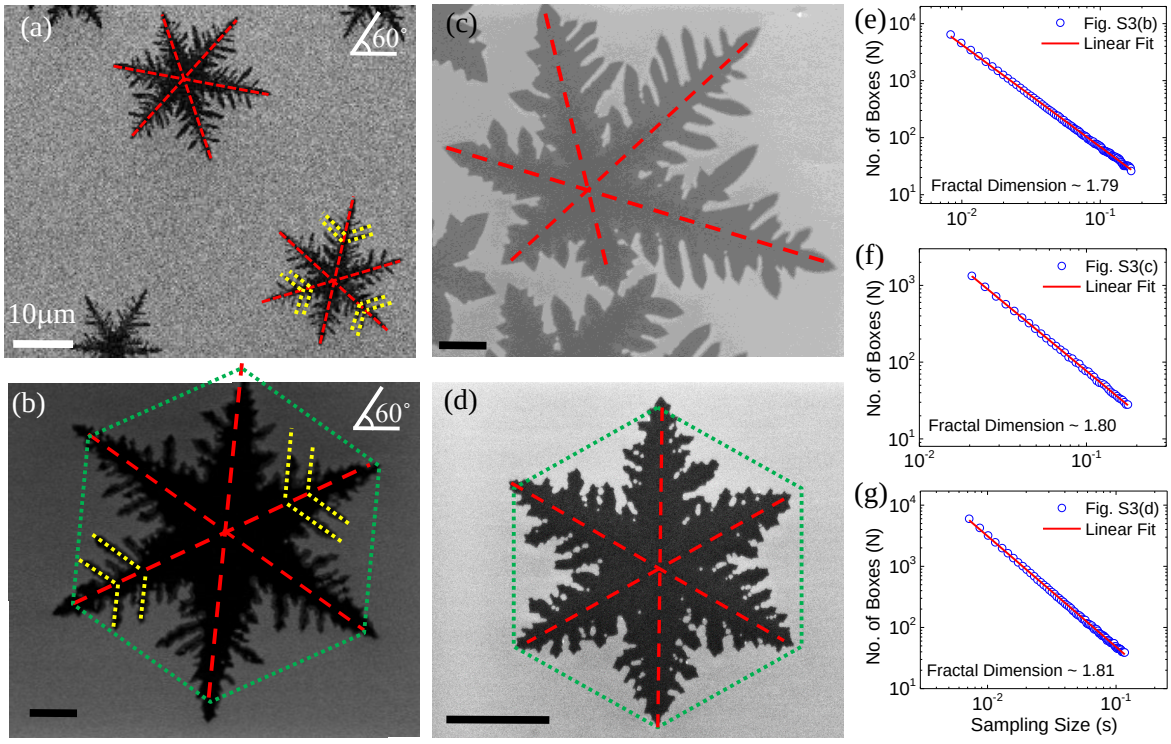

Figure 3.8: SEM micrographs of different $MoSe_2$ branched domains following six-fold symmetry (a-d). Branching occurs only at an angle of 60˚ with respect to the central needle branch. Fractal dimensions as calculated from the branched domains are shown (e-g).

Figure 3.9 shows the reproducibility of the compact, fractal and dendritic modes of $MoSe_2$ growth. Three different batches are shown in each case. For the compact mode, growth-1 has a majority of hexagonal domains, while growth-2 and growth-3 are dominated by $MoSe_2$ triangles. The size distributions corresponding to each growth (insets) show majority of the domains fall within the 10 – 20 μm range, thereby reasserting the homogeneity of the growths. Three different batches of fractals and dendrites are shown in Fig. 3.9 (b) and (c), respectively. Although the growth mode remains the same for each case, depending on the local flux and/or temperature, a variation in the shapes/sizes/densities of compact/fractal/dendritic domains are observed.

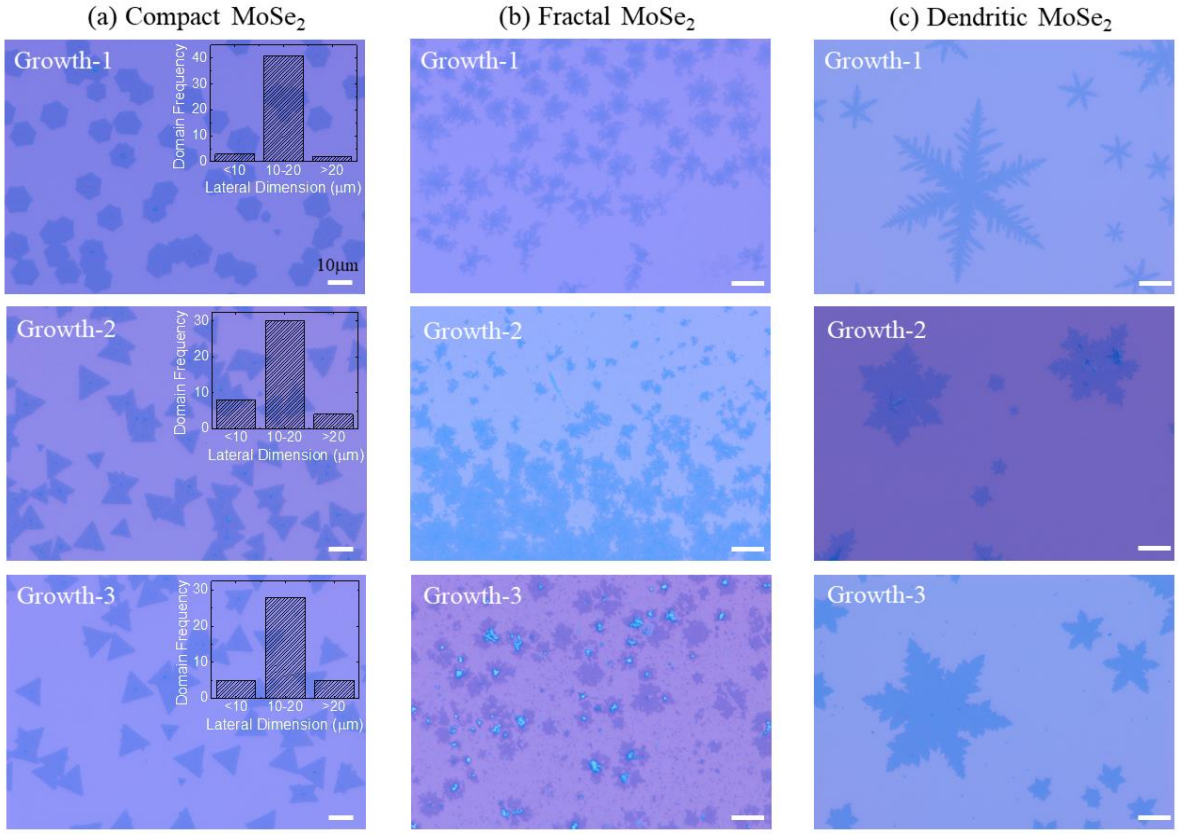

Figure 3.9: Reproducibility of different growth modes – (a) Compact, (b) Fractal, and (c) Dendritic. Insets in (a) show the size distributions of $MoSe_2$ compact domains.

Although growth at 900 °C produces compact domains as large as 30−40 μm [Figure 3.3 (a)], growth at higher temperature (1000 °C) leads to reduced domain sizes while still maintaining a compact triangular shape, as shown in Fig. 3.10. This is consistent with the theory that at higher substrate temperature, the rate of desorption will increase, so most of the adatoms that get adsorbed on the substrate will now have enough energy to leave the substrate, resulting in diminished domain sizes as shown in Fig. 3.10 (a). Figure 3.10 (b) shows growth at a high metal flux regime. As previously observed in Figure 3.5 (a), higher metal flux at 900 °C leads to transition from compact to dendritic growth. At 1000 °C, however, the added thermal energy facilitates the edge diffusion of the excess adatoms (because of higher metal flux) and the growth reverts to the compact mode. In addition, at elevated temperature, we see vertical three-dimensional (3D) growth being promoted and multiple islands being formed on the domains, as shown in Fig. 3.10 (a,b).

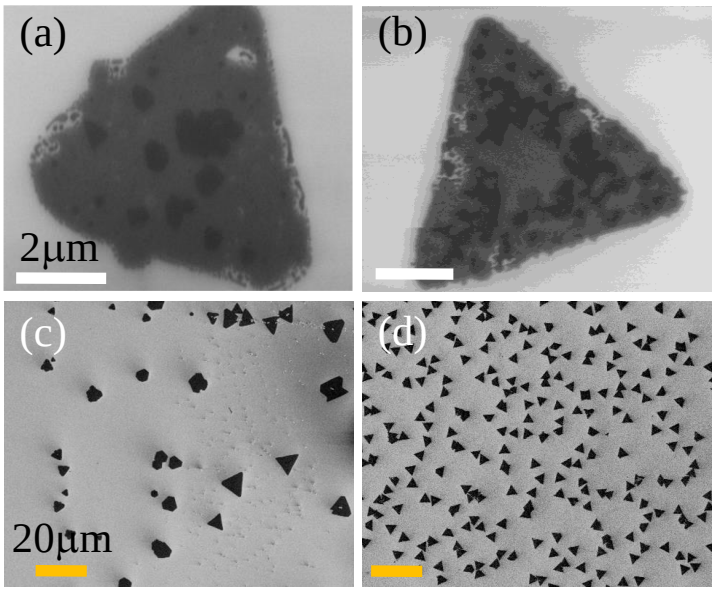

Figure 3.10: Effect of temperature and metal flux on vertical growth of $MoSe_2$. SEM images showing (a) 3D island formation on $MoSe_2$ domains grown at 1000 ˚C. (b) Higher metal flux at 1000 ˚C leading to more nucleation of 3D islands. Corresponding zoomed out SEM images in the panel below [(c) & (d)] show nucleation density of the grown domains. Scale bars are 2 μm (white) for the upper panel and 20 μm (yellow) for the lower panel.

AFM images and height profiles of domains grown under a higher temperature and flux regime are shown in Fig. 3.11, indicating 3D island growth. The growth mechanism to form 3D islands is explained in further detail in the following sections.

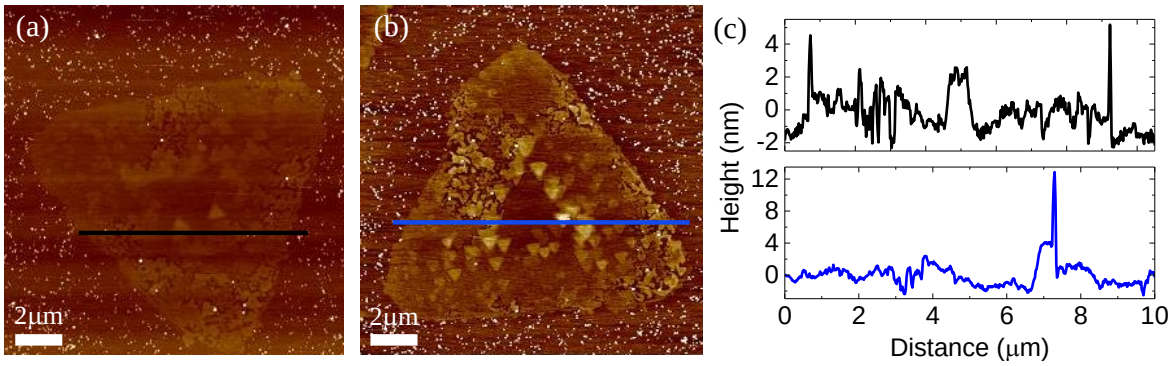

Figure 3.11: (a-b) AFM images and (c) corresponding height profiles from $MoSe_2$ samples grown at 1000 ˚C with higher metal flux.

The growth duration has an effect similar to that of temperature. Growth for a shorter duration (5 min) yields random shapes, as shown in Fig. 3.12 (a), which transition to triangular domains as the temperature is increased to 950 °C [Figure 3.12 (b)] owing to the added thermal energy that promotes edge diffusion.

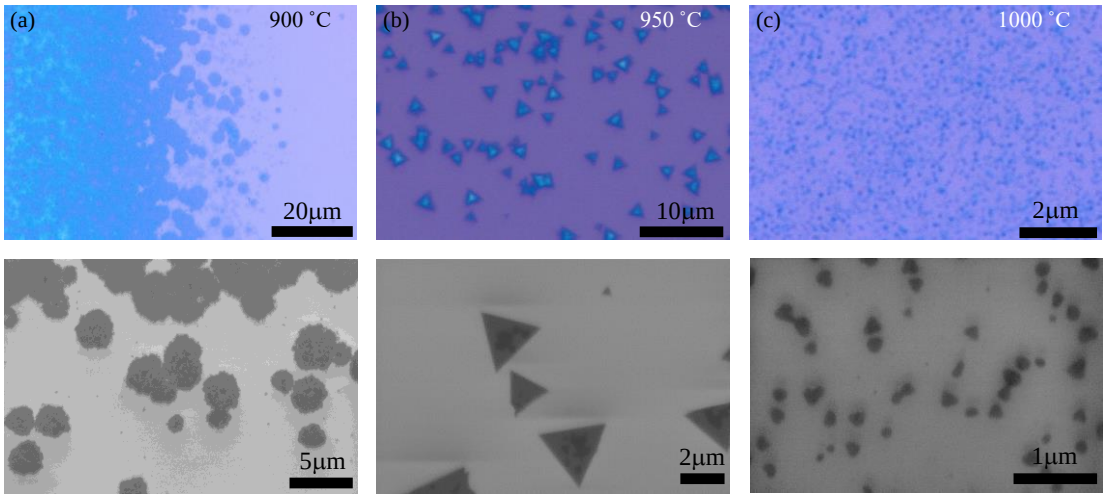

Figure 3.12: Optical (upper panel) and SEM (lower panel) micrographs from $MoSe_2$ growth for 5 min on Si/SiO_2 substrates at different temperatures – (a) 900 ˚C, (b) 950 ˚C, and (c) 1000 ˚C.

The elevated temperature, however, gives rise to island growth similar to that shown in Fig. 3.10. When the substrate temperature is increased further (1000 °C), multilayer $MoSe_2$ domains of triangular shape are observed [Figure 3.12 (c)]. A reduction in domain sizes results from increased desorption at elevated substrate temperature.

Figure 3.13 shows the $MoSe_2$ growth on Si/SiO_2 substrates at 900 ˚C for different growth durations. All other growth parameters including the Se flux were kept the same for all of them. As expected, the coverage increases with increasing growth time. With increasing growth time, an incomplete shape of $MoSe_2$ domain in Fig. 3.13 (a) turns into a symmetry-driven hexagonal compact domain, in Fig. 3.13 (b). As we keep growing [for example, 20 min in Fig. 3.13 (c)] individual triangular and/or hexagonal $MoSe_2$ domains grow laterally and merge with the neighboring domains. This results in different types of grain boundary defects (e.g., mirror twins, tilt twins, *etc*.). Presence of grain boundaries due to the merging of individual $MoSe_2$ domains are evident in Fig. 3.13 (c).

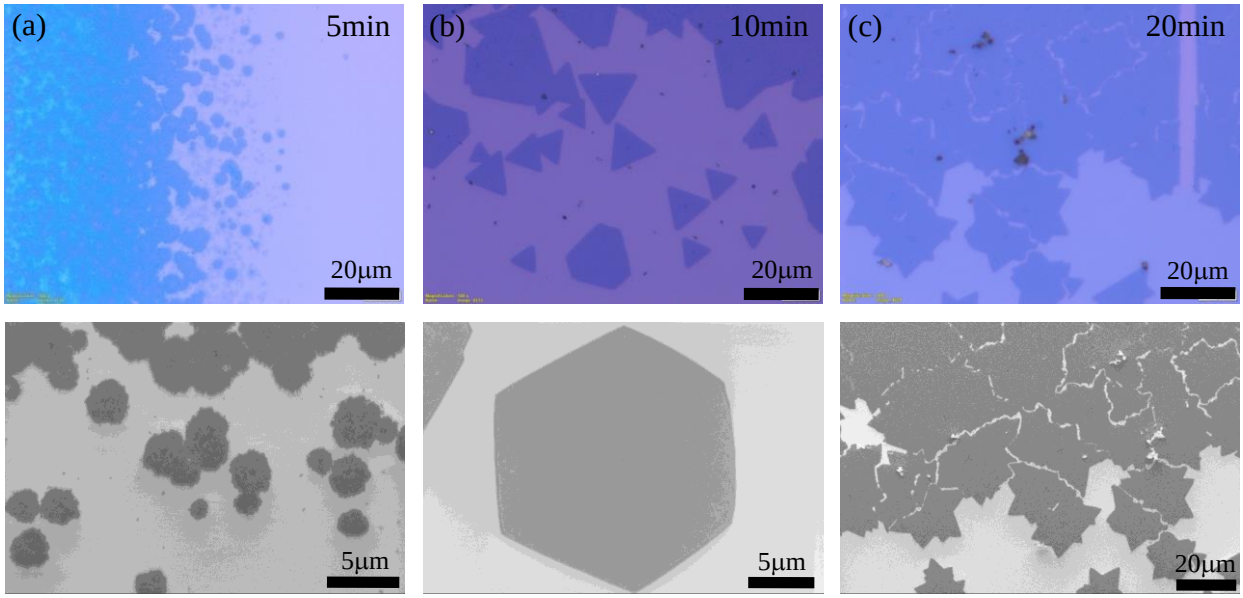

Figure 3.13: Optical (upper panel) and SEM (lower panel) micrographs from $MoSe_2$ growth on Si/SiO_2 substrates at 900 ˚C for different growth time – (a) 5 min, (b) 10 min, and (c) 20 min.

These grain boundaries are one of the major concerns associated with TMD growth as they serve as sinks and sources for point defects and dislocations and are also expected to degrade electrical performance. The likelihood of the grain boundary formation also increases with higher nucleation density. Hence, it is important to suppress the nucleation density as much as possible to keep the grain boundary formation at a minimum [64]. During CVD growth, several chemical and physical processes, for example, surface/ gaseous reactions, adsorption, desorption, nucleation, and so forth, occur simultaneously on the substrate surface [65]. Nucleation initiates with the formation of a cluster comprising a small number of closely packed molecules with a high surface area-to-volume ratio. This ratio decreases as more and more molecules attach to that cluster, minimizing the surface free energy, thereby reaching a critical size, and hence, stable nuclei are formed [66]. As the growth progresses, it becomes more favorable for the adatoms to attach themselves to the growing aggregate rather than forming individual nucleation sites and hence, the domains grow larger in size [Figure 3.3 (a)]. When the growth temperature is reduced to 750 °C, the desorption rate falls, leading to the formation of numerous nucleation sites [Figure 3.3 (c)]. In the higher flux regime, a larger number of adatoms reaching the substrate lead to more nucleation sites. This is shown in Fig. 3.5 (a) where a higher density is observed in comparison to that in Fig. 3.3 (a). Growth at 1000 °C limits nucleation because of higher desorption at higher substrate temperature [as observed in Fig. 3.10 (a,c)], whereas an increase in metal flux at 1000 °C shows more nucleation, as expected [Figure 3.10 (b,d)].

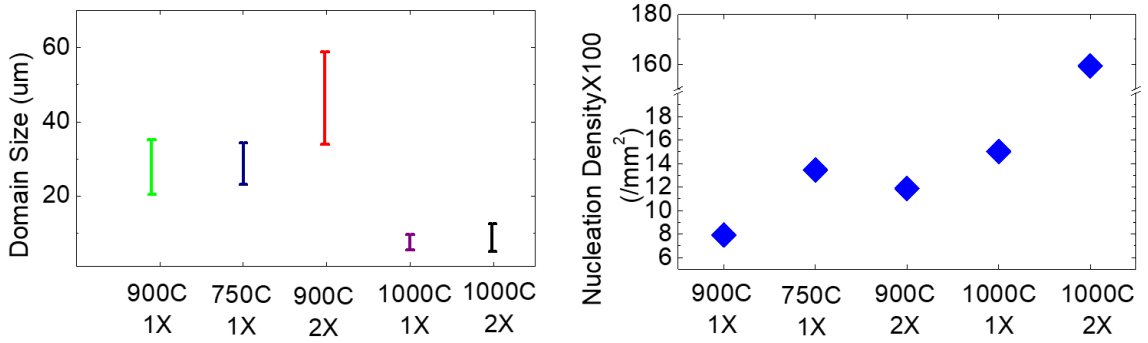

Figure 3.14: (a) Domain size and (b) nucleation density under different growth conditions.

When the metal flux is increased, the tendency to reach the critical nuclei size is higher, and hence, the nucleation density increases. The average domain sizes and nucleation density corresponding to different growth conditions are quantitatively represented in Fig. 3.14 and it clearly shows the lowest nucleation density of uniform monolayer domains under the optimized growth condition.

3.4 2D TO 3D GROWTH: EFFECT OF CHALCOGEN ENVIRONMENT

Compared to planar graphene, CVD growth of TMDs is somewhat more complex because there are two different types of atoms involved in the growth. The distribution of adatom concentration and growth rate can be quantitatively given using the following diffusion equation [67]:

$$\frac{\partial c_n}{\partial t} = D_n \nabla^2 c_n + F_n - \tau_{d,n}^{-1} c_n$$

where c_n is the number of adatoms, D_n is the diffusion coefficient, F_n is rate of adatom supply and τ_d is effective lifetime of adatoms before desorption. This diffusion equation suggests that if the first layer reaches a certain critical size before the second layer starts to grow then the vertical growth can be inhibited. The diffusion length λ_d of the adatoms within their lifetime τ_d also has a critical role in controlling thickness. Hence by tuning F and λ_d, lateral growth can be achieved. Transition metal atoms are much heavier than the chalcogen atoms and thus, compared to Se, Mo can travel for a much longer time on the substrate before getting desorbed [68]. To compensate for this large difference in surface diffusion behavior, the ratio of chalcogen to metal should be tuned in such a way that there are always enough chalcogen atoms to passivate the incoming Mo atoms. This can be achieved by controlling either the substrate temperature and/ or the chalcogen environment. At higher temperature, the rate of desorption also increases, so Se atoms get more easily desorbed leaving behind unpassivated Mo atoms that bond with other Mo atoms forming metal clusters and hence contributing to vertical growth (as shown in Fig. 3.10). Figure 3.15 (a) shows a SEM image of a uniform 2D single-crystal $MoSe_2$ domain grown in a Se-rich environment. The presence of Se atoms in abundance around the growing domain ensures that the Mo atoms that undergo attachment at the domain edges bond with Se atoms

only. This will ensure a near-dangling bond-free surface formation which is a critical condition required for the lateral growth to occur. The height profile along the line drawn on a $MoSe_2$ domain [as marked on the AFM image in Fig. 3.15 (b)] confirms uniform lateral growth, as shown in Fig. 3.15 (c).

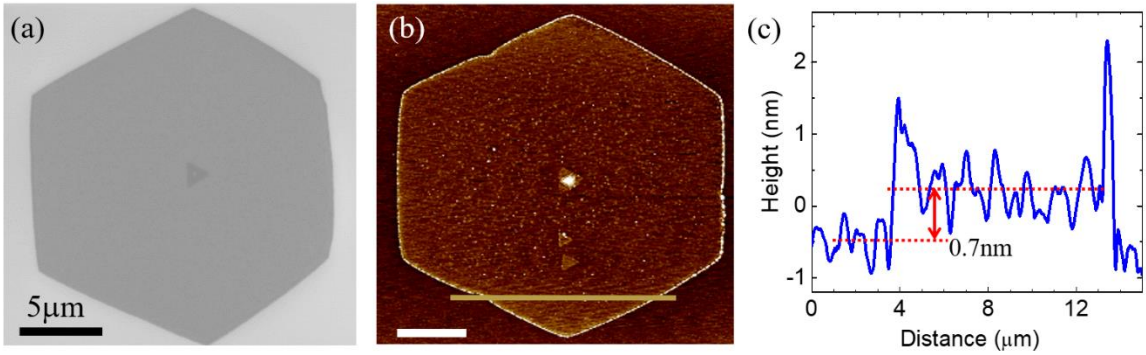

Figure 3.15: Effect of Se-environment on $MoSe_2$ growth transition from 2D to 3D. A monolayer domain of compact hexagonal structure grown under Se-rich condition: (a) SEM, (b) AFM and (c) the height profile across the yellow line marked on (b). Scale bars for all the images are 5 μm.

On the other hand, under a Se-deficient condition [Figure 3.16 (a)], probability of Mo atoms attached to the domain edges to bond with other incoming Mo atoms becomes higher because of the limited availability of Se atoms. This metal clustering due to incomplete Se passivation of Mo nuclei leads to 3D island growth [23]. In addition to the Se onset temperature, chalcogen flux can also be varied by changing the Se evaporation temperature (more details are described in the Experimental Methods section). Selenium evaporation at 220 °C (instead of 300 °C as compared to the optimized growth condition) also creates a Se-deficient environment for 3D growth to occur.

The AFM image [Figure 3.16 (b)] and the height profile along the line drawn on the AFM image in Fig. 3.16 (b) indicate the 3D vertical island growth [Figure 3.16 (c)], in

contrast to the uniform thickness of ~0.7 nm, corresponding to a monolayer height of $MoSe_2$, as shown in Fig. 3.15 (c).

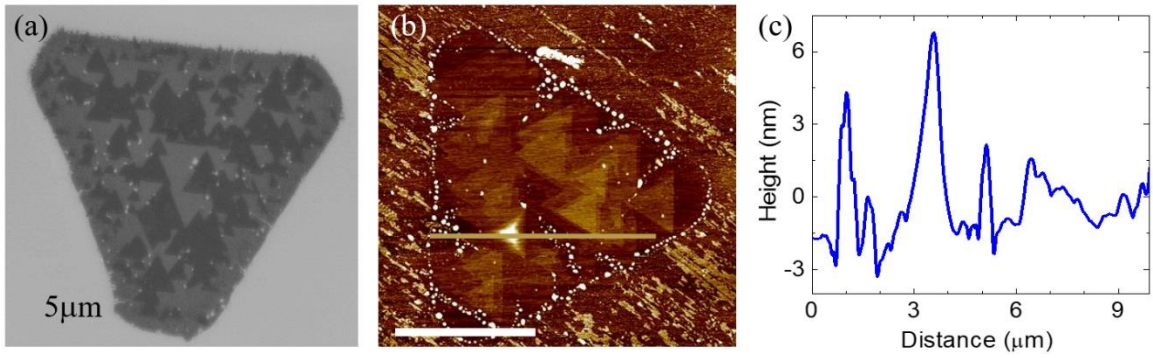

Figure 3.16: Effect of Se-environment on $MoSe_2$ growth transition from 2D to 3D. Growth under Se-deficient condition leads to 3D island formation on compact 2D domain: (a) SEM, (b) AFM and (c) height profile across the yellow line marked on (b). Scale bars for all the images are 5 μm.

The mechanism of the lateral versus vertical growth is schematically shown in Fig. 3.17 (a,b), highlighting the influence of the chalcogen environment.

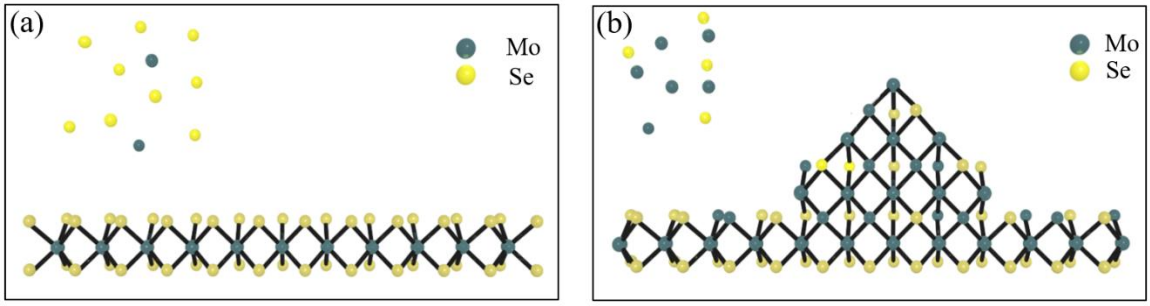

Figure 3.17: Effect of Se-environment on $MoSe_2$ growth transition from 2D to 3D. A schematic showing the mechanism behind the (a) lateral growth under Se-rich condition and (b) 3D island growth under Se-deficient condition.

To investigate this further, XPS measurements were carried out and the elemental compositions of $MoSe_2$ and WSe_2 are confirmed from the predominant peaks of Mo/W and Se, as shown in the survey spectra [Figure 3.18]. The spectra show intense Mo-3p, Mo-3d, W-4p, W-4f, Se-3p, and Se-3d photoemission features, in addition to Se-LMM Auger peaks.

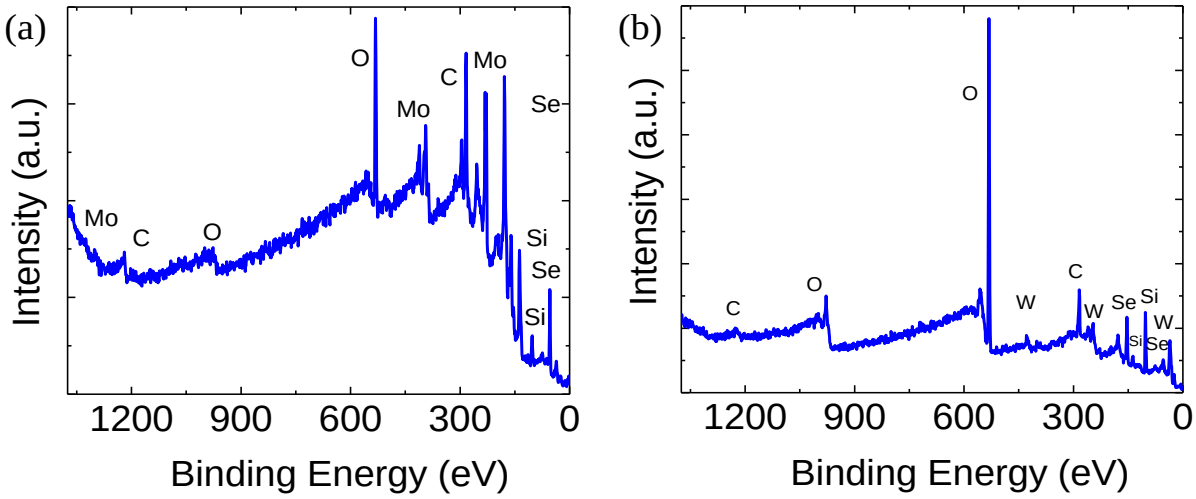

Figure 3.18: XPS survey spectra from (a) $MoSe_2$ and (b) WSe_2 grown on Si/SiO_2 substrates.

Figure 3.19 shows the high-resolution XPS spectra for $MoSe_2$ grown under Se-rich and Se-deficient conditions. The binding energies of 228.5 and 231.6 eV corresponding to Mo-$3d_{5/2}$ and Mo-$3d_{3/2}$ peaks, shown in Fig. 3.19 (a), for an $MoSe_2$ sample grown under Se-rich conditions are shifted from the binding energy of 232.4 and 235.9 eV for hexavalent Mo in MoO_3, suggesting a reduction to the +4 oxidation state of Mo in $MoSe_2$. Similarly, Se-$3d_{5/2}$ (54 eV) and Se-$3d_{3/2}$ (54.8 eV) in Fig. 3.19 (b) correspond to the −2 oxidation state of Se. These values of Mo and Se peak positions closely match with those reported in the literature [24]. The integrated peak area of Mo-3d and Se-3d are calculated, and a Se-to-Mo ratio of 1.98 is obtained, which suggests that the grown $MoSe_2$ is reasonably stoichiometric. Under Se-deficient conditions, the binding energies of Mo-$3d_{5/2}$ and Mo-$3d_{3/2}$ are found to be at 228.1 and 231.2 eV and those of Se-$3d_{5/2}$ and Se-$3d_{3/2}$ are

found to be at 53.7 and 54.5 eV, as shown in Fig. 3.19 (c,d). The shift of the Mo-$3d_{5/2}$ peak from 228.5 eV under Se-rich conditions to 228.1 eV under Se-deficient conditions suggests the presence of a combination of different oxidation states, which is a result of metal clustering under Se-deficient conditions [69]. This is further confirmed by the Se-Mo ratio of 1.68 in the Se-deficient $MoSe_2$, clearly indicating abundance of Mo-rich nuclei and incomplete Se passivation.

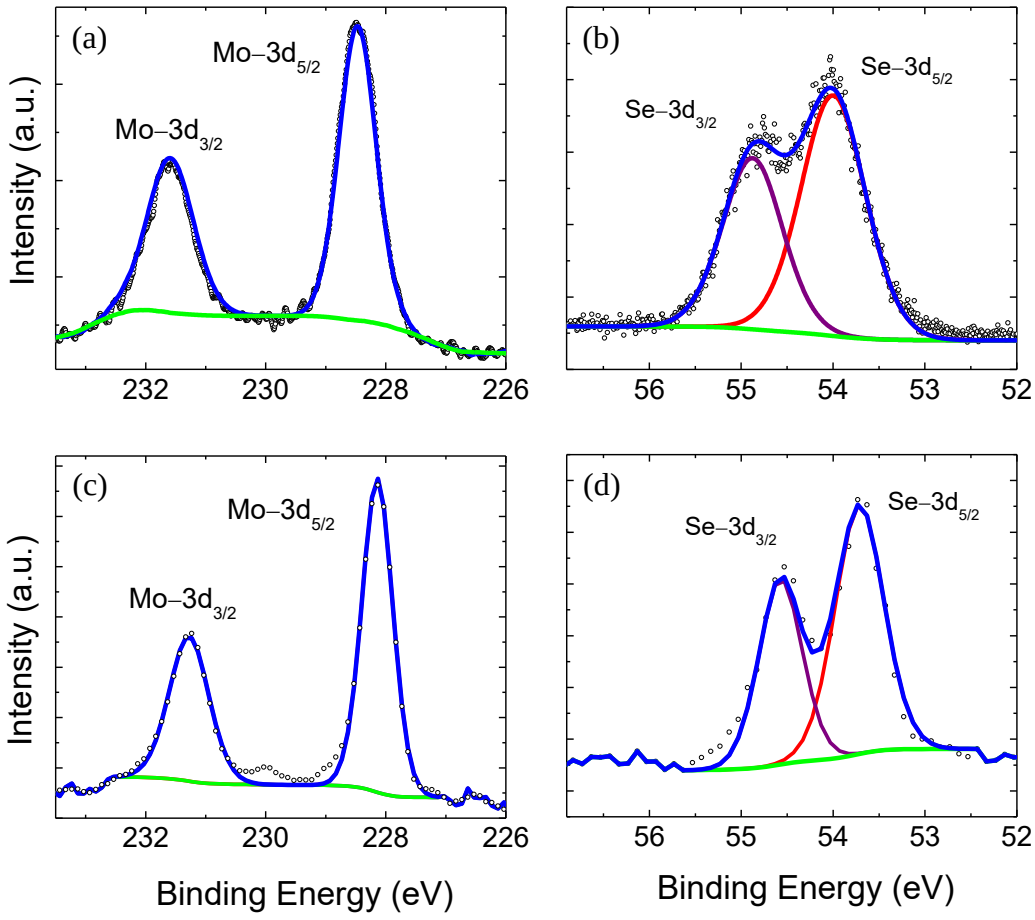

Figure 3.19: High-resolution XPS spectra of $MoSe_2$ thin films grown under different Se environments. Mo-3d and Se-3d core-level peaks of $MoSe_2$ grown under (a, b) Se-rich condition and (c, d) Se-deficient condition, respectively. A Mo/Se ratio of 1:1.98 (a, b) and 1:1.68 (c, d) are extracted from the area fit (solid lines) to the experimental data (○). A close-to-the-ideal ratio of 1:2 in Se-rich condition indicates a fairly stoichiometric $MoSe_2$, whereas, the deviation in case of (c) and (d) is due to incomplete Se-passivation of Mo atoms leading to 3D island growth.

3.5 APPLICABILITY TO OTHER TMDS: WSe_2

To verify the repeatability of the predicted trend in controlling the morphology and 2D-to-3D growth transitions for different TMD systems, WSe_2 growth was carried out under similar conditions. At 1000 °C, although growth under a Se-rich environment guides the domain to attain a uniform monolayer compact hexagonal shape [Figure 3.20 (a)], under Se deficient conditions, several 3D multilayer islands emerge on the WSe_2 domains [Figure 3.20 (b)]. At 900 °C, the domain assumes a fractal structure, as shown in Fig. 3.20 (c).

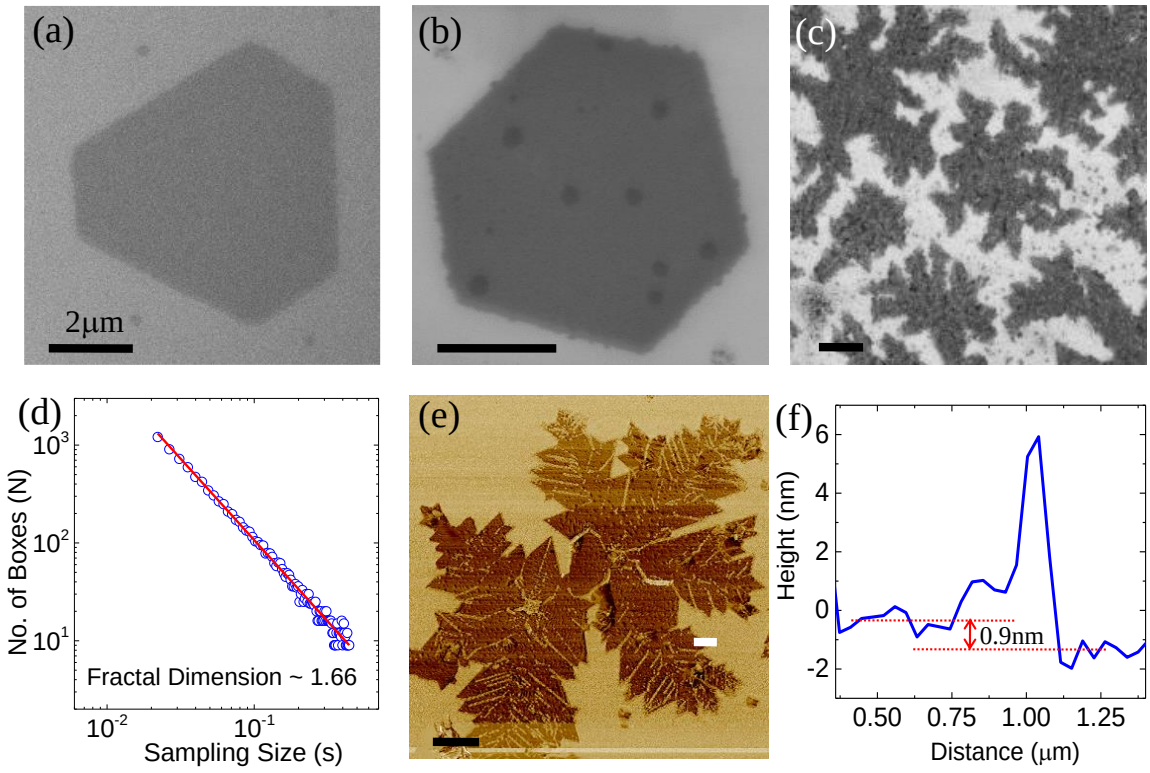

Figure 3.20: WSe_2 growth on Si/SiO_2 under different growth conditions. SEM micrographs show growth at 1000 ˚C leading to (a) compact hexagonal domains of uniform monolayer under Se-rich condition and (b) 3D multilayer islands under Se-deficient condition. (c) & (d) Growth at 900 ˚C leading to fractal growth with a dimension of 1.66, respectively. AFM image and height profile (across the white line drawn) are shown in (e) and (f), corresponding to monolayer WSe_2, respectively. Scale bars for all the images are 2 μm.

A fractal dimension of about 1.66 is calculated [shown in Fig. 3.20 (d)] which is in agreement with the 2D DLA growth mechanism. A 2D monolayer fractal domain is evident from the AFM image and the height profile, shown in Fig. 3.20 (e,f), respectively. These results suggest that higher substrate temperature is necessary to increase the adatom mobilities, suppress stochastic aggregation, and achieve compact hexagonal-/triangular-shaped structures. However, enhanced surface desorption at higher temperature requires a Se-rich condition to achieve 2D compact growth.

3.6 SUMMARY

In conclusion, we have synthesized large-area single-crystal monolayers of $MoSe_2$ and WSe_2 by CVD and have demonstrated the control of growth parameters to tune the morphology and thickness of the grown film. The effects of varying parameters such as substrate temperature and metal flux on ramification of compact structures are explored. Two different branched structures, fractals and dendrites, grow at reduced temperature and elevated metal flux, respectively. Although fractals obey the DLA mechanism, the dendrites with a higher fractal dimension show an anisotropic growth along the three crystallographic orientations of a hexagon. The high temperature and low-flux regime of growth favors the lower nucleation density and hence provides a pathway to minimize grain boundaries. However, when the growth temperature is increased further, the domain sizes are reduced because of increased desorption, and the vertical growth is promoted. 3D growth is also promoted by incorporating insufficient Se atoms during the growth, where metal-to-metal bonding due to incomplete Se passivation yields islands of multilayer domains. The stoichiometry and chemical composition of the grown films, investigated through XPS measurements, reveal that the near perfect stoichiometry of the film grown under a chalcogen-rich environment changes to sub-stoichiometric film under chalcogen-deficient conditions which is indicative of metal clustering. These studies provide a deeper understanding into the complex growth mechanism of TMDs and hence pave a pathway for controlled CVD growth.

Chapter 4: Role of Hydrogen in Suppressing Secondary Nucleation in Chemical Vapor Deposited MoS_2

4.1 INTRODUCTION

In this work we present a systematic study to synthesize MoS_2 monolayer film using APCVD under various combinations of three different carrier gases: N_2, Ar and H_2. Several characterization techniques such as Raman and photoluminescence (PL) spectroscopy, atomic force microscopy (AFM), scanning electron microscopy (SEM) are used to investigate the changes in thickness, domain size, and the crystal quality as the carrier gas composition are varied. The elemental composition and stoichiometry are compared using X-ray photoelectron spectroscopy (XPS). To understand the effect of H_2 incorporation we employ a phase field model to support the experimental findings. Our work provides a deeper insight into the underlying growth mechanisms that help us understand the effect of a reducing environment in achieving more uniform 2D growth of pristine MoS_2.

4.2 CVD MoS_2 GROWTH CHEMISTRY:

MoS_2 growth is performed under atmospheric pressure on Si/SiO_2 substrates using the precursors MoO_3 and Sulfur powder at 850 °C for 5 min. More details of the growth process can be found in the method section (Section 2.2.2.1). During CVD growth the reaction between the solid phase precursors MoO_3 and S occurs as follows [19]:

Much of the discussions, results and figures presented in this Chapter have been adapted from the following reference: Sayema Chowdhury et al. *"Role of hydrogen in suppressing secondary nucleation in chemical vapor deposited MoS_2"* (manuscript in preparation). The dissertator, S. Chowdhury, conceived and designed the experiments, conducted growths, carried out material characterization and analysis and largely wrote the manuscript with contributions from all the authors.

$$2MoO_3 + 7S \rightarrow 2MoS_2 + 3SO_2 \text{……..(1)}$$

In an inert atmosphere, MoO_3 is partially reduced by sulfur vapor to form volatile suboxide species MoO_{3-x}, which is further sulfurized to form MoS_2, similar to the reaction of WO_3 and S as reported by Zhang et al [70].

Figure 4.1 shows APCVD growth of MoS_2 under three different carrier gases: Ar, N_2, and H_2 (hereafter referred to as Ar-MoS_2, N-MoS_2 and H-MoS_2, respectively). When Ar is used as the carrier gas, MoS_2 domains range in size up to 200-300 μm and have jagged edges, as seen in Fig. 4.1 (a). In addition, many multilayer islands form resulting in non-uniform thickness. Significant number of secondary islands are also seen on MoS_2 domains grown under N_2 environment [Fig. 4.1(b)].

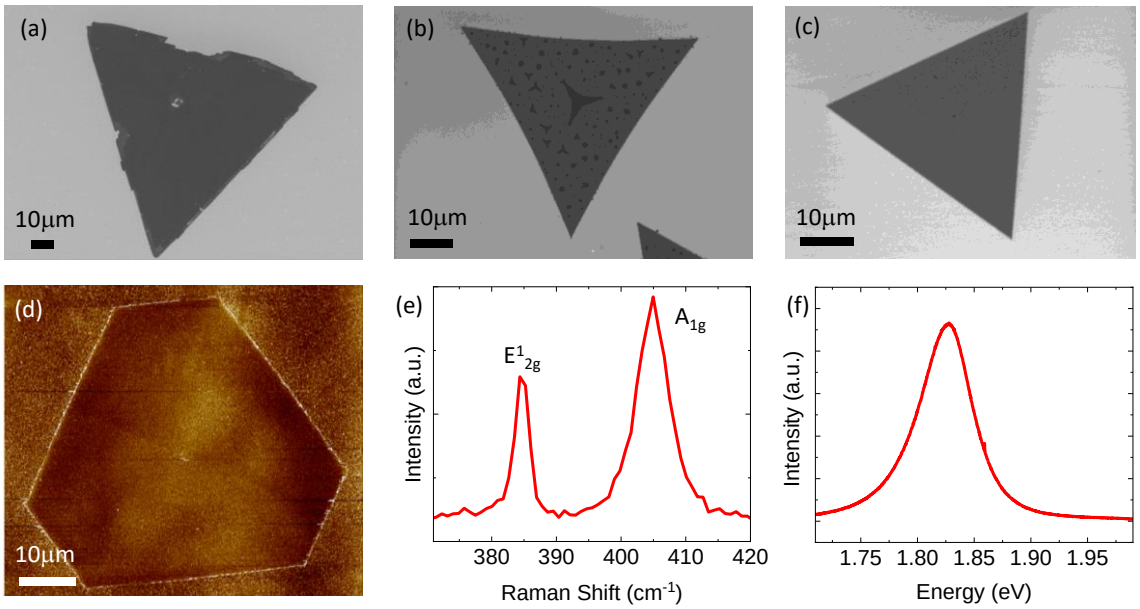

Figure 4.1: Scanning electron microscopy images of MoS_2 grown using carrier gas (a) Ar (b) N_2 and (c) H_2. (d) AFM image of an MoS_2 domain grown using H_2 carrier gas. (e-f) Corresponding Raman and PL spectroscopy images respectively.

Switching to H_2 as the carrier gas provides a reducing environment for the CVD reaction to occur resulting in domains with smooth edges, sharp corners and very little to

no multilayer growth [Fig. 4.1(c)]. A uniform, atomically flat surface of MoS_2 grown using H_2 carrier gas is seen in AFM studies [Fig. 4.1(d)]. Similar observation has been made previously by Yoo et al, where a small percentage of H_2 introduced in the growth chamber yields a "cleaner" domain [71]. H_2 has a very important benefits: H_2 leads to effective reduction of the oxide based precursor, according to Eqn. (2), resulting in fewer intermediate oxides and lower number of unsaturated Mo bonds, thus reducing the overall number of dangling bonds which can otherwise act as nucleation centers for subsequent layers [70]; secondly, it can increase the reaction speed [72], thereby moving the growth more into the kinetics-limited regime which favors thermodynamically stable geometry of a regular triangular shape [73]. We elaborate on this difference in the later sections.

$$MoO_3 + 3S + H_2 \rightarrow MoS_2 + 3SO_2 + H_2O \text{……..(2)}$$

Raman spectrum from MoS_2 grown using H_2 as the carrier gas shows two distinct characteristic peaks at ~386 cm^{-1} and ~406 cm^{-1} corresponding to Mo-S phonon modes E^1_{2g} (in-plane) and A_{1g} (out-of-plane) [Fig. 4.1(e)]. The peak difference of ~ 20 cm^{-1} indicates monolayer MoS_2 which is further confirmed by the sharp distinct PL peak at 1.8 eV [Fig. 4.1(f)] [2]. The narrow FWHM (~.05 eV) is indicative of high crystalline quality of MoS_2.

4.3 XPS ANALYSES COMPARING MoS_2 GROWN USING CARRIER GASES: AR, N_2 AND H_2

The elemental composition, oxide fraction and pristine nature of the MoS_2 film are evaluated by XPS analyses. Fig 4.2 shows the high-resolution Mo-3d (which overlaps with the S-2s) and S-2p spectra acquired on Ar-MoS_2 [Fig. 4.2(a)], N-MoS_2 [Fig. 4.2(b)] and H-MoS_2 [Fig. 4.2(c)]. The binding energies of Mo-$3d_{5/2}$ and Mo-$3d_{3/2}$ at ~229.9 and ~233 eV correspond to the Mo (IV) oxidation state of the disulfide, as previously seen in the case of pristine MoS_2. [2,74]

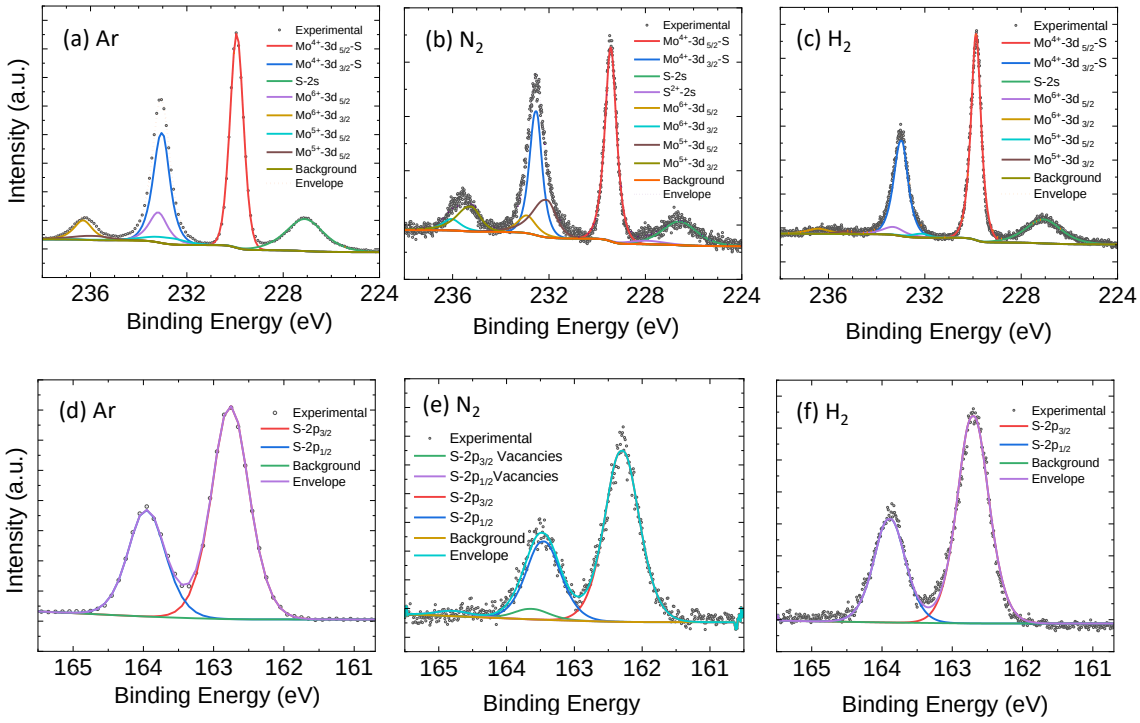

Figure 4.2: High-resolution Mo-*3d* XPS spectra of MoS_2 domains grown under different carrier gas compositions (a) Ar (b) N_2 and (c) H_2. (d-f) Corresponding high-resolution S-*2p* spectra.

In case of Ar-MoS_2 and N-MoS_2, in addition to the Mo(IV) peak corresponding to MoS_2, presence of a prominent Mo(VI) peak [at 236.4 eV in Figure 4.2(a-b)], indicates significant residual molybdenum trioxide in the films, presence of which results from using oxide-based precursor for CVD growth and has previously been reported [2]. Moreover, the N-MoS_2 has a prominent Mo-3$d_{3/2}$ peak at ~235 eV corresponding to the Mo(V) oxidation state of non-stoichiometric oxides. Conducting the growth in a reducing environment, by introducing H_2, strongly suppresses the Mo(VI) oxidation state, as observed in H-MoS_2 [Figure 4.2(c)] leading to a significantly decreased fraction of oxidized molybdenum in the near-surface region. The corresponding S-2*p* peaks are shown in Figure 4.2 (d-f). The S-2$p_{3/2}$ (162.3 eV) and S-2$p_{1/2}$ (163.4 eV) peaks correspond to the -2 oxidation state of S [2,74]. The presence of a second, shifted S (-2) doublet at 163.6 eV

for the S-$2p_{3/2}$ and 164.8 eV for the S-$2p_{1/2}$ in the S-2p region for the film grown in N_2 ambient indicates the presence of sulfur vacancies in the film. No SO_x doublets (which are located at 168-170 eV [75,76]) are present for any of the deposition atmospheres, indicating that oxi-sulfide intermediates are not formed. Thus, performing the growth in H_2 helps decrease the fraction of oxidized molybdenum and results in a more pristine MoS_2, whereas, in case of N-MoS_2 or Ar-MoS_2, the absence of a reducing environment leads to partial conversion of MoO_3 into MoS_2.

Figure 4.3 shows the relative percentages of various oxidation states of Mo: the XPS quantitative results clearly indicates that H-MoS_2 has the smallest fraction of the Mo(V) and Mo(VI) oxidation states corresponding to non-stoichiometric oxides and the native trioxide, respectively.

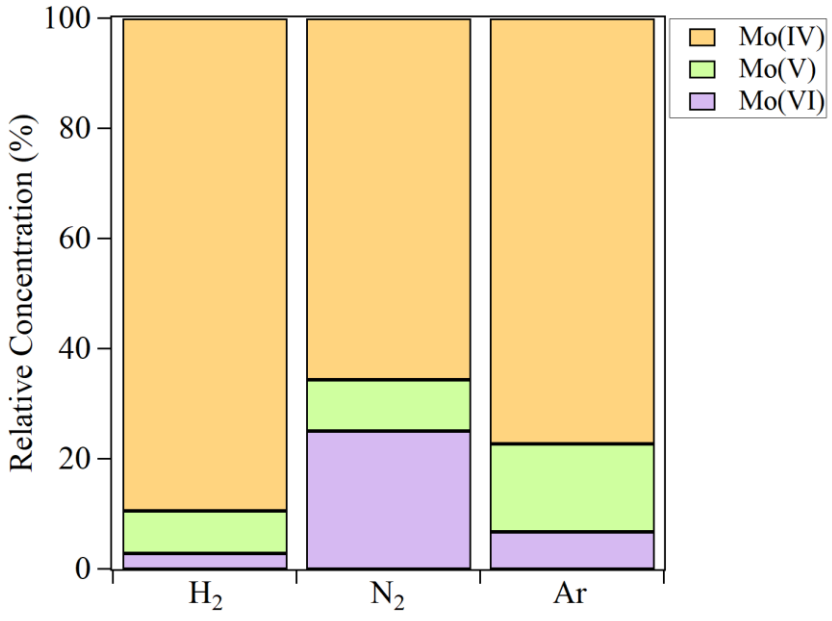

Figure 4.3: Comparison of relative composition of different oxidation states between MoS_2 grown using different carrier gases.

4.4 MORPHOLOGY OF MoS_2 DOMAINS WITH DIFFERENT CARRIER GAS COMPOSITION

Figure 4.4 shows SEM images of MoS_2 domains grown under different combination of carrier gasses with increasing percentage of H_2. For a combination of N_2/H_2 and Ar/H_2 with increasing H_2 percentages are shown in Fig. 4.4(a-e) and Fig. 4.4(f-j), respectively. The zoomed in SEM images corresponding to the domains in Fig. 4.4(a1-e1) are shown in Fig. 4.4(a2-e2). Similarly, zoomed in morphologies grown under Ar/H_2 in Fig. 4.4 (f1-j1) are shown in Fig. 4.4 (f2-j2). The H_2 induced reduction of the Mo^{6+} to Mo^{4+} results in more efficient conversion of oxides to sulfides leaving fewer dangling bonds that can otherwise act as nucleation centers for subsequent layers [37]. Hence, with increasing H_2 percentage, the nucleation density of secondary island decreases.

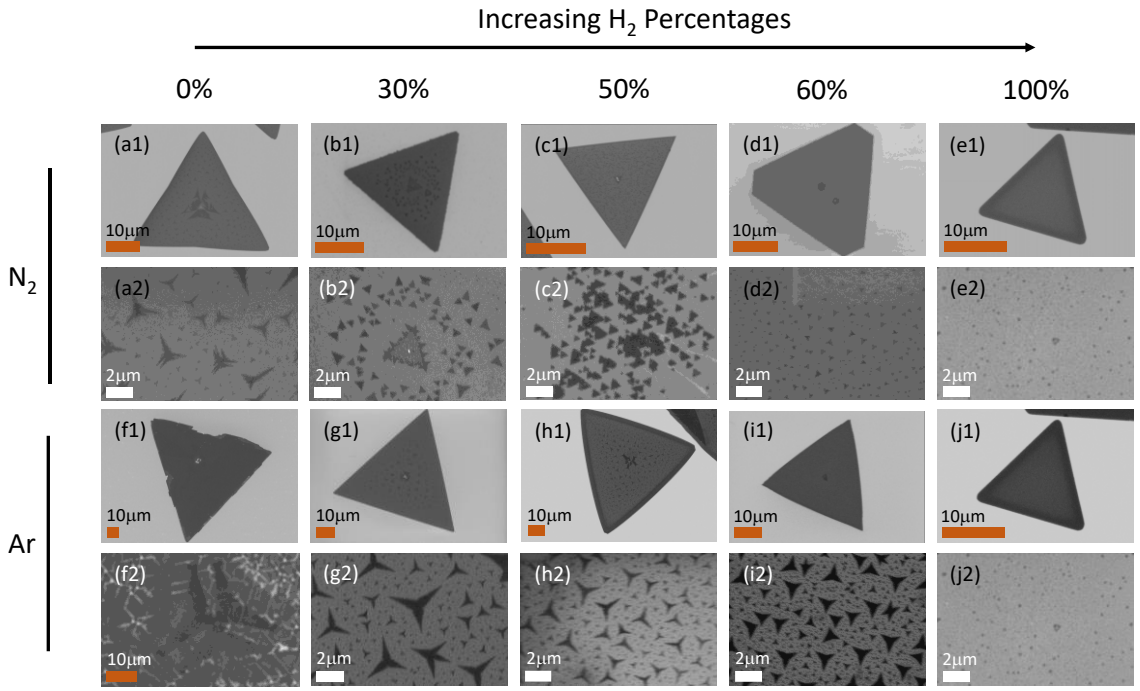

Figure 4.4: SEM images of MoS_2 domains grown under different combination of carrier gasses with increasing percentage of H_2 (left to right): (a-e) Combination of N_2/H_2 and (f-j) Ar/H_2. (a2-e2) Zoomed in SEM images corresponding to the domains in (a1-e1). (f2-j2) Zoomed in morphologies corresponding to domains in (f1-j1).

In addition to saturating dangling bonds on the primary monolayer domain surface, hydrogen also saturates dangling bonds at the edges, thereby limiting the lateral domain size [37]. Moreover, H_2 can slowly etch away the grown domain [77,78]. Both effects can thus restrict the primary domain to grow larger, as observed from Figure 4.4.

4.5 Effect of substrate on morphology of MoS_2 second layer

Interestingly, we observe that in addition to the size and density of these secondary islands, their shape also changes from dendritic to triangular as the percentage of H_2 increases. We attribute this transition to the effect of substrate surface on the growth. Dumcenco *et al.* [79]. reports that although van der waals epitaxy circumvents the requirement for lattice matched substrate, the substrate surface still dictates the nucleation of the growing material. For the growth of MoS_2 on highly polished sapphire substrate the van der waals interaction between closely lattice matched sapphire and MoS_2 control the lattice orientation of MoS_2. This results in growth of single crystal domains with edges oriented at multiples of 60° [79]. Similar substrate dependence has also been observed for the APCVD growth of 2D materials conducted on different substrates [80]. For *h*-BN growth on highly smoothened polished Cu substrate, Tay *et al.* has observed the influence of substrate surface morphology on the nucleation density, domain sizes and B/N-terminated edges [81]. Thus, pre-deposition substrate surface plays a crucial role in determining the growth mechanism as well as the overall morphology.

To understand more of the effect of carrier gases on controlling the growth morphologies, in Figure 4.5, we compare MoS_2 growth on Si/SiO_2 substrates carried out under H_2 and N_2 only. For the growth of H-MoS_2 the first layer (grown on Si/SiO_2 as substrate) have random azimuthal orientation [Figure 4.5(a)], but the subsequent secondary domains (grown on the primary MoS_2 domain as the substrate) grow with the edges oriented at multiples of 60° strictly following the crystal symmetry of the underlying monolayer MoS_2 [Figure 4.5(b)]. Similar uniform lateral 60º orientation of the secondary domains on randomly oriented first layer MoS_2 [Figure 4.5(c)] is also observed in case of N-MoS_2 [Figure 4.5(d)]. This confirms the role of underlying MoS_2 layer governing the growth of the secondary islands. However, unlike compact triangular secondary domains

on H-MoS_2, secondary domains on N-MoS_2 have a dendritic morphology. We attribute this variation on the role of carrier gases changing the condition of the substrate surface prior to the growth process.

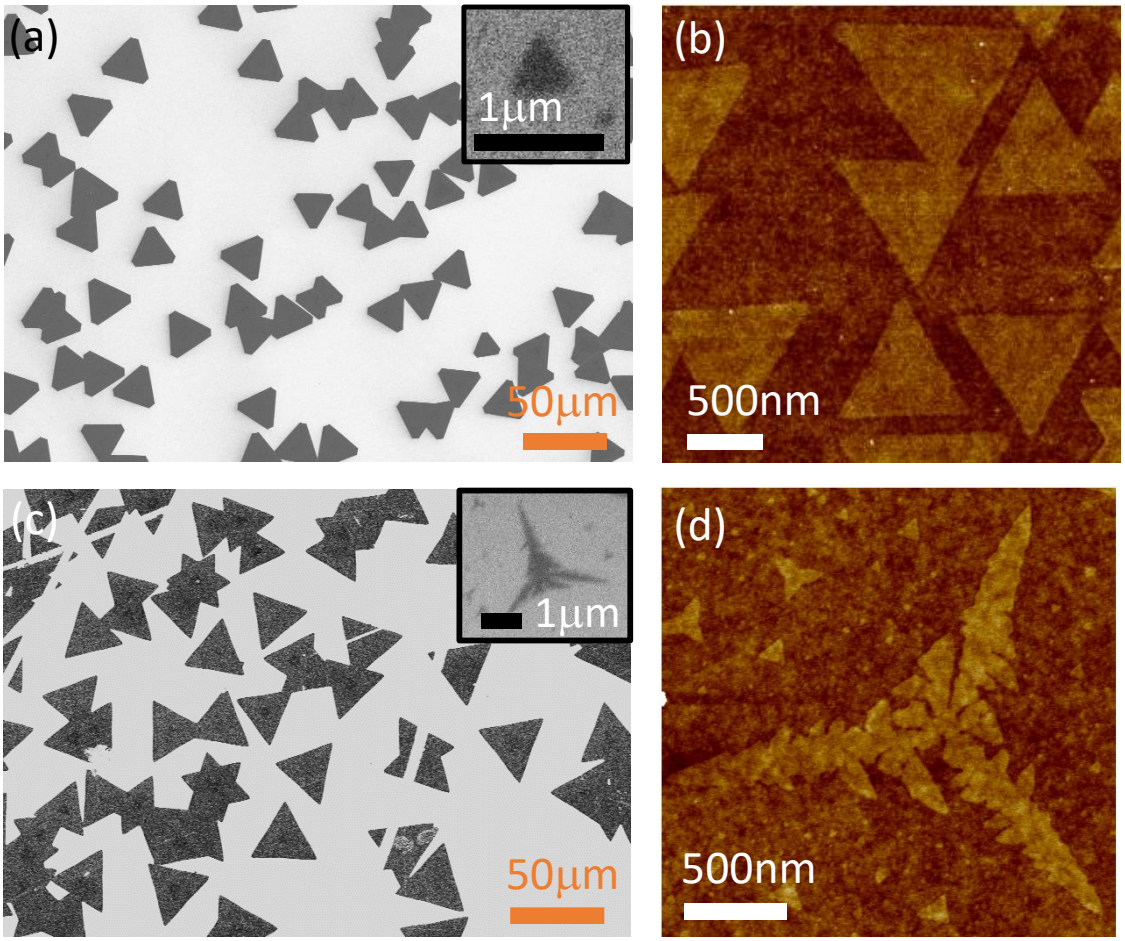

Figure 4.5: (a) SEM image of triangular MoS_2 domains grown under H_2. (inset) Zoomed out SEM and (b) AFM micrographs on a primary domain show formation of secondary domains of compact equilateral triangles in shape. (c) SEM image of MoS_2 domains grown under N_2. Primary domains are larger in size compared to that grown under H_2. (inset) Zoomed out SEM and (d) AFM micrographs show formation of dendritic secondary domains on a primary domain.

As H_2 carrier gas reduces the number of dangling bonds (thereby suppressing nucleation centers on the grown domains), a reduction in the number of secondary domains is evident [Figure 4.4(a2) and 4.4(e2)]. Moreover, in the process the surface diffusion is also enhanced, helping adatoms to find thermodynamically more stable compact triangular shape in H-MoS_2 [inset of Figure 4.5(a) and Figure 4.5(b)]. However, in case of N-MoS_2, due to the presence of more number of dangling bonds, adatoms require more energy to diffuse across the domain edges leading to dendritic shape of the secondary domains [inset of Figure 4.5(c) and Figure 4.5(d)]. Similar observation has also been made by Wu et al where more dangling bonds lead to dendrite formation in MoS_2 [80]. This is in line with our findings from XPS analyses that without the presence of a reducing environment, the MoS_2 formed will have intermediate oxides, and unsaturated Mo bonds which lead to presence of dangling bonds.

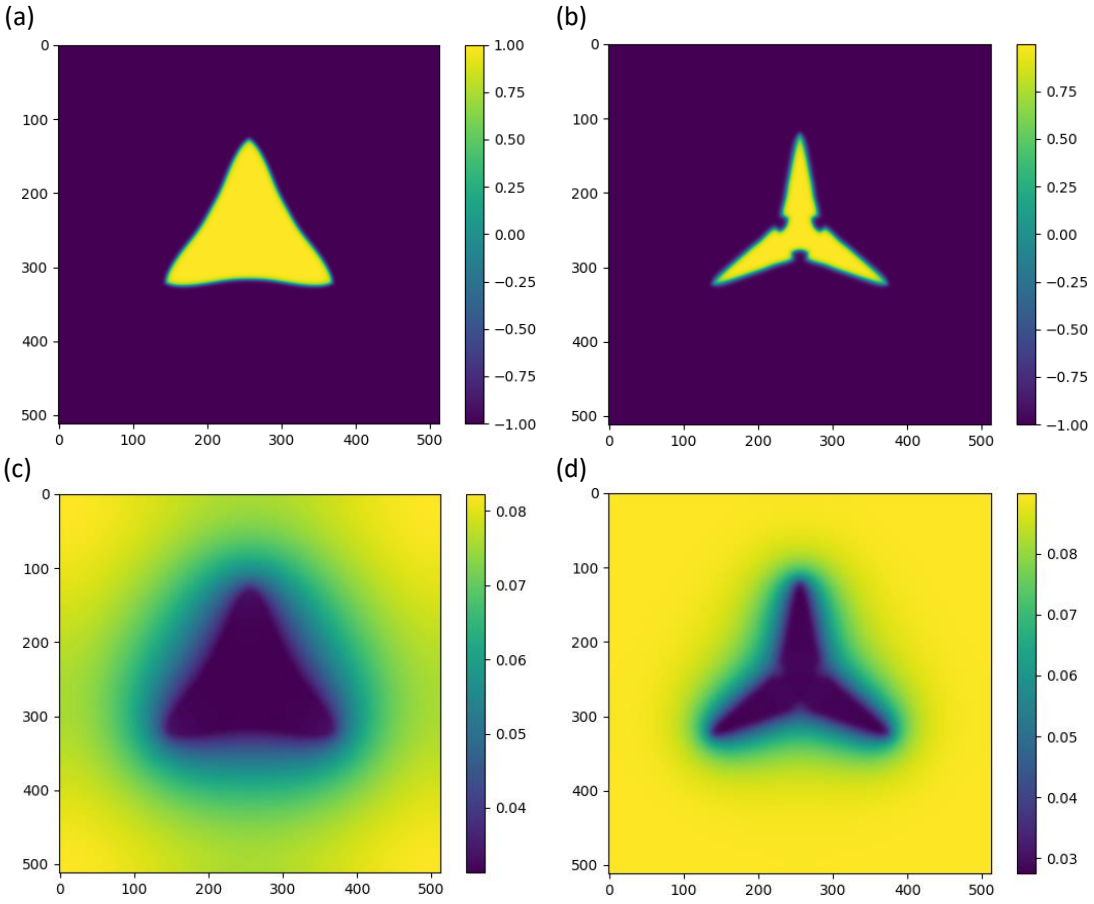

Figure 4.6 Effect of surface diffusion in determining the shape of secondary domains is verified using phase-field model. (a) Compact triangular secondary domains on H-MoS_2 matches well with the simulated patterns with enhanced surface diffusion. Similarly, (b) dendritic domains on N-MoS_2 agrees with patterns simulated with lower surface diffusion. Corresponding adatom concentrations are shown in (c) and (d), respectively.

Formation of different secondary domain morphologies due to suppressed adatom diffusion in N-MoS_2 is further supported by phase field simulations. The phase-field model is based on that of Roy *et al.* [82] and discussed in Appendix E. As shown in Figure 4.6(a) and 4(b), with the other growth parameters unaltered, adatom diffusion across the surface determines both the growth rate and the growth mechanism deciding the final shape of the grown domain. A faster diffusion in case of H-MoS_2 leads to a compact shape [Figure 4.6(a)], while slower diffusion in case of N-MoS_2 leads to branching out along the

symmetry-governed directions directing to dendritic domain formation [Figure 4.6(b)]. The results are consistent with previous observations [83–85]. This also confirms that compared with Ar and N_2, induction of H_2 as carrier gas directs APCVD growth towards more dangling bond free 2D regime.

4.8 CONCLUSION

In summary we have synthesized large area single crystal monolayer MoS_2 under various combinations of three different carrier gases: N_2, Ar and H_2. We observe that Introduction of H2 leads to a more uniform 2D growth with very little to no growth of secondary domains. XPS analyses show that when MoS_2 is grown under a reducing environment, compared to the ones grown under N_2 or Ar, the Mo(VI) oxidation state corresponding to MoO_3 from the CVD growth precursor is highly suppressed leading to a more pristine nature of MoS_2. This more efficient conversion of Mo(VI) to Mo(IV) also mean that there are negligible intermediate oxidation states and hence overall fewer dangling bonds which otherwise serve as sinks for nucleation of subsequent layers. This H_2 induced reduction of dangling bonds also lead to enhanced surface diffusion on the MoS_2 monolayer which results in the secondary domains resorting to their thermodynamically stable triangular shape as opposed to dendritic shape in case of N-MoS_2.

Chapter 5: Two-Step Growth of Uniform Monolayer MoS_2 Nanosheets by Metal-Organic Chemical Vapor Deposition

5.1 INTRODUCTION

In this work, we report large area MOCVD growth of MoS_2 film that transforms into homogeneous distribution of single crystal triangular domains of monolayer thickness by its controlled sulfurization. Several characterization techniques *e.g.*, Raman and photoluminescence (PL) spectroscopies, optical microscopy, scanning electron microscopy (SEM), atomic force microscopy (AFM) and X-ray photoelectron spectroscopy (XPS) are used to determine the crystalline quality, surface morphology, stoichiometry, and contamination level upon sulfurization of the grown films. Following sulfurization, MOCVD grown MoS_2 monolayer domains also show electrical properties that are comparable to those grown by the APCVD method.

5.2 MOCVD GROWTH OF MoS_2:

5.2.1 Growth Method:

Large area MoS_2 was synthesized in an MOCVD growth system under low-pressure conditions [Figure 2.6]. The precursors used for MoS_2 growth are molybdenum hexacarbonyl, $Mo(CO)_6$ (Sigma Aldrich, CAS number 13939-06-05, 99.9%), and diethyl sulfide, $(C_2H_5)_2S$ (Sigma Aldrich, CAS number 352-93-2, 98%). The target substrate used in this work was 285 nm SiO_2 grown on highly doped double side polished *p*-type Si. At the start of the growth process, the target substrate (measuring 10 cm × 1.7 cm) was placed

---

Much of the discussions presented in this Chapter have been adapted from the following reference: Ref [2]: Chowdhury, S., Roy, A., Liu, C., Alam, MH., Ghosh, R., Chou, H., Akinwande, D., Banerjee, SK., "*Two-Step Growth of Uniform Monolayer MoS_2 Nanosheets by Metal–Organic Chemical Vapor Deposition*" ACS Omega **6**, 15, 10343–10351 (2021), reprinted with permission from [ACS Omega 2021, 6, 15, 10343–10351]. Copyright [2021] American Chemical Society. Available at: https://doi.org/10.1021/acsomega.1c00727. The dissertator, S. Chowdhury, conceived and designed the experiments, conducted growths, carried out material characterization and analysis and largely wrote the manuscript with contributions from all the authors.

approximately 10 cm into the furnace and the system was pumped down to base pressure (~ 1.5 mTorr) following which three subsequent purge cycles using ultra high purity Ar at 100 sccm were performed. Afterwards, Ar flow was cut off and H_2 flow was introduced at 5 sccm as the carrier gas for the rest of the growth. Background pressure of the system was held at 5 mTorr. $Mo(CO)_6$ and $(C_2H_5)_2S$ precursors were kept in bubblers in atmospheric pressures at 45 °C and at room temperature, respectively, and the flow rates were controlled *via* needle valves. The growth was conducted at 850 °C for a duration of 1 min after which the precursor gas flow was cut off and the furnace was allowed to cool down, with only the carrier gas flowing.

5.2.2 As-grown film characterization:

Raman spectroscopic measurements in Fig. 5.1 show two distinct peaks at ~386 cm^{-1} and ~406 cm^{-1} which coincides with the Mo-S phonon modes E^1_{2g} (in-plane) and A_{1g} (out-of-plane) peaks of MoS_2, respectively, as found in literature [51].

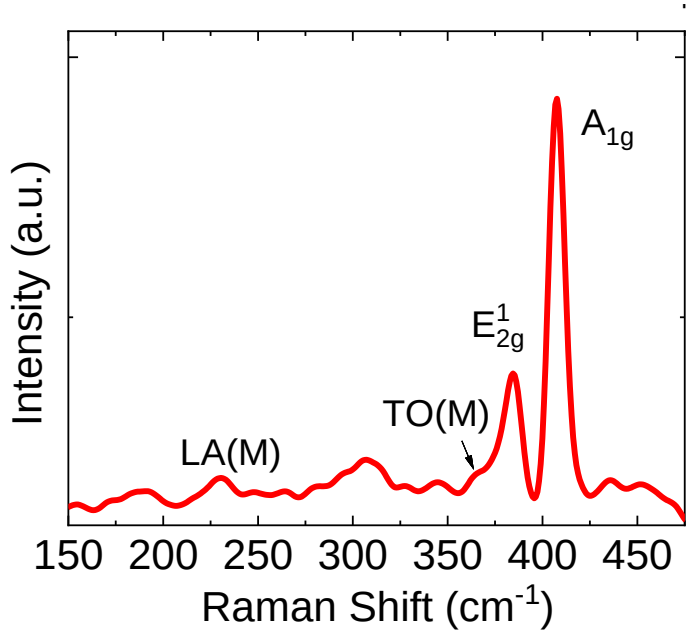

Figure 5.1: Raman spectrum of the as-grown MOCVD MoS_2 films.

However, the asymmetry in the E^1_{2g} peak suggests the presence of defect activated peaks and/or peaks due to intermediate oxides that are formed during growth [86]. In CVD grown MoS_2, sulfur vacancies are one of the most common defects [87,88] which results in unsaturated chemical bonds formation between Mo atoms. These bonds can interact with neighboring S atoms and disturb the crystal symmetry which activates phonon modes otherwise unavailable in pristine MoS_2. The peak at ~229 cm^{-1}, referred to as LA(M), possibly originates from the presence of a local maximum in the vibrational density of states located at the energy corresponding to the longitudinal acoustic (LA) branch at the edge of the Brillouin zone [89]. Other prominent defect induced peaks that arise at ~359 cm^{-1}, ~180 cm^{-1} and ~187 cm^{-1} are assigned to the TO(M), ZA(M) and TA(K) modes respectively [90].

5.2.3 Post-Growth Sulfurization:

The vacancies and disorders can be "repaired" to a great extent by annealing post growth in a S-rich environment. In another single zone Lindberg/Blue M CVD furnace the MOCVD grown MoS_2 sample was loaded in the center with sulfur powder (Sigma Aldrich, CAS number 7704-34-9, 99.98%) positioned upstream relative to the MoS_2 sample and heated separately using a heating coil [91]. The as grown samples were sulfurized at different temperatures for different durations. Sulfurization procedure was initiated by raising the temperature of the MoS_2 sample to the target temperature. Sulfur was heated to 150 °C and a carrier gas (N_2) was flown in at 10 sccm. After holding the MoS_2 film at the target temperature for desired duration, the furnace heating and the heating coil for sulfur were cut-off and subsequently allowed to cool down without any feedback control.

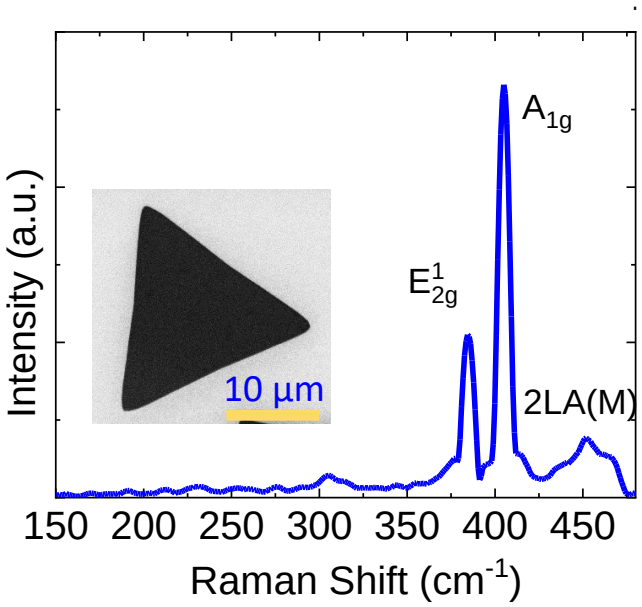

Figure 5.2: Raman spectrum of the MoS_2 films after sulfurization at 850 °C for 30 min. Inset shows SEM image of a triangular MoS_2 domain following sulfurization.

Upon sulfurization at 850 °C under atmospheric pressure for 30 min, the as-grown film transforms into isolated monolayer triangular domains as seen in inset of Fig. 5.2. During the sulfurization process at high temperature, the carbon impurities from the organic precursors and oxide based intermediate compounds can be desorbed from the MOCVD-grown film. The incoming S-adatoms can react with these unpassivated Mo sites, as well as with the desorbed intermediate compounds in gas phase leading to MoS_2 triangular domains. Raman spectrum of MOCVD grown MoS_2 film after sulfurization is shown in Fig. 5.2. Most of the defect induced peaks present in the as-grown sample disappear following sulfurization and the first order peak intensities and linewidths are greatly improved [Figure 5.3], indicating reduction in defect density and improvement in crystalline quality. The full width at half maxima of the A_{1g} Raman peak improves from 5.17 cm^{-1} in case of as grown film to 4.23 cm^{-1} after annealing in sulfur environment which is much closer to the value for exfoliated flake (3.51 cm^{-1}), as seen in Fig. 5.3 (c). An additional peak at ~450 cm^{-1} now appears after sulfurization due to fewer defects and is

attributed to an overlap of two peaks: the second order of the LA mode at the M-point called the 2LA(M) peak and a first order optical phonon peak A_{2u} [90,92].

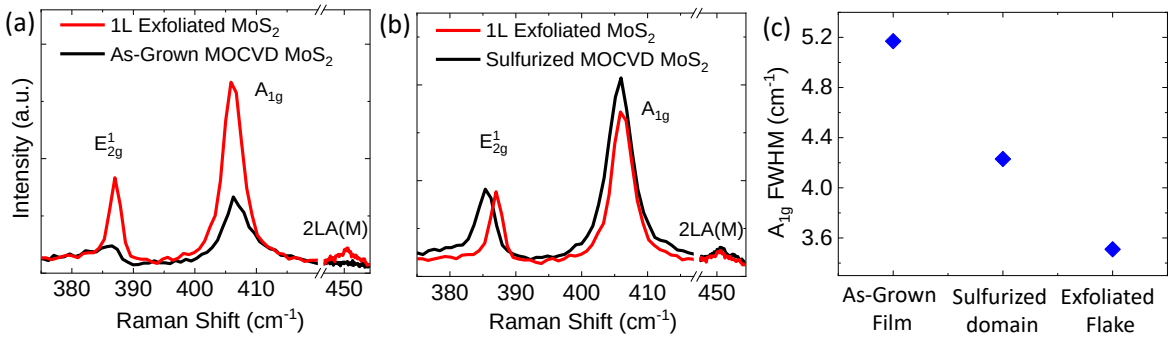

Figure 5.3: Comparison of Raman spectra between monolayer exfoliated flake and MOCVD grown MoS_2 (a) as-grown film, and (b) following sulfurization at 850 °C for 30 min. (c) Improvement in A_{1g} Raman peak full width at half maxima upon sulfurization.

5.3 COMPARISON BETWEEN APCVD AND 2-STEP MOCVD GROWN FILM

To compare our two-step growth process with that of other widely used methods, we have conducted growth of MoS_2 *via* solid-precursor-based (MoO_3 and S powder) APCVD method. Details of the growth process can be found in section 2.2.1.1.

Figure 5.4 (a) shows an optical micrograph of APCVD MoS_2 grown on Si/SiO_2 substrate. Compact MoS_2 domains as large as 40-50 μm are primarily triangular or hexagonal in shape [as shown in the optical and SEM images in Fig. 5.4 (b) and 5.4 (c), respectively]. Figures 5.4 (d) and 5.4 (e) show Raman and PL spectroscopies of a typical monolayer domain grown by APCVD. The Raman peak difference of ~19 cm^{-1} and a sharp distinct PL peak at 1.86 eV [FWHM is ~0.06 eV] are consistent with those of monolayer MoS_2 [49]. While this method produces MoS_2 with quality comparable to exfoliated flakes, a large portion of the substrate is rendered unusable due to very thick deposits of MoS_2, MoO_3 and intermediate compounds.

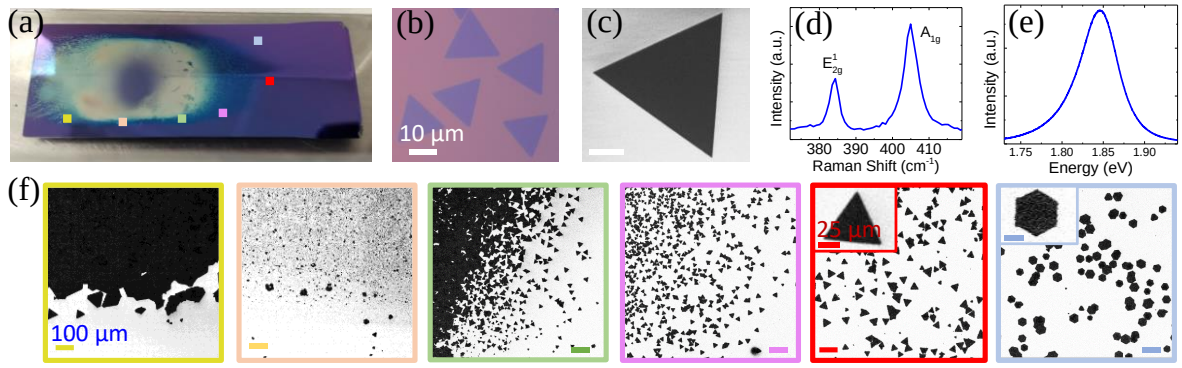

Figure 5.4: (a) Optical image of Si/SiO_2 substrate after APCVD growth of MoS_2. (b) Optical and (c) SEM images of triangular MoS_2 domains. Scale bars are 10 µm. Corresponding Raman and PL spectra are shown in (d) and (e), respectively. (f) Variation of MoS_2 domain size, shape, nucleation density and thickness in different locations of the sample [color coded accordingly in (a)]. Scale bars for all the images are 100 µm. Insets show magnified images (scale bars are 25 µm) of one of the domains to signify the domain shape.

The experimental setup used for APCVD growth of MoS_2 involves placing the substrate face-down on top of a crucible containing MoO_3 powder. Since MoO_3 is a low vapor pressure solid it needs to be placed at the center of the heating zone at 850 °C and hence the metal precursor flux cannot be precisely controlled. This setup causes majority of the MoO_3 powder to evaporate and/or react with S powder either partially or completely depending on local Mo/S ratios. In addition to MoS_2 with varying thicknesses, the unreacted and partially reacted MoO_3 also deposit on the central region of the substrate and monolayer MoS_2 is formed only in the faint blue region along its periphery [Figure 5.4 (a)]. Figure 5.4 (f) shows SEM images from 6 different points marked on different locations in Fig. 5.4 (a) (color coded) showing the variation in domain shapes, sizes, distribution, and thicknesses. Domain sizes range from 5 µm to 100 µm, from monolayer to bulk in thickness, and the nucleation density decreases as we move downstream. Sharp gradient of concentration of domains across the sample is clearly seen in Fig. 5.4 (f) where the domain density decreases as we move further away from the MoO_3 source, indicating a non-

homogeneous coverage. These differences in local Mo/S ratios also give rise to different morphologies, triangles and hexagons, as shown in the inset of Fig. 5.4 (f).

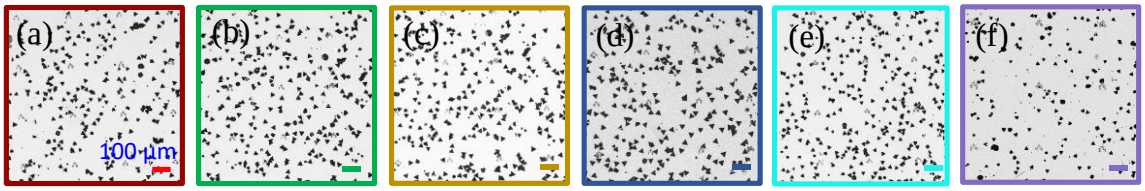

Figure 5.5: MOCVD Growth of MoS_2: (a-f) Uniformity of MoS_2 domain size, shape, nucleation density and thickness in different locations of the MOCVD grown sample. Scale bars are 100 µm.

Figure 5.5 shows MoS_2 grown on Si/SiO_2 substrate *via* two-step MOCVD method. Unlike solid-precursor-based APCVD growth, MOCVD uses gas phase precursors, which results in more uniform film coverage across the substrate. Following the post growth sulfurization process at 850 °C for 30 min mostly isolated triangular MoS_2 domains of ~ 30 µm in size are formed. SEM images taken from 6 different spots of the MOCVD film following sulfurization are shown in Fig. 5.5 and shows much more uniform coverage of domains across the entire substrate. There are a few occurrences of the domains merging to form different types of grain boundaries [as shown in Fig. 5.6], as also observed in MoS_2 grown by APCVD method [74,93,94].

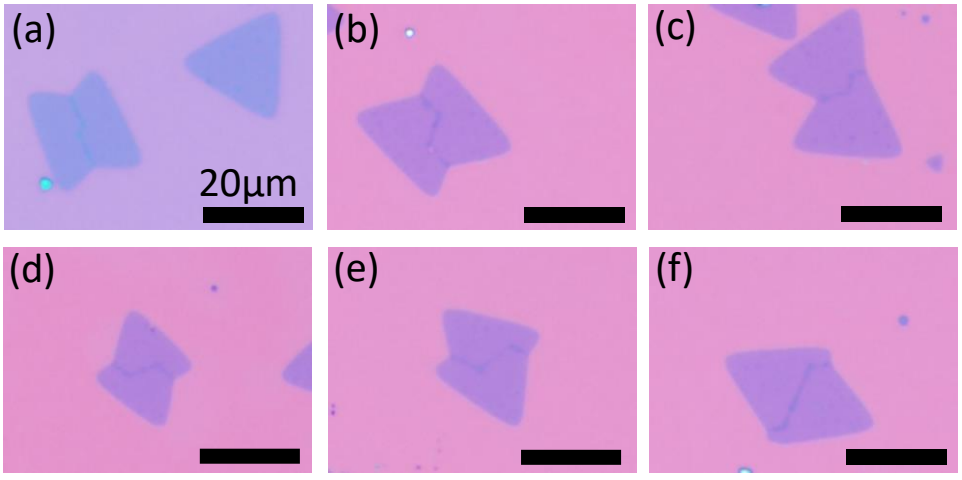

Figure 5.6: Different grain boundaries in sulfurized MoS_2 domains.

Raman spectra from different spots across different MoS_2 domains are shown in Fig. 5.7 which does not show any significant variation. These observations confirm that, unlike APCVD, this method produces triangular monolayer domains distributed homogeneously across the entire substrate.

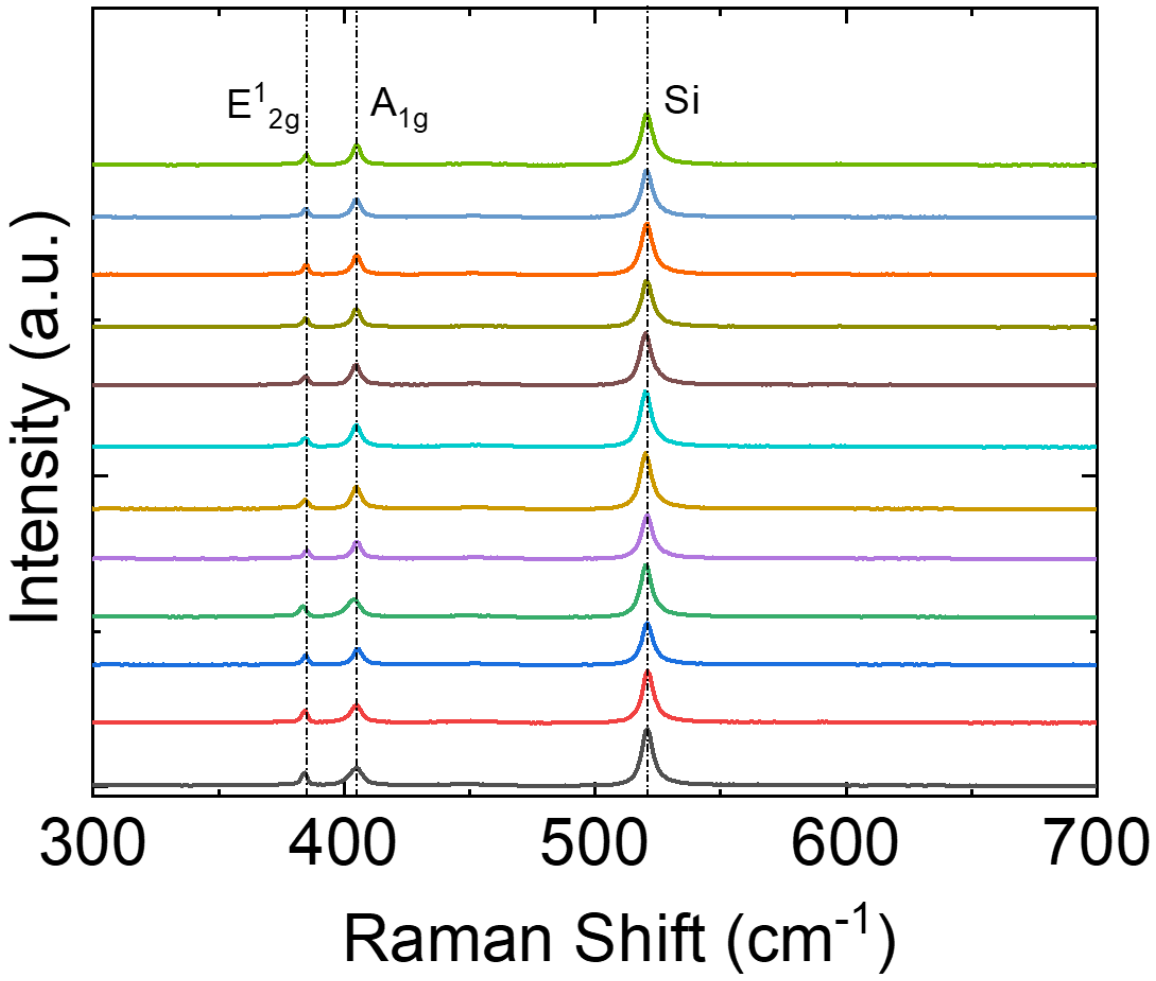

Figure 5.7: Raman spectra at different points across the substrate.

5.4 EFFECT OF ANNEALING CONDITIONS

To study the effect of annealing conditions, several identical MoS_2 samples grown by MOCVD were annealed at different temperatures/durations in a S-rich environment. Figure 5.8 (a) shows the comparison among normalized Raman spectra of the grown film sulfurized for 30 min at different temperatures: 550 °C, 650 °C, 750 °C and 850 °C. With increase in the sulfurization temperature, the distortion in E^1_{2g} peak which usually arises from the presence of oxide based intermediate compounds and defects in the MoS_2 film gradually transforms into a sharp distinct peak, as expected for pristine single crystal MoS_2. This improvement in crystalline quality is further confirmed from the enhanced peak intensities and reduced linewidths of the first order Raman peaks. Figure 5.8 (b) shows variation in peak intensities and the full width at half maximum (FWHM) with increased sulfurization temperature for the A_{1g} Raman peak.

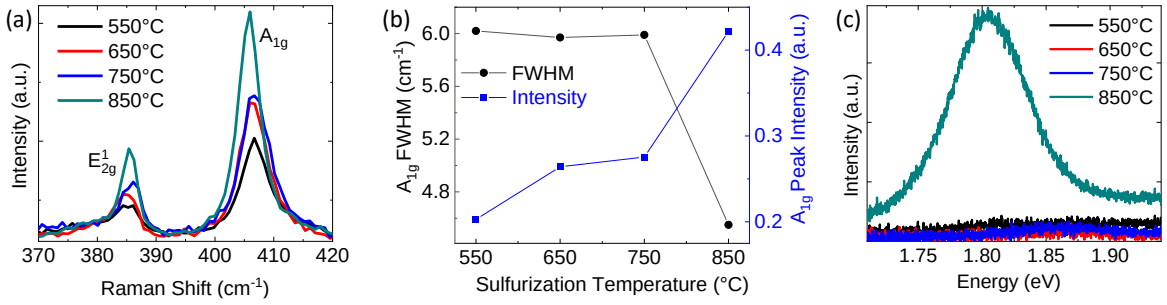

Figure 5.8: Comparison of Raman and PL spectra of the as-grown MOCVD film following sulfurization at different temperatures and durations. All Raman data have been normalized with respect to Si. (a) Comparison of Raman spectra for the samples sulfurized at different temperatures: 550 °C, 650 °C, 750 °C and 850 °C. Sulfurization duration was kept 30 min for all the samples. (b) Variation of A1g FWHM and normalized A1g peak intensity with respect to sulfurization temperature. (c) PL spectra for different samples sulfurized at different temperatures.

As the sulfurization temperature increases, linewidth of the A_{1g} peak decreases from 6.02 cm^{-1} to 4.55 cm^{-1} which indicates gradual reduction in structural disorder [79] [Figure

5.8 (b)]. The improvement in crystalline quality is also evident from the enhanced PL peak intensities [95] and narrow PL peak width for the sample sulfurized at 850 °C for 30 min, signifying the direct bandgap for monolayer MoS_2 at 1.8 eV as shown in Fig. 5.8 (c).

A similar trend in Raman E^1_{2g} linewidth with sulfurization temperature is shown in Fig. 5.9.

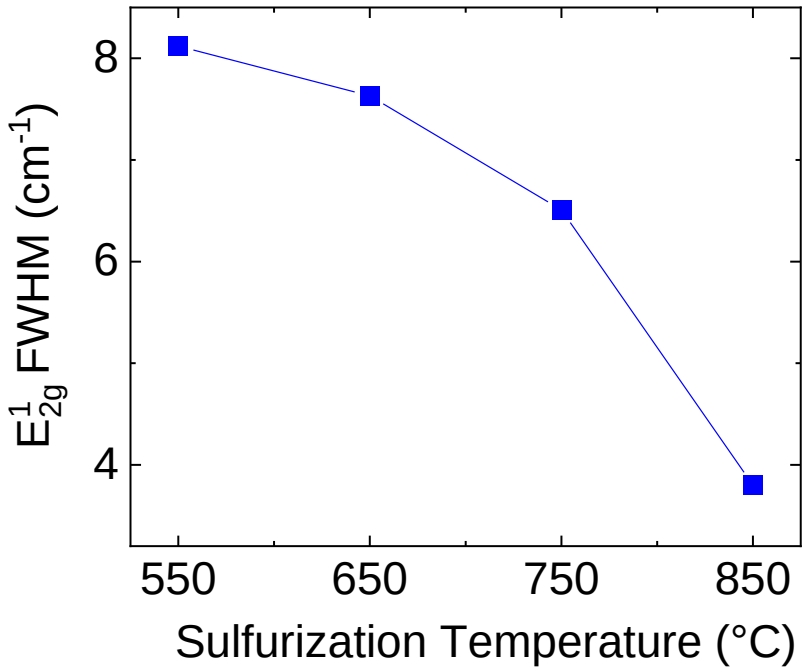

Figure 5.9: Variation of E^1_{2g} Raman peak for different sulfurization temperatures.

Transformation of continuous MOCVD-grown MoS_2 film into monolayer domains upon sulfurization at various temperatures is shown in Fig. 5.10. No significant improvement is observed optically as the film is sulfurized at 550 °C and 650 °C as seen in Fig. 5.10 (a-b). However, for a sulfurization temperature of 750 °C, some indefinite patches of MoS_2 appear [Figure 5.10 (c)]. At 850 °C, sharp triangular domains of 1L MoS_2 are formed. [Figure 5.10 (d)].

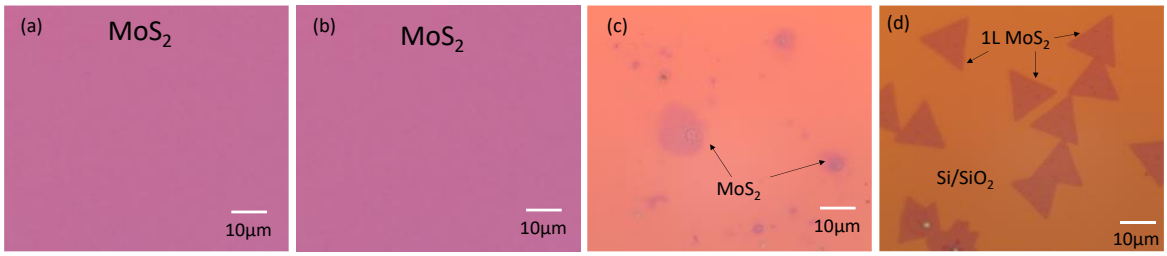

Figure 5.10: Optical microscopy images following sulfurization at (a) 550 °C (b) 650 °C (c) 750 °C (d) 850 °C for a duration of 30 min.

Further increase in the sulfurization temperature, however, produces non-compact thicker MoS_2. Figure 5.11 shows the Raman spectrum from MOCVD-grown MoS_2 film following sulfurization at 950 ˚C for 30 min. Sulfurization at higher temperature leads to patches of thicker MoS_2 distributed sparsely across the substrate (inset). A peak separation between the E^1_{2g} and A_{1g} is observed to be ~ 26.4 cm^{-1} which corresponds to bulk MoS_2 [49].

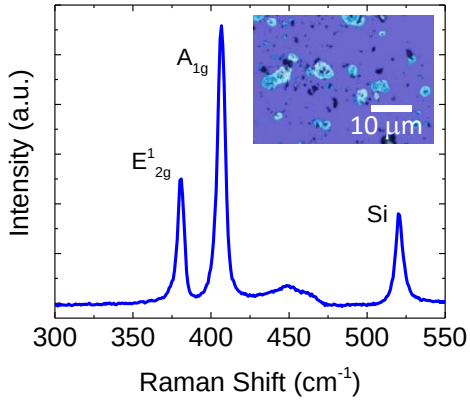

Figure 5.11: Sulfurization of As-Grown MoS_2 Film at 950 ˚C for 30 min.

Figure 5.12 (a) show the Raman spectra of the as-grown MOCVD films compared to samples that were sulfurized at 850 °C for 5 min and 30 min. The A_{1g} peak intensity and FWHM also improve accordingly, as shown in Fig. 5.12 (b). Corresponding PL spectra are compared in Fig. 5.12 (c).

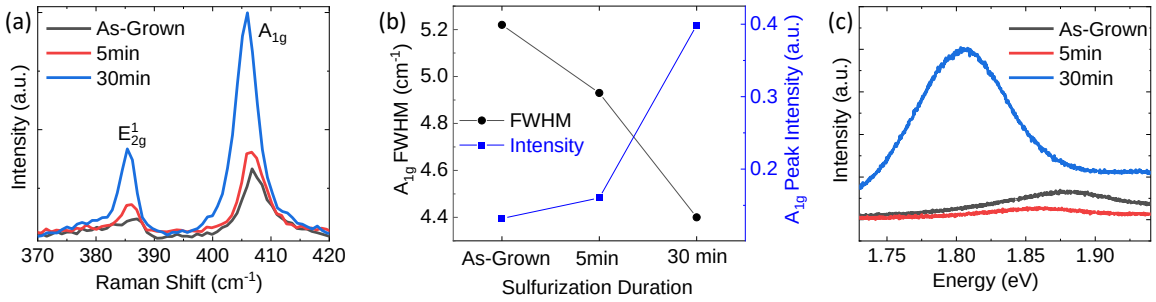

Figure 5.12: (a) Comparison of the MoS_2 Raman peaks as a function of sulfurization duration: as grown, 5 min and 30 min. Sulfurization temperature was kept at 850 °C for all the samples. (b) Variation of A_{1g} FWHM and normalized peak intensity with respect to sulfurization duration. Corresponding variation in PL spectra are shown in (c).

Although optically no significant difference is observed for the duration of 5 min sulfurization, monolayer triangular MoS_2 domains appear to be distributed uniformly across the entire substrate following sulfurization at 850 °C for 30 min (Figure 5.13).

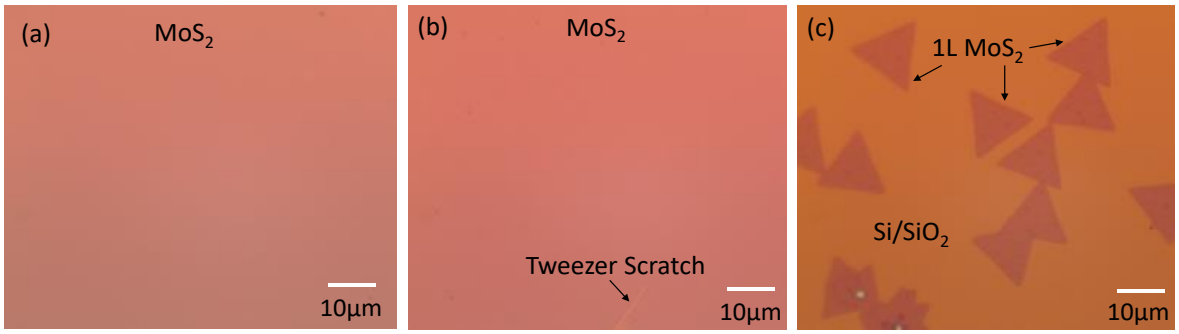

Figure 5.13: Effect of sulfurization duration: (a) As-grown continuous MoS_2 film grown by MOCVD method. (b) No significant change is observed for the film sulfurized at 850 °C for 5 min. (c) Sulfurization for 30 min produces monolayer isolated MoS_2 triangular domains.

Figure 5.14 shows the gradual improvements in the FWHM corresponding to the PL spectra shown Fig. 5.12 (c).

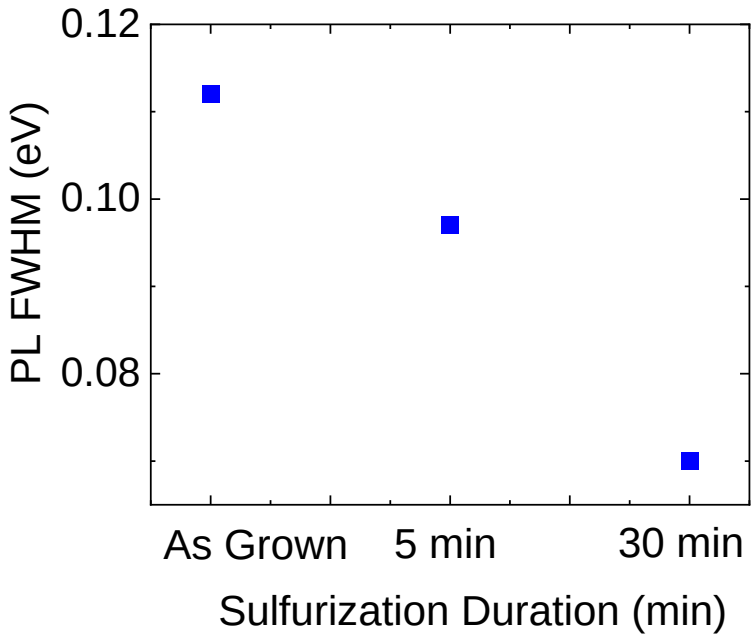

Figure 5.14: Variation of PL peak FWHM for different sulfurization durations.

5.5 CONTAMINATION IN THE MOCVD FILM: RAMAN ANALYSES

Using diethyl sulfide as the chalcogen precursor in MOCVD growth leaves significant carbon residues in the grown film [40]. The Raman spectrum from the as grown film in Fig. 5.15 (black line) shows presence of peaks at defect related D-band at ~ 1347 cm^{-1} and graphite related G band at ~1597 cm^{-1} [96], confirming presence of carbonaceous compounds. Similar observation has also been made by Choudhury *et al.* [97] and also by Zhang *et al.* [98], where the presence of carbon G peak is observed for the films grown at different temperatures. These peaks disappear completely following sulfurization [Figure 5.15, blue line], indicating significant reduction in carbon contamination.

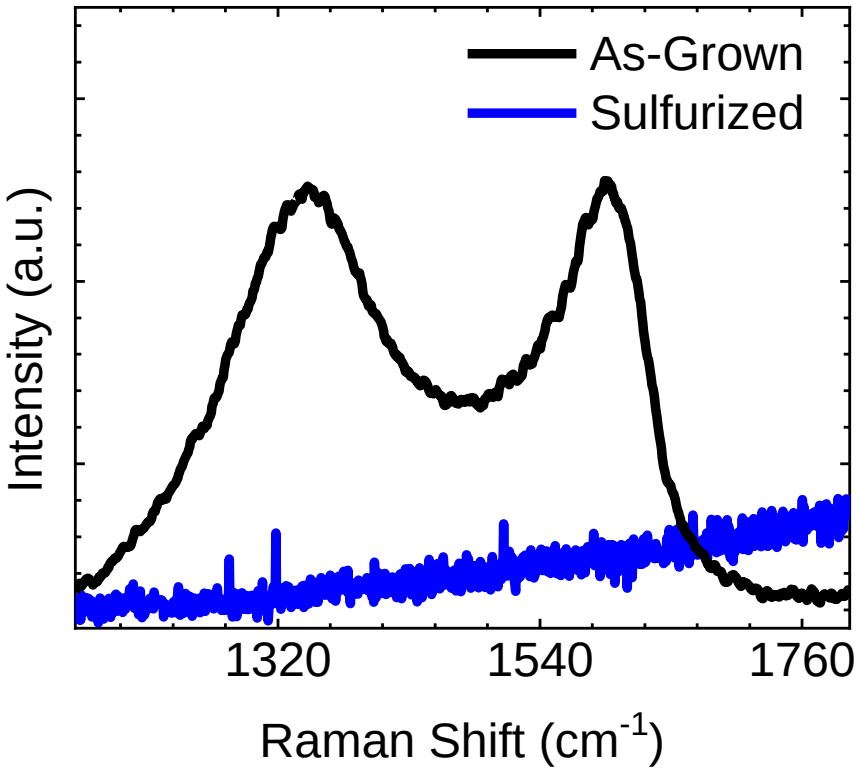

Figure 5.15: Variation of PL peak FWHM for different sulfurization durations.

5.6 CONTAMINATION IN THE MOCVD FILM: XPS ANALYSES

To further check the film quality and to confirm the presence of oxide and carbon contamination, elemental analysis and chemical stoichiometry quantification were investigated using XPS. Figures 5.16 (a) and (b) show the XPS survey scans of the MOCVD-grown MoS_2 films before and after sulfurization process, respectively. From XPS survey spectra all the major peaks are identified and labeled as Mo and S, and Si from the substrate. Presence of C and O in the survey spectrum from the as-grown film is evident. In addition to the adsorbed atmospheric molecular contamination from moving/storing the samples *ex situ* to the XPS system [99,100] and underlying Si/SiO_2 substrates contributing to the oxygen peak, metal organic precursors contribute significantly to the carbon contamination of the grown film.

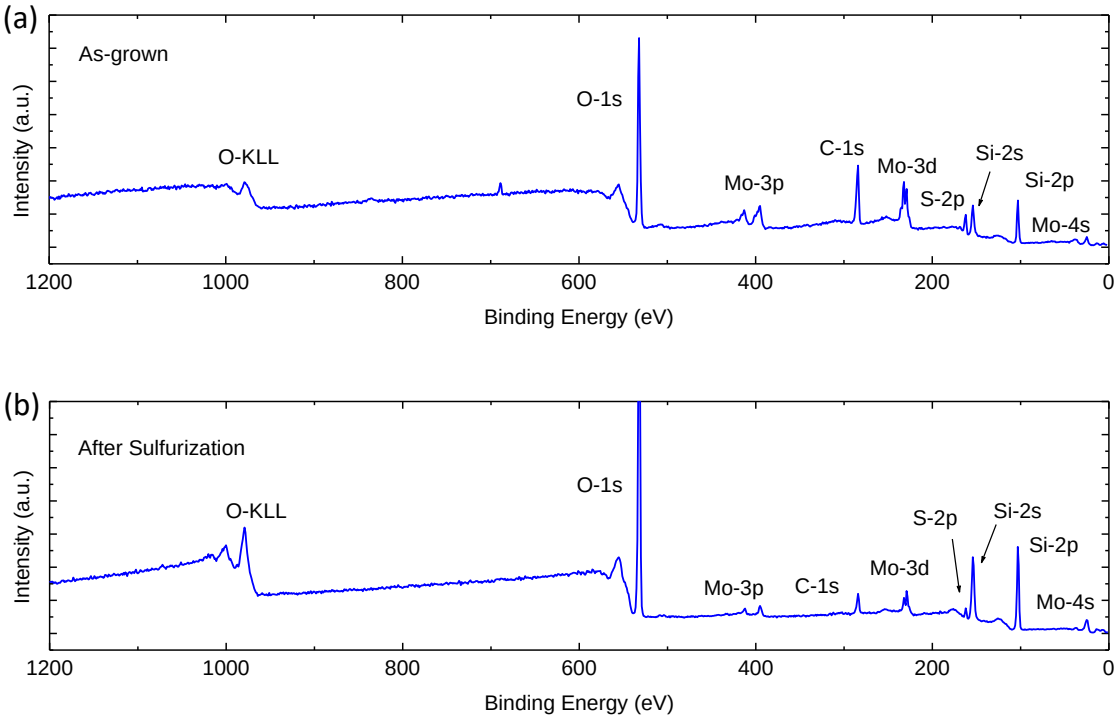

Figure 5.16: XPS survey spectra from MoS_2 film grown on Si/SiO_2 substrates by MOCVD process (a) before and (b) after sulfurization process.

Here, the C-C component at 284.8 eV belonging to the C-1*s* spectrum of adventitious carbon contamination is used as a charge referencing for all the XPS spectra. This method of using aliphatic carbon peak as charge correction reference may sometimes be unreliable since the nature and thickness of the film may vary. However, it can be a convenient method of referencing when relative peak shifts and not absolute peak positions are considered, as is the case here.

Figure 5.17 shows high resolution spectra for Mo-3*d*, S-2*p* and C-1*s* peaks from the as-grown MOCVD film [Figure 5.17 (a)] and from samples sulfurized under the optimized conditions [Figure 5.17 (b)]. The Mo-3*d* spectra shows clear presence of molybdenum oxide at 236.5 eV on the as-grown film that almost vanishes after sulfurization indicating conversion of remaining oxides to MoS_2 [101].

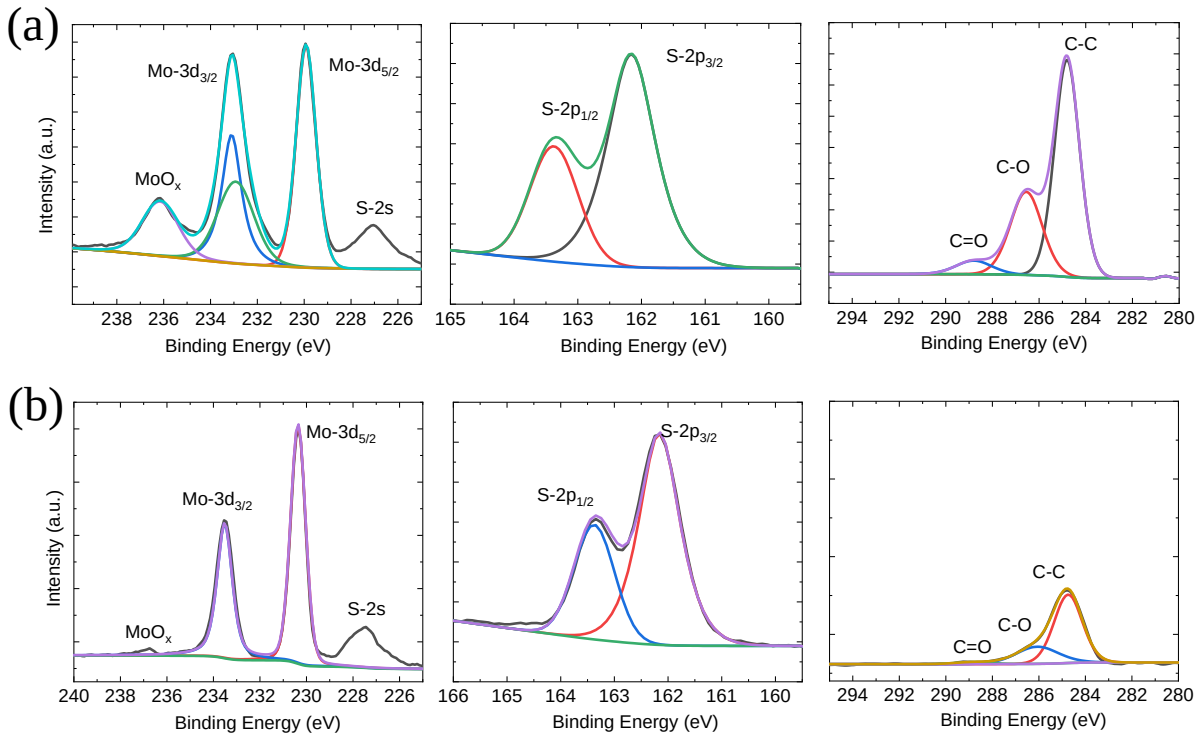

Figure 5.17: High resolution XPS spectra from MoS_2 films compared before and after sulfurization: Mo-3*d*, S-2*p* and C-1*s* peaks from (a) the as-grown and (b) after sulfurization at 850 °C for 30 min.

In addition to this, MOCVD film quality suffers greatly due to significant carbon contamination arising from organic precursors such as diethyl sulfide, as mentioned previously [Figure 5.15]. C-1*s* spectra from the as grown film [Figure 5.17 (a)] can be resolved into the following components: C-C at 284.8 eV, C-O at 286.6 eV and C=O at 288.8 eV. Upon sulfurization at 850 °C for 30 min, most of the carbon contamination is reduced as seen from a sharp decline in the peak intensity of C-1*s* spectra in Figure 5.17 (b). Some carbon however, is still present as is the case with all materials that has been exposed to the ambient. The stoichiometry as calculated from the integrated peak areas of Mo and S is found to be Mo:S = 1:1.6 for the as-grown film. This means that about 20% of the sulfur sites are vacancies. If we assume a uniform distribution of the sulfur vacancies, one in every five S-sites have S missing. Considering the distance between adjacent S-sites to be 0.316 nm, the average distance of defects, L_D, is found to be ~1.58 nm. Upon sulfurization, the stoichiometry improves to almost near ideal value of 1:1.97 which corresponds to an average inter-defect distance to be ~21.06 nm. This is a ~13-fold increase in the average inter-defect distance and it clearly shows the significant improvement in the film quality upon sulfurization. Figure 5.18 shows the improvement in stoichiometry of MoS_2 with increasing sulfurization temperatures.

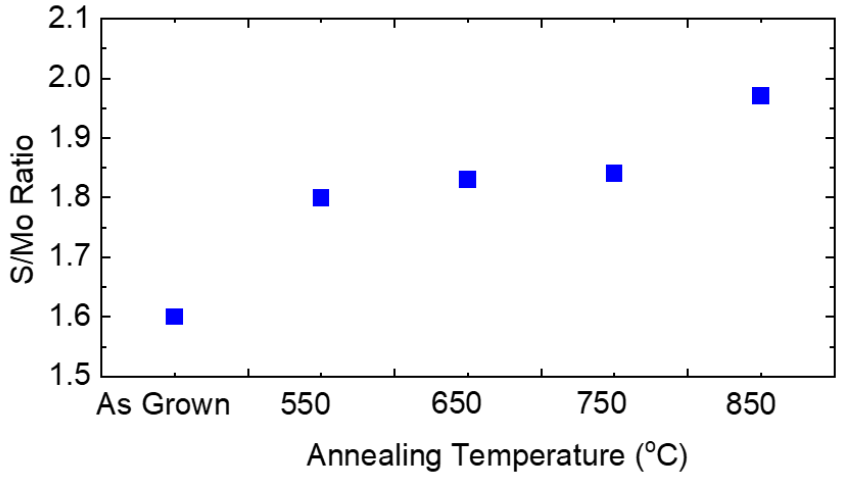

Figure 5.18: Improvement in stoichiometry of MoS_2 with increasing sulfurization temperatures.

To demonstrate the gradual improvement in the film quality with increasing sulfurization temperature/durations, Fig. 5.19 shows the high resolution XPS analyses for the samples sulfurized at different conditions. Annealing for 30 min at different temperatures in S-environment, and for different durations at 850 °C are shown in Fig. 5.19 (a,b) and 5.19 (c,d), respectively. The ratio of MoO_3 to MoS_2 as well as the carbon peak intensity gradually decreases with increasing sulfurization temperature [Figure 5.19 (b)] and duration [Figure 5.19 (d)] signifying a substantial reduction in defects and oxide/carbon contaminations.

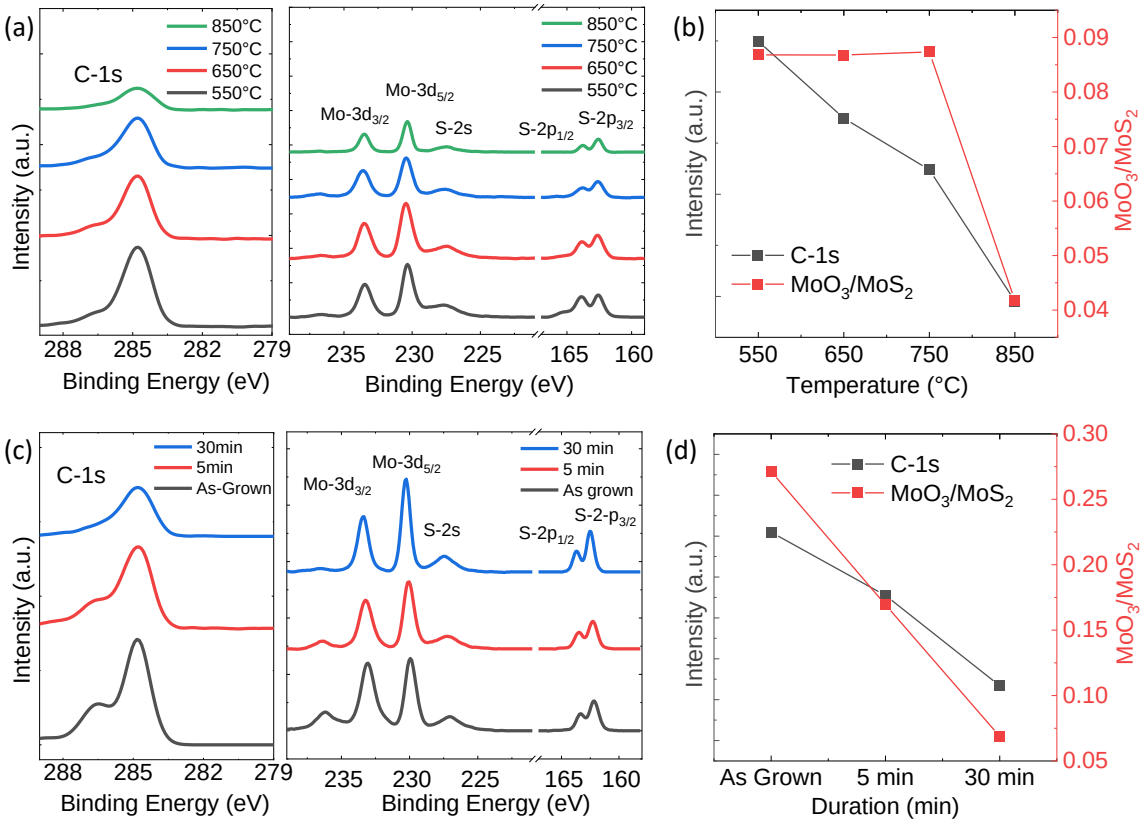

Figure 5.19: (a-b) Comparison of XPS spectra of MoS_2 films sulfurized at different temperature: (a) High resolution C-1*s*, Mo-3*d* and S-2*p* peaks and (b) corresponding variation of C-1*s* peak intensities and normalized MoO_3/MoS_2 peak ratios. (c-d) Comparison of XPS spectra of MoS_2 sulfurized for different duration: (c) High resolution C-1*s*, Mo-3*d* and S-2*p* peaks and (d) corresponding variation of C-1*s* peak intensities and normalized MoO_3/MoS_2 peak ratios.

5.7 ELECTRICAL PROPERTIES

To compare the electrical quality of the film before and after sulfurization, back-gated FETs were fabricated on as-grown and sulfurized MoS_2. Back gated FETs fabricated on as-grown film shows no apparent gate modulation as evident from the near-constant drain and source current for a -60 V to +60 V back-gate voltage change, shown in Fig. 5.20 (a). The gate leakage current (I_{BG}) is at least four orders of magnitude lower than the drain/source current and the drain current (I_D) is nearly equal to the source current (I_S). The output characteristics reach a drain current of 200 nA/μm at a drain voltage of 4 V, again with no gate effect as seen from the overlapping currents for varying gate voltages (V_{BG}) in the range of 20 V to 60 V with an increment of 10 V. The absence of gate modulation has also been observed in other MOCVD-grown TMDs [102] and may be attributed to the predominance of localized charge-carrier states arising from the defects and grain boundaries in the grown film [24].

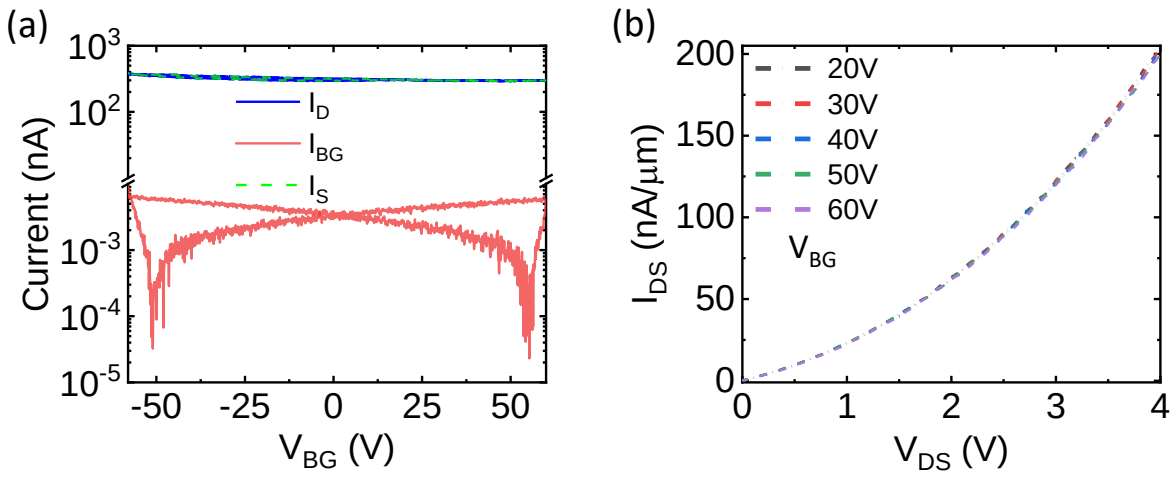

Figure 5.20: (a) Transfer and (b) output characteristics for as-grown MOCVD MoS_2-based transistor with a channel length 500 nm.

For the sulfurized film, uniform monolayer MoS_2 domains on Si/SiO_2 substrates were identified using a combination of optical contrast, Raman spectroscopy, and AFM.

Device active regions and source/drain metal electrodes were defined with electron beam lithography. A stack of Ni/Au (20 nm/30 nm) was deposited as source/drain metal electrodes using *e*-beam evaporator. All electrical DC measurements were performed on a Cascade Microtech Summit 11000B-AP probe station using an Agilent 4156C parameter analyzer in ambient at room temperature under dark. The sulfurized film was transferred *via* a poly (methyl methacrylate) (PMMA) based wet transfer method using NaOH as substrate etchant, onto the target Si/SiO_2 substrate with alignment mark. Figure 5.21 (a) shows PL spectra of an MoS_2 domain before and after transfer. Shift in the PL peak position upon transfer indicates relaxation of strain that develops during the high temperature growth and anneal cycles [74]. Suitable MoS_2 domains were identified using a combination of optical contrast, Raman spectroscopy, and AFM images. Next, drain/source metal contacts were patterned using *e*-beam lithography and subsequently contact metals (Ni/Au 20nm/30nm) were deposited using *e*-beam evaporation followed by lift-off. An optical image of the final device structure used is shown in the inset of Figure 5.21 (b). Electrical measurements were performed under ambient at room temperature without any illumination. Figure 5.21 (b) shows the I_{DS}-V_{GS} transfer characteristics of a SiO_2/Si back-gated MoS_2 transistor with 285 nm thick SiO_2 being the back-gate dielectric.

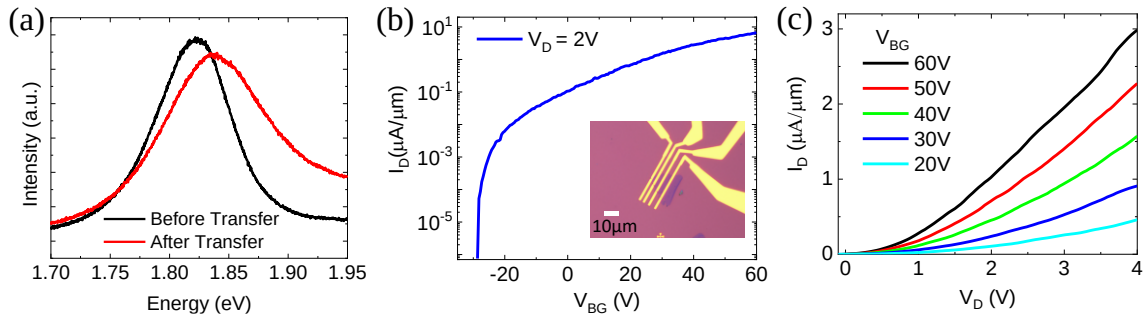

Figure 5.21: (a) Transfer and (b) output characteristics for as-grown MOCVD MoS_2-based transistor with a channel length 500 nm.

The back-gate voltage (V_{BG}) is swept from -30 V to 60 V at a drain voltage of 2 V. The device exhibits a threshold voltage (V_{th}) of around -10 V. The ON/OFF ratios exceed 10^6 at a V_{DS} of 2 V with off-state currents less than 1 pA. Using the slope of the I_{DS}-V_{GS}

curve in the linear region, the field-effect mobility is calculated using $\mu = \frac{\partial I_{DS}}{\partial V_{BG}} \cdot \frac{L}{W} \cdot \frac{1}{C_{ox} V_{DS}}$ where L, W and C_{ox} are the channel length, width and dielectric capacitance, respectively. By using a value of C_{ox} = 12 nF/cm^2 (for 285 nm thick SiO_2) and L = 500 nm, we obtain a field-effect mobility value of ~1 cm^2/(V s), that is comparable to reported values for CVD MoS_2 FETs on thermally grown SiO_2 [103–105]. Figure 5.21 (c) shows the I_{DS}-V_{DS} output curves for back-gate voltages of 20 V to 60 V with an interval of 10 V. From the exponential I_{DS}-V_{DS} at small V_{DS}, it is evident that a Schottky contact is formed, typical for SiO_2/Si back-gated MoS_2 FETs [106].

5.8 APPLICABILITY TO OTHER TMDS

To verify the repeatability of the 2-step growth method for different TMDs, the recipe was repeated to grow WS_2. A 1min growth at 850 °C using the precursors $W(CO)_6$ (99.99% pure, Sigma Aldrich CAS no: 14040-11-0) and diethyl sulfide, $(C_2H_5)_2S$ (Sigma-Aldrich, CAS number 352-93-2, 98%) yields uniform continuous WS_2 film. Upon sulfurization at 850 ºC for 30 min, the crystalline quality of the grown WS_2 is seen to greatly improved as seen from the enhanced Raman peaks in Figure 5.22 (a). Additionally, following sulfurization the PL peak of the as-grown film [shown by black line in Fig. 5.22 (b)] transforms into a sharp distinct peak at 1.95 eV which is characteristic of highly crystalline monolayer WS_2 as shown in Fig. 5.22 (b).

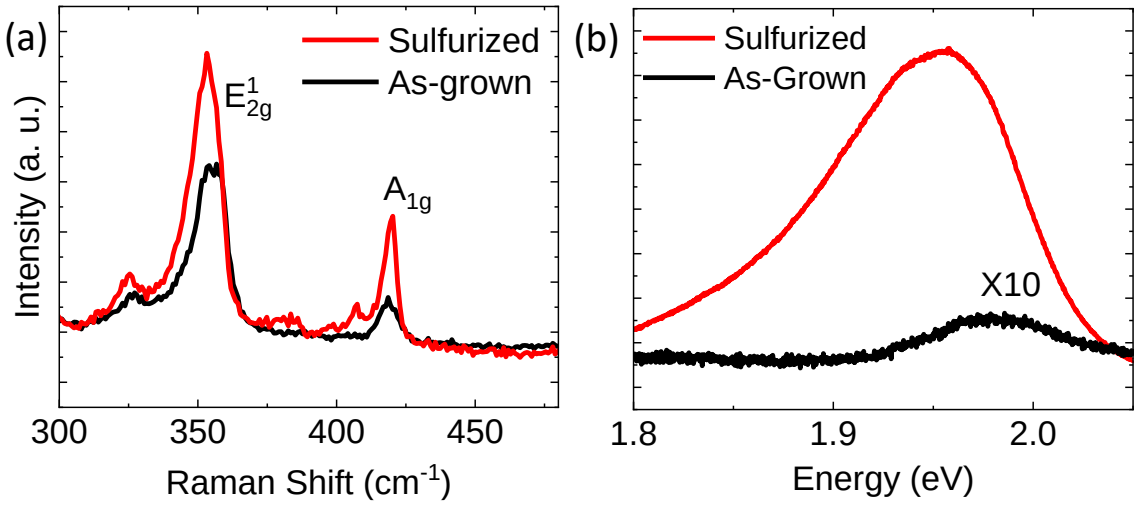

Figure 5.22: Comparison of Raman and PL spectra of the as-grown MOCVD film following sulfurization. All Raman data have been normalized with respect to Si. (a) Comparison of Raman spectra for the as grown film and sulfurized film at 850 °C. Sulfurization duration was kept 30 min for all the samples. (b) Comparison of PL spectra for WS2 film pre- and post-sulfurized at 850 °C.

5.9 CONCLUSION

In conclusion, we have grown continuous MoS_2 film *via* MOCVD and demonstrated its controlled sulfurization to form single crystal domains with uniform monolayer thickness. The effect of sulfurization temperature and duration are investigated, and an optimized condition is proposed to obtain a homogeneous distribution of large area single crystal monolayer domains. The sulfurization process heals sulfur vacancies in as grown film, thereby improving of the stoichiometry of MoS_2 as verified by XPS quantification. Interestingly, carbon contamination, one of the main challenges associated with metal organic precursors, is highly suppressed following sulfurization as evident from both Raman and XPS analysis. Monolayer nature, high crystallinity, and uniformity of MoS_2 domains are confirmed *via* Raman and PL spectroscopies. Electrical characterization of MoS_2 following sulfurization shows performance comparable to that grown by APCVD method. Our results indicate that this two-step growth method can be considered as a reliable and efficient way to synthesize large area single crystal homogeneous domains of MoS_2 with uniform monolayer coverage and can also be applied to other sulfur based TMDs.

Chapter 6: Conclusion and Outlook

In summary, we studied growth of various transition metal dichalcogenides (TMDs) using chemical vapor deposition (CVD) with a focus on understanding the importance of different parameters influencing the growth.

We investigated the role of growth temperature and metal/chalcogen flux in atmospheric pressure chemical vapor deposition (APCVD) of $MoSe_2$ and WSe_2 on Si/SiO_2 substrates. We observed that the growth temperature and transition metal flux strongly influence the domain morphology. Compact triangular or hexagonal domains ramify into branched structures as the growth temperature (metal flux) is decreased (increased). Different combinations of growth temperature and flux can produce two different branched structures - fractals and dendrites. The fractals (with a dimension of ~1.67) obey diffusion-limited aggregation (DLA) mechanism, whereas the dendrites with a higher fractal dimension of ~1.80 exhibit a preferential growth along the symmetry-governed directions. Using a phase field technique, we presented a more systematic correlation between the changes in growth parameters and corresponding morphologies of the domains observed experimentally.

Next, the effect of chalcogen environment was studied where a Se-rich condition restricted Mo-rich nuclei formation, promoting lateral growth. For a Se-deficient environment, several multilayer islands formed on two-dimensional (2D) domains, suggesting a transition from lateral to vertical growth due to insufficient Se passivation. By tuning the growth temperature and metal/chalcogen flux, we proposed an optimized window for the CVD growth to synthesize large area Mo(W)-selenide.

To understand the roles of other important parameters affecting the growth, we carried out APCVD growth of MoS_2 monolayer film under various combinations of carrier gases: N_2, Ar and H_2. We observed that, compared to other carrier gases, more uniform 2D growth of MoS_2 was achieved under H_2 due to a reducing environment. To understand the effect of H_2 incorporation we employed a phase field model to support the experimental findings.

In another approach, to achieve large area growth of TMDs of uniform monolayer thickness, we demonstrated metal-organic CVD (MOCVD) growth under low pressure followed by a high-temperature sulfurization process under atmospheric pressure (AP). We observed that following sulfurization, structural disorders and chalcogen vacancies inherent to as-grown MOCVD film were substantially healed, and carbon/oxygen contaminations were heavily suppressed. In addition, the continuous MOCVD-grown MoS_2 film transformed into compact triangular crystals of uniform monolayer thickness. The effect of temperature and duration of the sulfurization process on the morphology and stoichiometry of the grown film were investigated in detail. Compared to the APCVD growth, this two-step growth process showed more homogenous distribution of the triangular monolayer MoS_2 domains across the entire substrate while demonstrating comparable electrical performance.

This work can be extended to correlate the electrical performance of CVD-grown TMDs with the morphologies, structures, and defects in grown domains, and possible route to improve by tuning the growth parameters. Moreover, this work can be applied to other TMDs to achieve more uniform homogeneous and large area monolayer TMDs.

The work presented in this dissertation can serve as the foundation to achieve large area TMDs with qualities comparable to their bulk exfoliated counterparts and may lead to several research directions in the field of CVD grown TMDs. Some of these are outlined below:

1. This work can be extended to grow heterostructures of different combination of TMDs, having novel electronic states based on moiré patterns, resonant tunneling in rotationally aligned double layer heterostructures and applications in optical devices.

2. Low-temperature transport studies will help shed light on the contact and transport mechanism, important to understand the physical properties, carrier mechanisms, dominant scattering mechanisms and the nature of contact CVD grown TMD FETs.

3. Recently, branched structure of TMD domains is being used as a catalyst for hydrogen evolution reactions (HER). Although several papers have reported application of MoS_2 in HER, other 2D TMDs, theoretically predicted to exhibit superior HER activity, are still unexplored.

4. This work demonstrated monolayer growth of MoS_2, $MoSe_2$ and WSe_2 on Si/SiO_2. Next, WSe_2 growth on a Si/SiO_2 substrate can be followed by MoS_2 or $MoSe_2$ growth on the same substrate and FETs can be made on them, such that WSe_2 FETs (p-type) and MoS_2 FETs (n-type) are located in different areas. These FETs can be used to study planar complementary metal oxide semiconductor (CMOS) devices on the same substrate.

Appendices

Appendix A: Custom Built CVD Growth System

A.1 GROWTH FURNACE

Figure A1 shows the image of the growth furnaces located at room 2.406 at MRC 2-D growth lab.

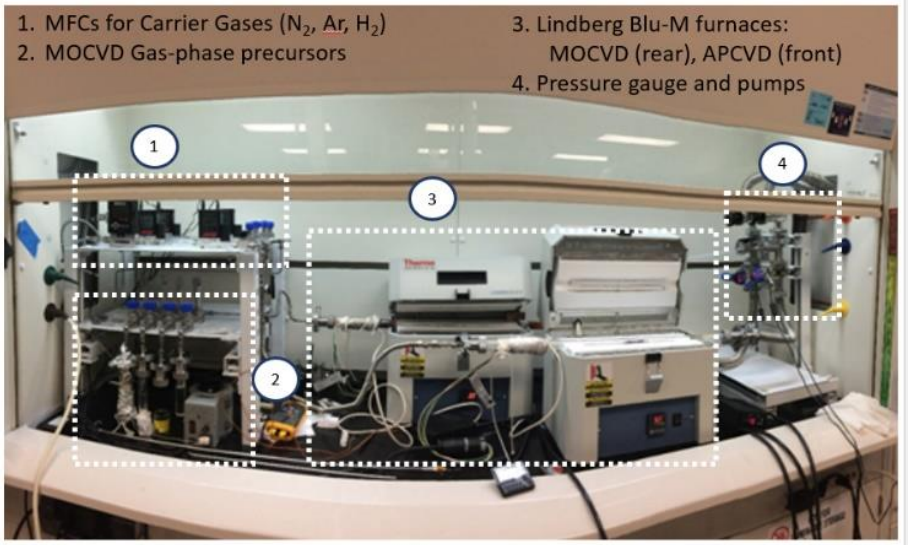

Figure A.1: CVD growth systems. (1) Mass flow controllers for carrier gases: N_2, Ar, H_2. (2) Precursors for MOCVD growth: $Mo(CO)_6$, $W(CO)_6$, $(C_2H_5)_2S$. (3) Single zone Lindberg Blu-M furnaces: MOCVD growth chamber (rear), APCVD growth chamber (front). (4) Gas outlets, pressure gauges and roughing pumps.

A.2 IMPORTANT PARTS OF THE CVD GROWTH FURNACE

Figure A.2 shows close-up images of different parts of the system.

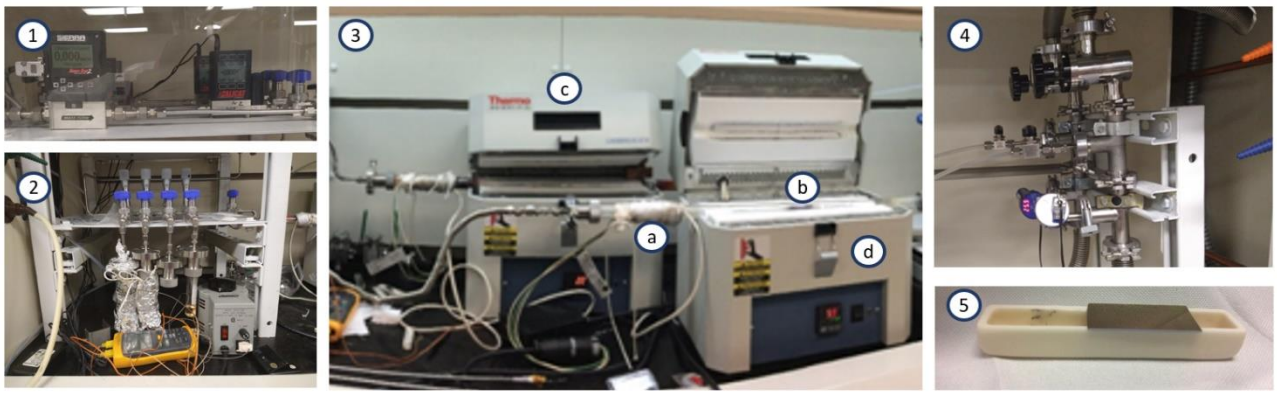

Figure A.2: Close up images of CVD growth systems. (1) Mass flow controllers for carrier gases: N_2, Ar, H_2. (2) Precursors for MOCVD growth: $Mo(CO)_6$, $W(CO)_6$, $(C_2H_5)_2S$. (3) Single zone Lindberg Blu-M furnaces: (a) secondary coil heater for sulfur (b) substrate placed face down on alumina boat inside 1" quartz tube. (c) MOCVD growth chamber (d) APCVD growth chamber (4) Gas outlets, pressure gauges and roughing pumps (5) substrate on alumina boat.

A.3 APCVD GROWTH RECIPE

A.3.1 Sample preparation

1. Obtain two boats
2. Measure out desired MoO3. Standard range is 8-15mg
3. Place it 1/3rd of the length of one boat roughly 2.5 cm from one edge
4. Cut a Si wafer with roughly the dimension 1.7cm*4.8cm
5. Place the Si piece, polished surface down) over the boat with MoO3 with 1cm open on either side of the boat
6. Make sure all gas valves are closed, valve connecting to atmosphere is also closed.
7. Insert the boat into the tube to the centre of the furnace
8. Fill the second boat with sulfur until it is full and insert into the tube to the centre of the heating coil

9. Seal off the quartz tube connecting to the nitrogen tank

A.3.2 Purge

1. Ensure all gas valves are closed
2. Turn on the Vacuum pump downstream and wait for the pressure to stabilize (~30mTorr)
3. Begin flowing nitrogen at 200sccm at automatic valve setting
4. Wait until the pressure stabilizes to 3mTorr
5. Close the vacuum valve to allow pressure to build
6. Open the vacuum valve when the pressure is> 900Torr
7. Repeat step 4-6 three times
8. Close the vacuum valve and wait for the system to pressurize
9. Adjust Nitrogen flow from 200sccm to 10sccm
10. Turn off the vacuum pump (close valve)
11. Open the exhaust valve (connection to atmosphere)

A.3.3 Growth Process

1. Ensure that the thermocouple of the heating tape is on the heating tape
2. Set the furnace to 850C by holding the blue button down and selecting LCL
3. When the furnace reaches 550C plug in the heating tape outlet
4. When the furnace reaches 850C begin counting down growth time
5. At the end of growth time, turn off furnace
6. Put on safety glasses and open the lid
7. When the furnace reaches 550C open the heating tape (Sulfur heater)
8. Wait for the furnace to cool down to <100C to retrieve your sample.
9. Clean up near the wafer cutting table and furnace
10. Leave the system under low pressure, by turning on the vacuum pump

Appendix B: Microfabrication on CVD TMDs

The main steps for device fabrication can be summarized as follows:

1. Sample preparation: Flake identification, sample cut, alignment marks
2. Defining active channel area by using Electron Beam Lithography (EBL) followed by Reactive ion etching
3. Patterning source and drain using EBL.
4. Metallization using E-beam metal evaporation (EBME) for depositing contact metal followed by metal lift-off

The steps are discussed in details as follows:

1) Sample Preparation
   a) Flake identification: Using a combination of optical microscopy, Raman and PL spectroscopy, identify regions of uniform growth
   b) Sample cut: Use diamond scribe to get a clean cut of the sample
   c) Alignment marks for e-beam lithography
      i) Spin coat photoresist:
         (1) Adhesion promoter [Hexamethyldisilazane (HMDS)]: spin-coat at 4000 rpm for 60 s followed by bake at 114.8 °C for 60 s
         (2) Resist: AZ 5214: spin coat at 4000 rpm for 60 sec followed by bake at 100 °C for 60 s

---

Portions of this Chapter, including figures are part of the following manuscript: (1) Sayema Chowdhury, et al. "*Role of hydrogen in suppressing secondary nucleation in chemical vapor deposited MoS_2*" (in preparation); The dissertator, S. Chowdhury, conceived and designed the experiments, conducted growths, characterization, performed microscopy, contributed to data analysis and largely wrote the manuscripts with contributions from all the authors.

ii) Photolithography:

(1) Tool: Mask aligner (SussMicrotec -MA6/BA6)

(2) Exposure Recipe: Exposure time 7.5 sec,

gap 40 µm,

exposure type= vacuum (6 s, 30 s, 10 s)

(3) Develop: Use developer MEGAPOSIT™ MF-26A for 30 sec followed by DI water rinse + N_2 blow-dry

iii) Metallization

(1) Cr/Au (5 nm/ 30 nm) deposition *via* e-beam evaporation

(2) Metal lift-off: Use acetone (65 °C for 30 min) followed by rinse in IPA+ N_2 blow-dry

2) E-beam lithography (EBL): For defining the device active region [Figure B.1].

a) Apply Photoresist [PMMA A4 (950 PMMA 4% in anisole from www.microchem.com)]: Spin 4000 rpm for 60 sec, followed by bake at 180 °C for 60 s

b) Patterning: E-Beam parameters: 20 kV accelerating voltage and dose of 360 µC/cm^2

c) Develop:

Developer: 1:3 solution of methyl isobutyl ketone (MIBK): IPA

Recipe: Develop for 25 sec, followed by rinse in IPA for 30 sec + N_2 blow-dry

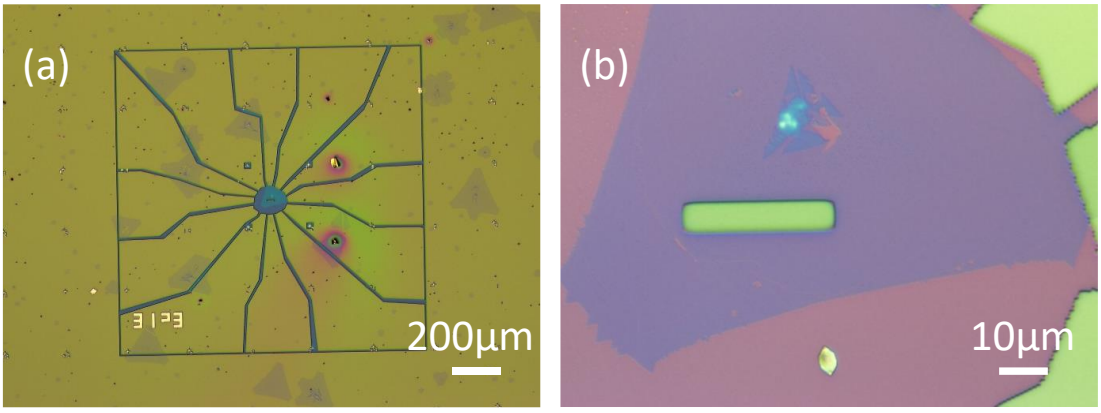

Figure B.1: (a) Using EBL to pattern active device area. (b) Zoomed image of the active MoS_2 area post development.

d) Use Reactive ion etching (RIE) to etch out unwanted material leaving the active device area [Figure B.2]

i) Tool: Plasma-Therm 790 RIE

ii) Etch Mask: PMMA

iii) Etch Recipe (MoS_2): Cl_2 (20 sccm) + O_2 (4 sccm) plasma,

Chamber pressure 200 mTorr; RF power 75 W

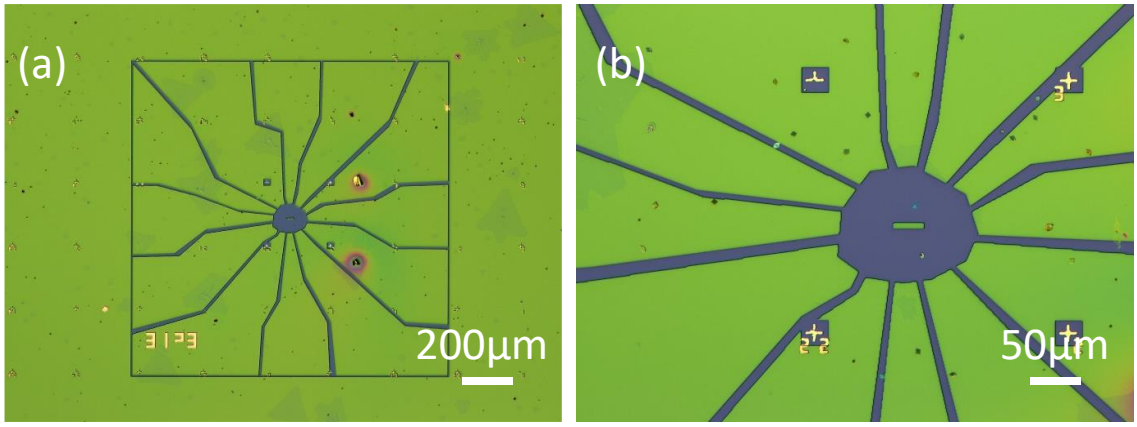

Figure B.2: (a) Using RIE to etch excess material to define active device area. (b) Zoomed image post RIE etch.

iv) Clean the e-beam resist using acetone dip followed by IPA rinse.

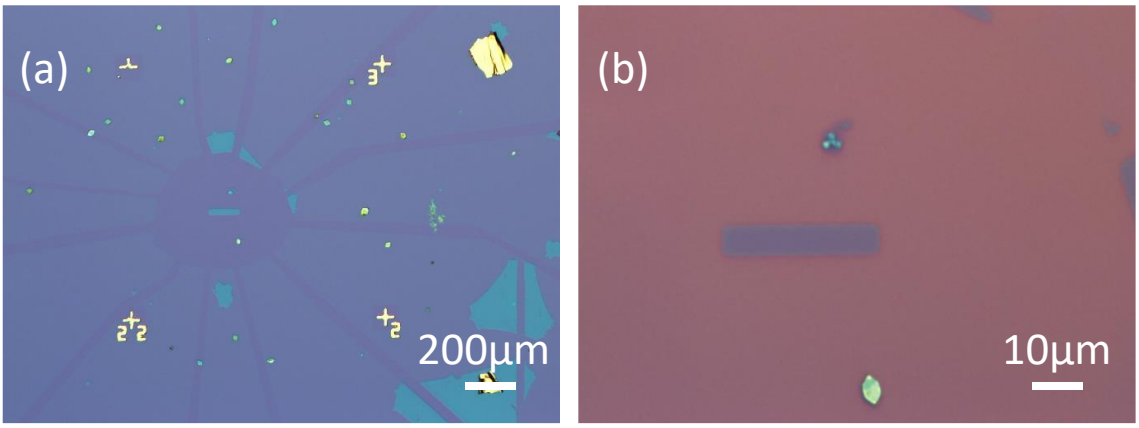

Figure B.3: (a) Active device area post etch and cleaning. (b) Zoomed image of active device area.

3) E-beam lithography (EBL): For patterning source and drain region

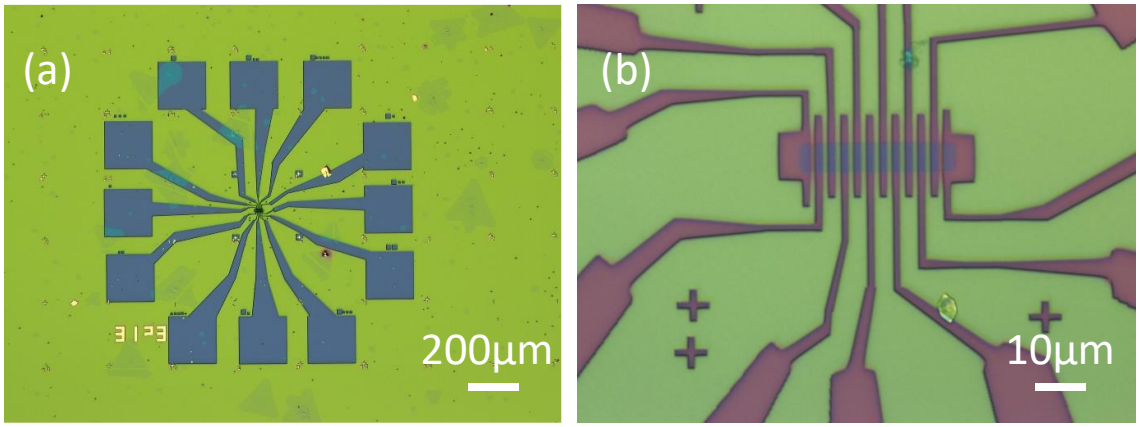

Figure B.4: (a) Patterning source drain region using EBL. (b) Zoomed image of the source drain pads.

4) Metallization *via* e-beam evaporation

a) Deposition rate: < 0.5 Å/sec for Ni to ensure film uniformity; ~1 Å/sec for Au

b) Base pressure ~ 10^{-6} Torr

c) Chamber T < 60 °C to avoid resist reflow

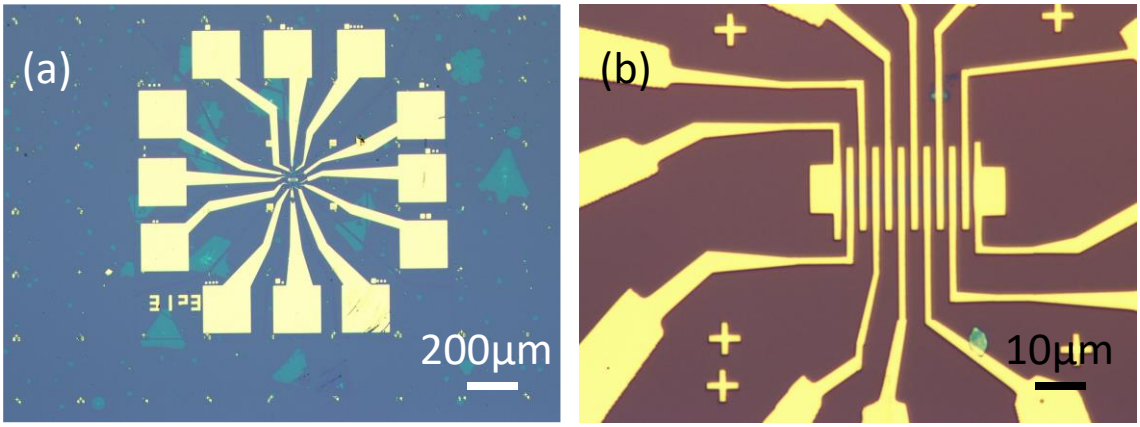

Figure B.5: (a) Metallization via e-beam evaporation (b) Zoomed image of the source drain pads.

Appendix C: Growth of MoS_2 on Various Substrates

Below we present some of the APCVD growth of MoS_2 grown on different substrates [107] using the same recipe [850 °C for 5 min]. We observe that there is a substrate dependence on the morphology of the grown domains. This is discussed in greater detail in chapter 4.

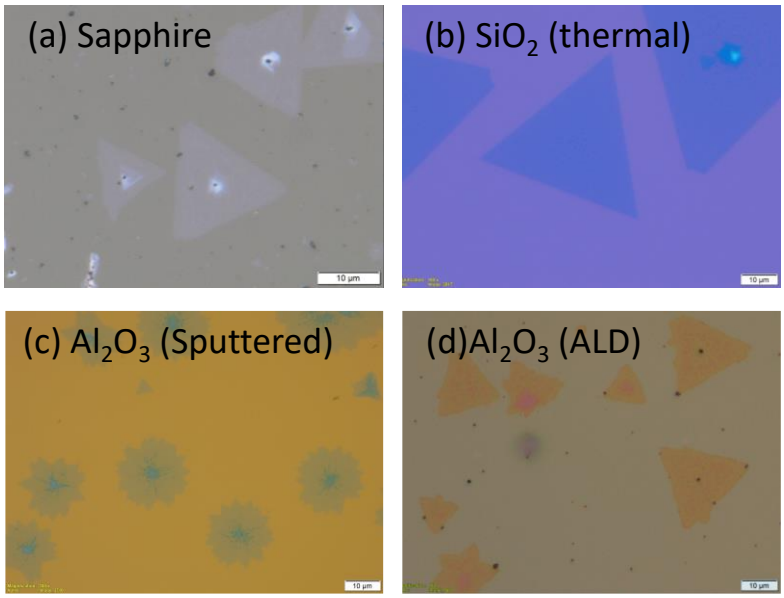

Figure C.1: MoS_2 grown using CVD on (a) Sapphire (b) Si/SiO_2 (thermally grown) (c) Al_2O_3 (Sputtered) and (d) Al_2O_3 (ALD-grown).

Appendix D: Phase Field Modeling of Morphology Evolution of CVD Grown $MoSe_2$

APCVD growth of 2D-TMDs is highly sensitive to any changes in growth parameters. As observed in chapter 3, at an optimized growth temperature and transition metal flux, 2D compact domains grow primarily triangular/hexagonal in shape that ramify into dendritic structures at higher transition metal flux. Domain morphologies evolve with locations away from the center due to changes in the local flux. For a better understanding, phase field simulations are carried out to demonstrate experimentally observed morphology evolution as a function of transition metal flux variation.

Phase-field modeling (PFM) is a well-established technique to study the 2D/3D growth in solids from corresponding liquid or vapor phases [108] and has been used successfully to model growth of different 2D materials, for example, graphene [109–112], TMDs [113–115] and *h*-BN [116] etc.

2D solid growth from its vapor phase, in PFM, is characterized by a phase variable ψ, that takes up a value of +1 for the solid phase and -1 for the vapor phase and is approximated to be a continuous variation within a narrow but finite width at the edges. The growth in 2D is described as [112,117],

$$\tau_\psi \frac{\partial \psi}{\partial t} = -\frac{\partial}{\partial x}\left(\kappa\kappa' \frac{\partial \psi}{\partial y}\right) + \frac{\partial}{\partial y}\left(\kappa\kappa' \frac{\partial \psi}{\partial x}\right) + \nabla.(\kappa^2 \nabla\psi) + \sin(\pi\psi) + \lambda(\mathrm{c} - \mathrm{c_{eq}})\{1 + \cos(\pi\psi)\}, \text{ – Equation (1)}$$

Portions of this Chapter, including figures are part of the following two manuscripts: (1) Sayema Chowdhury, et al. "*Role of hydrogen in suppressing secondary nucleation in chemical vapor deposited MoS_2*" (in preparation); and (2) Anupam Roy[#], Tanmoy Pramanik[#], Sayema Chowdhury[#] and Sanjay K Banerjee "*Phase-Field Modeling for the Morphological Evolution of Chemical Vapor Deposited Two-Dimensional $MoSe_2$*" (in preparation) ([#]equal contribution). The dissertator, S. Chowdhury, conceived and designed the experiments, conducted growths, carried out Raman and Photoluminescence measurements, performed atomic force microscopy and scanning electron microscopy, contributed to data analysis and largely wrote the manuscripts with contributions from all the authors.

where, τ_ψ is the attachment time, λ is the phase-field coupling parameter, c is the concentration of the adatom species on the substrate surface, c_{eq} is the concentration of the adatom species for which the grown domain remains in equilibrium with the surrounding vapor phase. κ controls the anisotropy of the edge-energy and is given as $\kappa = k^2(1 + g\cos(n\theta))$, with a constant factor of *k*, anisotropy strength *g* and number of symmetry directions *n* (e.g., *n* = 6 for hexagonal symmetry). The angle θ is given by $\theta = \tan^{-1}\left.\frac{\frac{d\psi}{dy}}{\frac{d\psi}{dx}}\right.$ and $\kappa' = \frac{d\kappa}{d\theta}$. Here, we have considered six-fold anisotropy (*n* = 6) only in the parameter κ to model domains growing with hexagonal symmetry. The variation of the adatom concentration, *c*, is given by:

$$\frac{\partial c}{\partial t} = D\nabla^2 c + \left(F - \frac{c}{\tau_s}\right)(1 - \psi) - \frac{1}{2}\frac{\partial \psi}{\partial t}, \qquad \text{– Equation (2)}$$

where, *D* is the diffusion coefficient of the adatoms on the surface, *F* is the incoming precursor flux and τ_s is the average time an adatom stays on the surface before desorption. We assume that the transition metal and chalcogenide atoms react before attaching to the domain edges. To understand the effect of flux influencing the domain morphology, we assume that the diffusion coefficient *D* is same across the surface as well as along the edges of the growing domain and we ignore any anisotropy in the same. The coupled PFM Eqns. (1) and (2) are solved using a finite-difference space discretization. For the time-integration, we use first order Euler's method for Eqn. (1) and Crank-Nicholson method for Eqn. (2) [118]. We assume a space discretization of *512* × *512* points with a cell size of $\Delta x = \Delta y = 1$. For the initialization, $\psi = -1$ everywhere, except at the center of the domain where a seed area of 2 × 2 is set to +1. The variable *c* is initialized to $F\tau_s$ in all our simulations. Assuming dimensionless forms for the phase-field equations (1) and (2), we set *D* = 10.0, λ = 200, c_{eq}= 0.03, τ_s= 18 and vary the flux *F* from 0.0025 to 0.006.

One of the observations from our experiment [Figure D.1] is the transformation of the growth morphology from compact to dendritic domains with increase in the metal flux (as well as the overall flux *F*). As increasing *F* also increases the rate of adatom

attachment to the growing domain, the edge diffusion of adatoms may no longer be effective to promote a thermodynamically favorable compact shape at the faster rate of attachment (*i.e.*, reduced attachment time, τ_ψ). A sufficiently low τ_ψ would therefore result in faster growth along the high symmetry directions and branching out of domains into dendrites [1,119].

To this end, we now vary the attachment time τ_ψ (from 5 to 400) along with the flux F. The domain morphology predicted from these simulations are shown in Fig. D.1(b) and D.1(e), which mimic the experimentally observed domains quite well, as can be seen by comparing them with Fig. D.1 (a) and D.1 (d), respectively. The values of (F, τ_ψ) pairs obtained from these two growth conditions are (0.0025, 300) and (0.005, 20), respectively for the compact and dendritic morphologies. The adatom concentration profiles as obtained from the simulations are shown in Fig. D.1 (c) and D.1 (f), respectively.

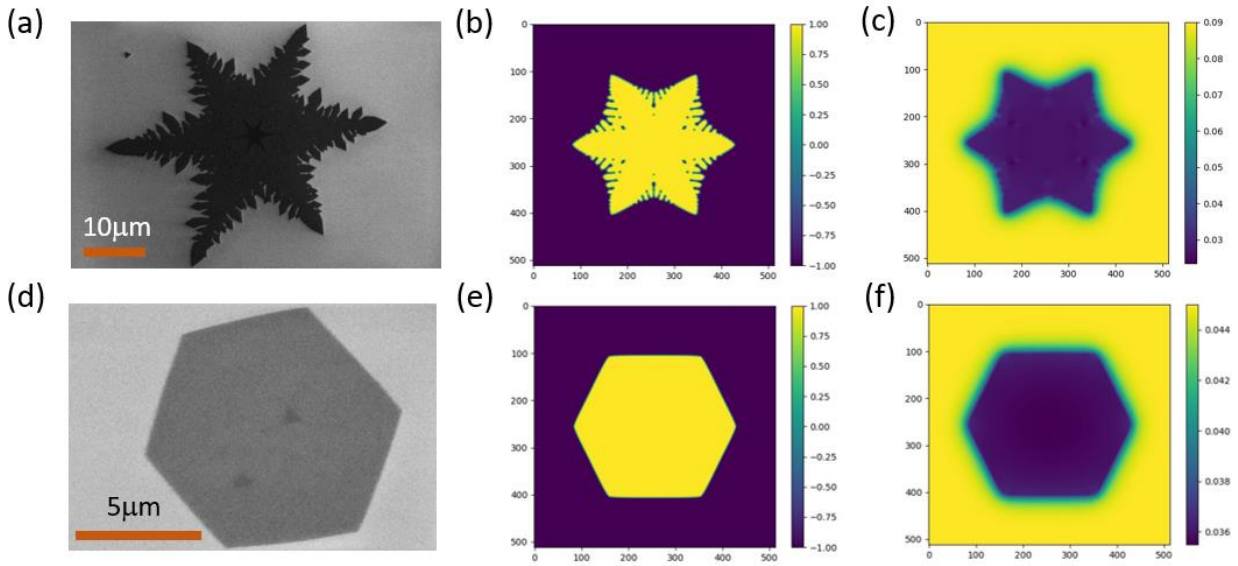

Figure D.1: APCVD growth of $MoSe_2$: (a, d) at higher and lower transition metal flux, respectively. Phase filed simulation reproducing the experimentally observed domain patterns at corresponding transition metal flux conditions are shown in (b) and (e). Corresponding concentration profiles are shown in (c) and (f), respectively.

References

[1] S. Chowdhury, A. Roy, I. Bodemann, and S. K. Banerjee, *Two-Dimensional to Three-Dimensional Growth of Transition Metal Diselenides by Chemical Vapor Deposition: Interplay between Fractal, Dendritic, and Compact Morphologies*, ACS Appl. Mater. Interfaces **12**, 15885 (2020).

[2] S. Chowdhury, A. Roy, C. Liu, M. H. Alam, R. Ghosh, H. Chou, D. Akinwande, and S. K. Banerjee, *Two-Step Growth of Uniform Monolayer MoS $_2$ Nanosheets by Metal–Organic Chemical Vapor Deposition*, ACS Omega **6**, 10343 (2021).

[3] K. F. Mak, C. Lee, J. Hone, J. Shan, and T. F. Heinz, *Atomically Thin MoS 2 : A New Direct-Gap Semiconductor*, Phys. Rev. Lett. **105**, 136805 (2010).

[4] W. Zhao, Z. Ghorannevis, L. Chu, M. Toh, C. Kloc, P.-H. Tan, and G. Eda, *Evolution of Electronic Structure in Atomically Thin Sheets of WS $_2$ and WSe $_2$*, ACS Nano **7**, 791 (2013).

[5] A. Daus, S. Vaziri, V. Chen, Ç. Köroğlu, R. W. Grady, C. S. Bailey, H. R. Lee, K. Schauble, K. Brenner, and E. Pop, *High-Performance Flexible Nanoscale Transistors Based on Transition Metal Dichalcogenides*, Nat. Electron. **4**, 495 (2021).

[6] M. Bernardi, M. Palummo, and J. C. Grossman, *Extraordinary Sunlight Absorption and One Nanometer Thick Photovoltaics Using Two-Dimensional Monolayer Materials*, Nano Lett. **13**, 3664 (2013).

[7] V. Podzorov, M. E. Gershenson, Ch. Kloc, R. Zeis, and E. Bucher, *High-Mobility Field-Effect Transistors Based on Transition Metal Dichalcogenides*, Appl. Phys. Lett. **84**, 3301 (2004).

[8] Z. Wang, D.-K. Ki, J. Y. Khoo, D. Mauro, H. Berger, L. S. Levitov, and A. F. Morpurgo, *Origin and Magnitude of 'Designer' Spin-Orbit Interaction in Graphene on Semiconducting Transition Metal Dichalcogenides*, Phys. Rev. X **6**, 041020 (2016).

[9] M. Bonilla, S. Kolekar, Y. Ma, H. C. Diaz, V. Kalappattil, R. Das, T. Eggers, H. R. Gutierrez, M.-H. Phan, and M. Batzill, *Strong Room-Temperature Ferromagnetism in VSe2 Monolayers on van Der Waals Substrates*, Nat. Nanotechnol. **13**, 289 (2018).

[10] G. Fiori, F. Bonaccorso, G. Iannaccone, T. Palacios, D. Neumaier, A. Seabaugh, S. K. Banerjee, and L. Colombo, *Electronics Based on Two-Dimensional Materials*, Nat. Nanotechnol. **9**, 768 (2014).

[11] D. Krasnozhon, D. Lembke, C. Nyffeler, Y. Leblebici, and A. Kis, *MoS $_2$ Transistors Operating at Gigahertz Frequencies*, Nano Lett. **14**, 5905 (2014).

[12] A. Rai, H. C. P. Movva, A. Roy, D. Taneja, S. Chowdhury, and S. K. Banerjee, *Progress in Contact, Doping and Mobility Engineering of MoS2: An Atomically Thin 2D Semiconductor*, Crystals **8**, 8 (2018).

[13] K. F. Mak and J. Shan, *Photonics and Optoelectronics of 2D Semiconductor Transition Metal Dichalcogenides*, Nat. Photonics **10**, 216 (2016).

[14] R. Chaudhary, K. Patel, R. K. Sinha, S. Kumar, and P. K. Tyagi, *Potential Application of Mono/Bi-Layer Molybdenum Disulfide (MoS $_2$) Sheet as an Efficient*

Transparent Conducting Electrode in Silicon Heterojunction Solar Cells, J. Appl. Phys. **120**, 013104 (2016).
[15] Y. Li, C.-Y. Xu, J.-Y. Wang, and L. Zhen, *Photodiode-Like Behavior and Excellent Photoresponse of Vertical Si/Monolayer MoS2 Heterostructures*, Sci. Rep. **4**, 7186 (2015).
[16] M.-L. Tsai, S.-H. Su, J.-K. Chang, D.-S. Tsai, C.-H. Chen, C.-I. Wu, L.-J. Li, L.-J. Chen, and J.-H. He, *Monolayer MoS $_2$ Heterojunction Solar Cells*, ACS Nano **8**, 8317 (2014).
[17] X. Xu, W. Yao, D. Xiao, and T. F. Heinz, *Spin and Pseudospins in Layered Transition Metal Dichalcogenides*, Nat. Phys. **10**, 343 (2014).
[18] D. Xiao, G.-B. Liu, W. Feng, X. Xu, and W. Yao, *Coupled Spin and Valley Physics in Monolayers of MoS 2 and Other Group-VI Dichalcogenides*, Phys. Rev. Lett. **108**, 196802 (2012).
[19] M. Chhowalla, H. S. Shin, G. Eda, L.-J. Li, K. P. Loh, and H. Zhang, *The Chemistry of Two-Dimensional Layered Transition Metal Dichalcogenide Nanosheets*, Nat. Chem. **5**, 263 (2013).
[20] H.-J. Chuang, X. Tan, N. J. Ghimire, M. M. Perera, B. Chamlagain, M. M.-C. Cheng, J. Yan, D. Mandrus, D. Tománek, and Z. Zhou, *High Mobility WSe $_2$ p - and n - Type Field-Effect Transistors Contacted by Highly Doped Graphene for Low-Resistance Contacts*, Nano Lett. **14**, 3594 (2014).
[21] H. Li, J. Wu, Z. Yin, and H. Zhang, *Preparation and Applications of Mechanically Exfoliated Single-Layer and Multilayer MoS $_2$ and WSe $_2$ Nanosheets*, Acc. Chem. Res. **47**, 1067 (2014).
[22] H. J. Liu, L. Jiao, L. Xie, F. Yang, J. L. Chen, W. K. Ho, C. L. Gao, J. F. Jia, X. D. Cui, and M. H. Xie, *Molecular-Beam Epitaxy of Monolayer and Bilayer WSe $_2$: A Scanning Tunneling Microscopy/Spectroscopy Study and Deduction of Exciton Binding Energy*, 2D Mater. **2**, 034004 (2015).
[23] R. Yue et al., *Nucleation and Growth of WSe $_2$: Enabling Large Grain Transition Metal Dichalcogenides*, 2D Mater. **4**, 045019 (2017).
[24] A. Roy, H. C. P. Movva, B. Satpati, K. Kim, R. Dey, A. Rai, T. Pramanik, S. Guchhait, E. Tutuc, and S. K. Banerjee, *Structural and Electrical Properties of MoTe $_2$ and MoSe $_2$ Grown by Molecular Beam Epitaxy*, ACS Appl. Mater. Interfaces **8**, 7396 (2016).
[25] J. Xia, X. Huang, L.-Z. Liu, M. Wang, L. Wang, B. Huang, D.-D. Zhu, J.-J. Li, C.-Z. Gu, and X.-M. Meng, *CVD Synthesis of Large-Area, Highly Crystalline MoSe $_2$ Atomic Layers on Diverse Substrates and Application to Photodetectors*, Nanoscale **6**, 8949 (2014).
[26] B. Liu, M. Fathi, L. Chen, A. Abbas, Y. Ma, and C. Zhou, *Chemical Vapor Deposition Growth of Monolayer WSe $_2$ with Tunable Device Characteristics and Growth Mechanism Study*, ACS Nano **9**, 6119 (2015).
[27] X. Lu et al., *Large-Area Synthesis of Monolayer and Few-Layer MoSe $_2$ Films on SiO $_2$ Substrates*, Nano Lett. **14**, 2419 (2014).

[28] Y. Li, K. Zhang, F. Wang, Y. Feng, Y. Li, Y. Han, D. Tang, and B. Zhang, *Scalable Synthesis of Highly Crystalline MoSe $_2$ and Its Ambipolar Behavior*, ACS Appl. Mater. Interfaces **9**, 36009 (2017).
[29] X. Wang et al., *Chemical Vapor Deposition Growth of Crystalline Monolayer MoSe $_2$*, ACS Nano **8**, 5125 (2014).
[30] X. Ling, Y.-H. Lee, Y. Lin, W. Fang, L. Yu, M. S. Dresselhaus, and J. Kong, *Role of the Seeding Promoter in MoS $_2$ Growth by Chemical Vapor Deposition*, Nano Lett. **14**, 464 (2014).
[31] J.-K. Huang, J. Pu, C.-L. Hsu, M.-H. Chiu, Z.-Y. Juang, Y.-H. Chang, W.-H. Chang, Y. Iwasa, T. Takenobu, and L.-J. Li, *Large-Area Synthesis of Highly Crystalline WSe $_2$ Monolayers and Device Applications*, ACS Nano **8**, 923 (2014).
[32] K. Chen, A. Roy, A. Rai, H. C. P. Movva, X. Meng, F. He, S. K. Banerjee, and Y. Wang, *Accelerated Carrier Recombination by Grain Boundary/Edge Defects in MBE Grown Transition Metal Dichalcogenides*, APL Mater. **6**, 056103 (2018).
[33] Y.-H. Lee et al., *Synthesis of Large-Area MoS2 Atomic Layers with Chemical Vapor Deposition*, Adv. Mater. **24**, 2320 (2012).
[34] C. Cong, J. Shang, X. Wu, B. Cao, N. Peimyoo, C. Qiu, L. Sun, and T. Yu, *Synthesis and Optical Properties of Large-Area Single-Crystalline 2D Semiconductor WS2 Monolayer from Chemical Vapor Deposition*, Adv. Opt. Mater. **2**, 131 (2014).
[35] Y.-C. Lin, H.-P. Komsa, C.-H. Yeh, T. Björkman, Z.-Y. Liang, C.-H. Ho, Y.-S. Huang, P.-W. Chiu, A. V. Krasheninnikov, and K. Suenaga, *Single-Layer ReS $_2$: Two-Dimensional Semiconductor with Tunable In-Plane Anisotropy*, ACS Nano **9**, 11249 (2015).
[36] M. Hafeez, L. Gan, H. Li, Y. Ma, and T. Zhai, *Chemical Vapor Deposition Synthesis of Ultrathin Hexagonal ReSe2 Flakes for Anisotropic Raman Property and Optoelectronic Application*, Adv. Mater. **28**, 8296 (2016).
[37] X. Zhang, H. Nan, S. Xiao, X. Wan, X. Gu, A. Du, Z. Ni, and K. (Ken) Ostrikov, *Transition Metal Dichalcogenides Bilayer Single Crystals by Reverse-Flow Chemical Vapor Epitaxy*, Nat. Commun. **10**, 598 (2019).
[38] B. Kalanyan, W. A. Kimes, R. Beams, S. J. Stranick, E. Garratt, I. Kalish, A. V. Davydov, R. K. Kanjolia, and J. E. Maslar, *Rapid Wafer-Scale Growth of Polycrystalline 2H-MoS $_2$ by Pulsed Metal–Organic Chemical Vapor Deposition*, Chem. Mater. **29**, 6279 (2017).
[39] T. K. Nguyen, A. D. Nguyen, C. T. Le, F. Ullah, K. Koo, E. Kim, D.-W. Kim, J. I. Jang, and Y. S. Kim, *Large-Scale Conformal Growth of Atomic-Thick MoS2 for Highly Efficient Photocurrent Generation*, 25 (n.d.).
[40] K. Kang, S. Xie, L. Huang, Y. Han, P. Y. Huang, K. F. Mak, C.-J. Kim, D. Muller, and J. Park, *High-Mobility Three-Atom-Thick Semiconducting Films with Wafer-Scale Homogeneity*, Nature **520**, 656 (2015).
[41] Z. Islam, K. Zhang, J. Robinson, and A. Haque, *Quality Enhancement of Low Temperature Metal Organic Chemical Vapor Deposited MoS $_2$: An Experimental and Computational Investigation*, Nanotechnology **30**, 395402 (2019).

[42] C. M. Schäfer, J. C. Roque, E. D. Corro, J. Bousquet, C. Hébert, G. Sauthier, J. Santiso, and J. A. Garrido, *NaCl-Assisted, Low Pressure MOCVD Growth of Mono- to Few Layer MoS2*, 1 (n.d.).
[43] *Schäfer, C., Caicedo, J. M., Del Corro, E., Bousquet, J., Hébert, C., Sauthier, G., ... & Garrido, J. A. (2019). Assessment of Carbon Contamination in MoS2 Grown by MOCVD Using Mo (CO) 6 and (CH3-CH2) 2S Precursors.*, (n.d.).
[44] B. McMurtray, *Growth of Molybdenum Disulfide Atomic Layers*, 2 (n.d.).
[45] T. Kim, J. Mun, H. Park, D. Joung, M. Diware, C. Won, J. Park, S.-H. Jeong, and S.-W. Kang, *Wafer-Scale Production of Highly Uniform Two-Dimensional MoS_2 by Metal-Organic Chemical Vapor Deposition*, Nanotechnology **28**, 18LT01 (2017).
[46] J. Mun et al., *High-Mobility MoS_2 Directly Grown on Polymer Substrate with Kinetics-Controlled Metal–Organic Chemical Vapor Deposition*, ACS Appl. Electron. Mater. **1**, 608 (2019).
[47] H. Kim, D. Ovchinnikov, D. Deiana, D. Unuchek, and A. Kis, *Suppressing Nucleation in Metal–Organic Chemical Vapor Deposition of MoS_2 Monolayers by Alkali Metal Halides*, Nano Lett. **17**, 5056 (2017).
[48] H. Kim et al., *Role of Alkali Metal Promoter in Enhancing Lateral Growth of Monolayer Transition Metal Dichalcogenides*, Nanotechnology **28**, 36LT01 (2017).
[49] H. Li, Q. Zhang, C. C. R. Yap, B. K. Tay, T. H. T. Edwin, A. Olivier, and D. Baillargeat, *From Bulk to Monolayer MoS2: Evolution of Raman Scattering*, Adv. Funct. Mater. **22**, 1385 (2012).
[50] K. M. McCreary, A. T. Hanbicki, S. Singh, R. K. Kawakami, G. G. Jernigan, M. Ishigami, A. Ng, T. H. Brintlinger, R. M. Stroud, and B. T. Jonker, *The Effect of Preparation Conditions on Raman and Photoluminescence of Monolayer WS2*, Sci. Rep. **6**, 35154 (2016).
[51] H. Li, Q. Zhang, C. C. R. Yap, B. K. Tay, T. H. T. Edwin, A. Olivier, and D. Baillargeat, *From Bulk to Monolayer MoS2: Evolution of Raman Scattering*, Adv. Funct. Mater. **22**, 1385 (2012).
[52] A. Roy, S. Guchhait, S. Sonde, R. Dey, T. Pramanik, A. Rai, H. C. P. Movva, L. Colombo, and S. K. Banerjee, *Two-Dimensional Weak Anti-Localization in Bi_2Te_3 Thin Film Grown on Si(111)-(7 × 7) Surface by Molecular Beam Epitaxy*, Appl. Phys. Lett. **102**, 163118 (2013).
[53] S. Wang, X. Wang, and J. H. Warner, *All Chemical Vapor Deposition Growth of MoS_2:H-BN Vertical van Der Waals Heterostructures*, ACS Nano **9**, 5246 (2015).
[54] S. Tongay, J. Zhou, C. Ataca, K. Lo, T. S. Matthews, J. Li, J. C. Grossman, and J. Wu, *Thermally Driven Crossover from Indirect toward Direct Bandgap in 2D Semiconductors: $MoSe_2$ versus MoS_2*, Nano Lett. **12**, 5576 (2012).
[55] K. He, N. Kumar, L. Zhao, Z. Wang, K. F. Mak, H. Zhao, and J. Shan, *Tightly Bound Excitons in Monolayer WSe 2*, Phys. Rev. Lett. **113**, 026803 (2014).
[56] Y.-C. Lin et al., *Atomically Thin Heterostructures Based on Single-Layer Tungsten Diselenide and Graphene*, Nano Lett. **14**, 6936 (2014).
[57] X. Yin, Z. Ye, D. A. Chenet, Y. Ye, J. C. Hone, and X. Zhang, *Edge Nonlinear Optics on a MoS2 Atomic Monolayer*, **344**, 4 (2014).

[58] H. Brune, C. Romainczyk, H. Röder, and K. Kern, *Mechanism of the Transition from Fractal to Dendritic Growth of Surface Aggregates*, Nature **369**, 469 (1994).
[59] F. Meng, S. A. Morin, A. Forticaux, and S. Jin, *Screw Dislocation Driven Growth of Nanomaterials*, Acc. Chem. Res. **46**, 1616 (2013).
[60] H. Brune, K. Bromann, K. Kern, J. Jacobsen, P. Stoltze, K. Jacobsen, and J. Nørskov, *Fractal and Dendritic Growth of Surface Aggregates*, MRS Proc. **407**, 379 (1995).
[61] T. Park, C. Bae, H. Lee, M. Leem, H. Kim, W. Ahn, J. Kim, E. Lee, H. Shin, and H. Kim, *Non-Equilibrium Fractal Growth of MoS_2 for Electrocatalytic Hydrogen Evolution*, CrystEngComm **21**, 478 (2019).
[62] W. Xu, S. Li, S. Zhou, J. K. Lee, S. Wang, S. G. Sarwat, X. Wang, H. Bhaskaran, M. Pasta, and J. H. Warner, *Large Dendritic Monolayer MoS_2 Grown by Atmospheric Pressure Chemical Vapor Deposition for Electrocatalysis*, ACS Appl. Mater. Interfaces **10**, 4630 (2018).
[63] S. Wang and H. Xin, *Fractal and Dendritic Growth of Metallic Ag Aggregated from Different Kinds of γ-Irradiated Solutions*, J. Phys. Chem. B **104**, 5681 (2000).
[64] T. Michely and J. Krug, *Islands, Mounds and Atoms* (Springer-Verlag, Berlin Heidelberg, 2004).
[65] Z. L. Wang, Y. Liu, and Z. Zhang, editors , *Chemical Vapor Deposition*, in *Handbook of Nanophase and Nanostructured Materials* (Springer US, Boston, MA, 2002), pp. 102–144.
[66] S. Karthika, T. K. Radhakrishnan, and P. Kalaichelvi, *A Review of Classical and Nonclassical Nucleation Theories*, Cryst. Growth Des. **16**, 6663 (2016).
[67] H. Ye, J. Zhou, D. Er, C. C. Price, Z. Yu, Y. Liu, J. Lowengrub, J. Lou, Z. Liu, and V. B. Shenoy, *Toward a Mechanistic Understanding of Vertical Growth of van Der Waals Stacked 2D Materials: A Multiscale Model and Experiments*, ACS Nano **11**, 12780 (2017).
[68] Y. Nie, C. Liang, K. Zhang, R. Zhao, S. M. Eichfeld, P.-R. Cha, L. Colombo, J. A. Robinson, R. M. Wallace, and K. Cho, *First Principles Kinetic Monte Carlo Study on the Growth Patterns of WSe_2 Monolayer*, 2D Mater. **3**, 025029 (2016).
[69] R. B. Quincy, Marwan. Houalla, Andrew. Proctor, and D. M. Hercules, *Distribution of Molybdenum Oxidation States in Reduced Molybdenum/Titania Catalysts: Correlation with Benzene Hydrogenation Activity*, J. Phys. Chem. **94**, 1520 (1990).
[70] Y. Zhang et al., *Controlled Growth of High-Quality Monolayer WS_2 Layers on Sapphire and Imaging Its Grain Boundary*, ACS Nano **7**, 8963 (2013).
[71] Y. Yoo, Z. P. Degregorio, and J. E. Johns, *Seed Crystal Homogeneity Controls Lateral and Vertical Heteroepitaxy of Monolayer MoS_2 and WS_2*, J. Am. Chem. Soc. **137**, 14281 (2015).
[72] Y. Sheng, H. Tan, X. Wang, and J. H. Warner, *Hydrogen Addition for Centimeter-Sized Monolayer Tungsten Disulfide Continuous Films by Ambient Pressure Chemical Vapor Deposition*, Chem Mater 8 (2017).
[73] W. He, D. Geng, and Z. Xu, *Pattern Evolution Characterizes the Mechanism and Efficiency of CVD Graphene Growth*, Carbon **141**, 316 (2019).

[74] A. Roy et al., *Intra-Domain Periodic Defects in Monolayer MoS $_2$*, Appl. Phys. Lett. **110**, 201905 (2017).
[75] X.-J. Lv, G.-W. She, S.-X. Zhou, and Y.-M. Li, *Highly Efficient Electrocatalytic Hydrogen Production by Nickel Promoted Molybdenum Sulfide Microspheres Catalysts*, RSC Adv. **3**, 21231 (2013).
[76] B. Li, L. Jiang, X. Li, P. Ran, P. Zuo, A. Wang, L. Qu, Y. Zhao, Z. Cheng, and Y. Lu, *Preparation of Monolayer MoS2 Quantum Dots Using Temporally Shaped Femtosecond Laser Ablation of Bulk MoS2 Targets in Water*, Sci. Rep. **7**, 11182 (2017).
[77] X. Li, X. Li, X. Zang, M. Zhu, Y. He, K. Wang, D. Xie, and H. Zhu, *Role of Hydrogen in the Chemical Vapor Deposition Growth of MoS $_2$ Atomic Layers*, Nanoscale **7**, 8398 (2015).
[78] P. Li, Z. Li, and J. Yang, *Dominant Kinetic Pathways of Graphene Growth in Chemical Vapor Deposition: The Role of Hydrogen*, J. Phys. Chem. C **121**, 25949 (2017).
[79] D. Dumcenco et al., *Large-Area Epitaxial Monolayer MoS $_2$*, ACS Nano **9**, 4611 (2015).
[80] S. Wu, C. Huang, G. Aivazian, J. S. Ross, D. H. Cobden, and X. Xu, *Vapor–Solid Growth of High Optical Quality MoS $_2$ Monolayers with Near-Unity Valley Polarization*, ACS Nano **7**, 2768 (2013).
[81] R. Y. Tay, M. H. Griep, G. Mallick, S. H. Tsang, R. S. Singh, T. Tumlin, E. H. T. Teo, and S. P. Karna, *Growth of Large Single-Crystalline Two-Dimensional Boron Nitride Hexagons on Electropolished Copper*, Nano Lett. **14**, 839 (2014).
[82] A. Roy, T. Pramanik, S. Chowdhury, and S. K. Banerjee, *Phase-Field Modeling for the Morphological Evolution of Chemical Vapor Deposited Two-Dimensional MoSe2 (in Preparation)*, (2022).
[83] *Pattern Evolution Characterizes the Mechanism and Efficiency of CVD Graphene Growth | Elsevier Enhanced Reader*, https://doi.org/10.1016/j.carbon.2018.09.046.
[84] J. Li, Z. Hu, Y. Yi, M. Yu, X. Li, J. Zhou, J. Yin, S. Wu, and W. Guo, *Hexagonal Boron Nitride Growth on Cu-Si Alloy: Morphologies and Large Domains*, Small **15**, 1805188 (2019).
[85] J. Xu, D. J. Srolovitz, and D. Ho, *The Adatom Concentration Profile: A Paradigm for Understanding Two-Dimensional MoS $_2$ Morphological Evolution in Chemical Vapor Deposition Growth*, ACS Nano **15**, 6839 (2021).
[86] M. R. Islam, N. Kang, U. Bhanu, H. P. Paudel, M. Erementchouk, L. Tetard, M. N. Leuenberger, and S. I. Khondaker, *Tuning the Electrical Property via Defect Engineering of Single Layer MoS $_2$ by Oxygen Plasma*, Nanoscale **6**, 10033 (2014).
[87] A. Förster, S. Gemming, G. Seifert, and D. Tománek, *Chemical and Electronic Repair Mechanism of Defects in MoS $_2$ Monolayers*, ACS Nano **11**, 9989 (2017).
[88] G. Zhang, J. Wang, Z. Wu, R. Shi, W. Ouyang, A. Amini, B. N. Chandrashekar, N. Wang, and C. Cheng, *Shape-Dependent Defect Structures of Monolayer MoS $_2$ Crystals Grown by Chemical Vapor Deposition*, ACS Appl. Mater. Interfaces **9**, 763 (2017).

[89] A. Molina-Sánchez and L. Wirtz, *Phonons in Single-Layer and Few-Layer MoS 2 and WS 2*, Phys. Rev. B **84**, 155413 (2011).
[90] S. Mignuzzi, A. J. Pollard, N. Bonini, B. Brennan, I. S. Gilmore, M. A. Pimenta, D. Richards, and D. Roy, *Effect of Disorder on Raman Scattering of Single-Layer Mo S 2*, Phys. Rev. B **91**, 195411 (2015).
[91] R. Ghosh, J.-S. Kim, A. Roy, H. Chou, M. Vu, S. K. Banerjee, and D. Akinwande, *Large Area Chemical Vapor Deposition Growth of Monolayer MoSe $_2$ and Its Controlled Sulfurization to MoS $_2$*, J. Mater. Res. **31**, 917 (2016).
[92] G. L. Frey, R. Tenne, M. J. Matthews, M. S. Dresselhaus, and G. Dresselhaus, *Raman and Resonance Raman Investigation of MoS 2 Nanoparticles*, Phys. Rev. B **60**, 2883 (1999).
[93] F. Giannazzo, M. Bosi, F. Fabbri, E. Schilirò, G. Greco, and F. Roccaforte, *Direct Probing of Grain Boundary Resistance in Chemical Vapor Deposition-Grown Monolayer MoS2 by Conductive Atomic Force Microscopy*, Phys. Status Solidi RRL – Rapid Res. Lett. **14**, 1900393 (2020).
[94] T. H. Ly, D. J. Perello, J. Zhao, Q. Deng, H. Kim, G. H. Han, S. H. Chae, H. Y. Jeong, and Y. H. Lee, *Misorientation-Angle-Dependent Electrical Transport across Molybdenum Disulfide Grain Boundaries*, Nat. Commun. **7**, 10426 (2016).
[95] C. Wu, K. Liao, C. Wu, and S. Lin, *Luminescence Enhancement and Enlarged Dirac Point Shift of MoS2/Graphene Hetero-Structure Photodetectors With Postgrowth Annealing Treatment*, IEEE J. Sel. Top. Quantum Electron. **23**, 101 (2017).
[96] A. Kaniyoor and S. Ramaprabhu, *A Raman Spectroscopic Investigation of Graphite Oxide Derived Graphene*, AIP Adv. **2**, 032183 (2012).
[97] T. H. Choudhury, H. Simchi, R. Boichot, M. Chubarov, S. E. Mohney, and J. M. Redwing, *Chalcogen Precursor Effect on Cold-Wall Gas-Source Chemical Vapor Deposition Growth of WS $_2$*, Cryst. Growth Des. **18**, 4357 (2018).
[98] X. Zhang, Z. Y. Al Balushi, F. Zhang, T. H. Choudhury, S. M. Eichfeld, N. Alem, T. N. Jackson, J. A. Robinson, and J. M. Redwing, *Influence of Carbon in Metalorganic Chemical Vapor Deposition of Few-Layer WSe2 Thin Films*, J. Electron. Mater. **45**, 6273 (2016).
[99] T. L. Barr and S. Seal, *Nature of the Use of Adventitious Carbon as a Binding Energy Standard*, J. Vac. Sci. Technol. A **13**, 1239 (1995).
[100] P. Swift, *Adventitious Carbon—the Panacea for Energy Referencing?*, Surf. Interface Anal. **4**, 47 (1982).
[101] A. A. Murthy, Y. Li, E. Palacios, Q. Li, S. Hao, J. G. DiStefano, C. Wolverton, K. Aydin, X. Chen, and V. P. Dravid, *Optically Active 1D MoS $_2$ Nanobelts*, ACS Appl. Mater. Interfaces **10**, 6799 (2018).
[102] M. Okada, N. Okada, W.-H. Chang, T. Endo, A. Ando, T. Shimizu, T. Kubo, Y. Miyata, and T. Irisawa, *Gas-Source CVD Growth of Atomic Layered WS 2 from WF 6 and H 2 S Precursors with High Grain Size Uniformity*, Sci. Rep. **9**, 1 (2019).
[103] M. Amani, M. L. Chin, A. G. Birdwell, T. P. O'Regan, S. Najmaei, Z. Liu, P. M. Ajayan, J. Lou, and M. Dubey, *Electrical Performance of Monolayer MoS $_2$ Field-*

Effect Transistors Prepared by Chemical Vapor Deposition, Appl. Phys. Lett. **102**, 193107 (2013).
[104] J. Jeon, S. K. Jang, S. M. Jeon, G. Yoo, Y. H. Jang, J.-H. Park, and S. Lee, *Layer-Controlled CVD Growth of Large-Area Two-Dimensional MoS $_2$ Films*, Nanoscale **7**, 1688 (2015).
[105] B. Liu, L. Chen, G. Liu, A. N. Abbas, M. Fathi, and C. Zhou, *High-Performance Chemical Sensing Using Schottky-Contacted Chemical Vapor Deposition Grown Monolayer MoS $_2$ Transistors*, ACS Nano **8**, 5304 (2014).
[106] A. Sanne, R. Ghosh, A. Rai, H. C. P. Movva, A. Sharma, R. Rao, L. Mathew, and S. K. Banerjee, *Top-Gated Chemical Vapor Deposited MoS $_2$ Field-Effect Transistors on Si $_3$ N $_4$ Substrates*, Appl. Phys. Lett. **106**, 062101 (2015).
[107] M. H. Alam, S. Chowdhury, A. Roy, M. H. Braga, S. K. Banerjee, and D. Akinwande, *Direct Growth of MoS 2 on Electrolytic Substrate and Realization of High-Mobility Transistors*, Phys. Rev. Mater. **5**, 054003 (2021).
[108] A. Karma and W. J. Rappel, *Quantitative Phase-Field Modeling of Dendritic Growth in Two and Three Dimensions*, Phys. Rev. E **57**, 4323 (1998).
[109] J. Zhuang, W. Zhao, L. Qiu, J. Xin, J. Dong, and F. Ding, *Morphology Evolution of Graphene during Chemical Vapor Deposition Growth: A Phase-Field Theory Simulation*, J. Phys. Chem. C **123**, 9902 (2019).
[110] E. Meca, J. Lowengrub, H. Kim, C. Mattevi, and V. B. Shenoy, *Epitaxial Graphene Growth and Shape Dynamics on Copper: Phase-Field Modeling and Experiments*, Nano Lett. **13**, 5692 (2013).
[111] Y. Hao et al., *The Role of Surface Oxygen in the Growth of Large Single-Crystal Graphene on Copper*, Science **342**, 720 (2013).
[112] W. He, D. Geng, and Z. Xu, *Pattern Evolution Characterizes the Mechanism and Efficiency of CVD Graphene Growth*, Carbon **141**, 316 (2019).
[113] J. Wu et al., *Spiral Growth of SnSe2 Crystals by Chemical Vapor Deposition*, Adv. Mater. Interfaces **3**, 1 (2016).
[114] V. I. Artyukhov, Z. Hu, Z. Zhang, and B. I. Yakobson, *Topochemistry of Bowtie- and Star-Shaped Metal Dichalcogenide Nanoisland Formation*, Nano Lett. **16**, 3696 (2016).
[115] J. Xu, D. J. Srolovitz, and D. Ho, *The Adatom Concentration Profile: A Paradigm for Understanding Two-Dimensional MoS 2 Morphological Evolution in Chemical Vapor Deposition Growth* , ACS Nano (2021).
[116] J. Li, Z. Hu, Y. Yi, M. Yu, X. Li, J. Zhou, J. Yin, S. Wu, and W. Guo, *Hexagonal Boron Nitride Growth on Cu-Si Alloy: Morphologies and Large Domains*, Small **15**, (2019).
[117] J. Zhuang, W. Zhao, L. Qiu, J. Xin, J. Dong, and F. Ding, *Morphology Evolution of Graphene during Chemical Vapor Deposition Growth: A Phase-Field Theory Simulation*, J. Phys. Chem. C **123**, 9902 (2019).
[118] A. Karma and W. J. Rappel, *Phase-Field Method for Computationally Efficient Modeling of Solidification with Arbitrary Interface Kinetics*, Phys. Rev. E - Stat. Phys. Plasmas Fluids Relat. Interdiscip. Top. **53**, R3017 (1996).

[119] A. Rajan, K. Underwood, F. Mazzola, and P. D. C. King, *Morphology Control of Epitaxial Monolayer Transition Metal Dichalcogenides*, Phys. Rev. Mater. **4**, 14003 (2020).